SEARCHING FOR SIGNATURES OF ACCRETING MASSIVE BLACK HOLES IN DWARF GALAXIES

by

Lilikoi Jean Latimer

A dissertation submitted in partial fulfillment
of the requirements for the degree

of

Doctor of Philosophy

in

Physics

MONTANA STATE UNIVERSITY
Bozeman, Montana

May 2022

©COPYRIGHT

by

Lilikoi Jean Latimer

2022

All Rights Reserved

ACKNOWLEDGEMENTS

The research presented in this thesis was financially supported by NASA through EPSCoR grant number 80NSSC20M0231 and through *Chandra* Award Numbers GO2-13126 and GO9-20094X. I would like to thank my advisor, Dr Amy Reines, for supporting and helping me throughout my time in graduate school. I also thank my family, for being generally both supportive and wonderful.

TABLE OF CONTENTS

1. INTRODUCTION 1

2. AN X-RAY + RADIO SEARCH FOR MASSIVE BLACK HOLES IN BLUE COMPACT DWARF GALAXIES 6

Contribution of Authors and Co-Authors 6
Manuscript Information 7
Introduction 8
Sample of Blue Compact Dwarf Galaxies 9
Observations and Data Reduction 13
Chandra X-ray Observatory 13
Karl G. Jansky Very Large Array 13
Optical Images 19
Analysis and Results 19
Host Galaxies and Star Formation Rates 19
Hard X-ray Sources 22
Expected Contribution from X-ray Binaries 26
Compact Radio Sources 30
Comparison to Thermal HII Regions and SNRs 30
A Candidate Low-luminosity AGN in Haro 9 32
Detection Limits 36
Summary and Conclusions 37

3. A *CHANDRA* AND *HST* VIEW OF *WISE*-SELECTED AGN CANDIDATES IN DWARF GALAXIES 40

Contribution of Authors and Co-Authors 40
Manuscript Information 41
Introduction 42
Sample Selection 45
Observations and Data Reduction 48
Chandra X-ray Observatory 48
Optical/NIR Images 52
Analysis and Results 55
X-ray Sources 55
Expected Contribution from X-ray Binaries 57
Optical/IR Counterparts of the X-ray Sources 63
Multiwavelength AGN Scaling Relations 66
$L_{\rm X}$ vs. $L_{\rm IR}$ 66
$L_{\rm X}$ vs. $L_{\rm H\alpha}$ and $L_{\rm [O\ III]}$ 69

TABLE OF CONTENTS – CONTINUED

Summary and Conclusions 73

4. THE AGN FRACTION IN DWARF GALAXIES FROM EROSITA: FIRST RESULTS AND FUTURE PROSPECTS 82

Contribution of Authors and Co-Authors 82
Manuscript Information 83
Introduction 84
Data 85
eROSITA/eFEDS 85
Sample of Dwarf Galaxies 86
Analysis and Results 87
Dwarf Galaxies with X-ray Detections 87
Chance Alignments with Background Sources 90
Origin of the X-ray Emission in Dwarf Galaxies 92
Conclusions and Discussion 97
eROSITA Constraints on the AGN Fraction in Low-redshift Dwarf Galaxies 97
Detection limits 97
Future Prospects with eROSITA 98

5. CONCLUSION 100

REFERENCES CITED 104

LIST OF TABLES

Table Page

2.1 Sample of Blue Compact Dwarf Galaxies 12

2.2 Chandra Observations 14

2.3 VLA Observations 17

2.4 Imaging Parameters for VLA Observations 18

2.5 Host Galaxy SFRs and Expected Luminosity from XRBs 21

2.6 Hard X-ray Sources 25

2.7 Compact Radio Sources 29

3.1 Sample of Dwarf Galaxies with Mid-IR Selected Candidate AGNs 44

3.2 *WISE* magnitudes 47

3.3 *Chandra* Observations 52

3.4 X-ray Sources 54

3.5 Host Galaxy SFRs and Expected Luminosity from XRBs 58

3.6 Multiwavelength Properties of Dwarf Galaxies with Red Mid-IR Colors 64

3.7 Expected $L_{\rm X}$ from $L_{\rm IR}$ 70

3.8 Expected $L_{\rm X}$ from $L_{\rm H\alpha}$ 74

3.9 Expected $L_{\rm X}$ from $L_{\rm [O\ III]}$ 75

4.1 Sample 89

4.2 X-ray sources 94

LIST OF FIGURES

Figure Page

1.1 A simplified model of an AGN. The accretion disk is comprised of in-spiralling matter, and is responsible for the ultraviolet and visible continuum emission. The obscuring torus is made of hot dust and emits infrared radiation. Ionized gas clouds give us the broad-line and narrow-line regions; the former is closer to the central BH, which results in the broadening of the emission lines. The jet produces radio emission via synchrotron emission. Image credit: C.M. Urry & P. Padovani. `https://heasarc.gsfc.nasa.gov/docs/objects/agn/agn_model.html`. 4

2.1 SDSS color composite images of the galaxies in our sample. Each image has dimensions of $1.69' \times 1.69'$, except for (e), which has dimensions of $0.'85 \times 0.'85$. 11

2.2 VLA 5 GHz (left) and 7.4 GHz (right) images of the galaxies in our sample. The beam sizes are shown in the lower left corners. 15

2.2 Same as above. 16

2.2 Same as above. 17

2.3 X-ray luminosity vs. SFR for the galaxies. The points represent the observed X-ray luminosities (cumulative from the point sources), while the black dashed line and shaded blue area represent the expected X-ray luminosity and the 1σ scatter using the relation from Lehmer et al. (2010). The uncertainty of $\sim$0.13 dex in the SFR is shown in black in the lower right-hand corner. Note that II Zw 70 is absent from this plot as we did not significantly detect any hard X-ray sources. 28

2.4 Optical images from *HST* or the SDSS as indicated, with X-ray sources (cyan) and 5 GHz radio contours (green) overlaid. For the X-ray sources, the cyan crosses and circles mark the position of the source and the 95% positional uncertainty. The only case of spatially coincident X-ray and radio sources within the positional uncertainties is in Haro 9, between X1 and R1. 33

2.4 Same as above. 34

LIST OF FIGURES – CONTINUED

Figure Page

3.1 *WISE* color-color diagram for the dwarf galaxies in our sample. The galaxies classified as AGN, composite, and star-forming are in red, grey, and black, respectively, using the [N II]/Hα BPT diagram (left panel in Figure 3.2). In black, we plot the AGN selection box from Jarrett et al. (2011), and in orange we show the W1-W2 > 0.8 selection criterion from Stern et al. (2012). 46

3.2 Optical narrow emission line diagnostic diagrams for our galaxies. Regions are separated according to the classification scheme in Kewley et al. (2006). The galaxies falling in the AGN, composite, and star-forming regions in the leftmost diagram are in red, grey, and black, respectively. 48

3.3 Three-color *HST* images of our galaxies. Red shows the NIR image (F140W for IDs 1,4-5,7-9,11, F110W for IDs 2-3,6), green shows the optical band (F606W), and blue shows the U/UV band (F336W for IDs 1,4-5,7-9,11, F275W for IDs 2-3,6). We overlay green circles of radii $0\farcs4$ at the peak of the NIR emission in the *HST* images, as well as the positions and 95% positional uncertainties of the detected X-ray sources in magenta. The SDSS $3''$ spectroscopic apertures are shown as white circles and the resolution of the *WISE* W2-band ($6.4''$) is in red. The text in the upper left corner denotes the BPT classification of the galaxy. Note that for ID 10, *HST* imaging was unavailable, so DECaLS imaging was used instead, with red, green, and blue as the z, r, and g bands, respectively. 49

3.3 Same as above. 50

3.3 Same as above. 51

LIST OF FIGURES – CONTINUED

Figure Page

3.4 Hardness ratio vs. log 2-10 keV X-ray luminosity for the seven of our galaxies that had a detected X-ray source in at least one of the two bands. The hardness ratio was calculated using BEHR (see Section 3). The error bars are the 68% confidence intervals. Galaxies classified as AGN, composite, and star-forming are in red, grey, and black, respectively, based on the [N II]/Hα BPT diagram. Hardness ratios for unabsorbed power laws with Γ = 1.8, 2.0, and 2.5 are shown as grey solid lines, while power laws with various absorptions and Γ = 1.8 are shown as dashed grey lines. 59

3.5 Log ratio of X-ray luminosity over host galaxy SFR vs. metallicity. The crosses represent SFRs calculated with the mid-IR-corrected FUV luminosities, the dots use the uncorrected FUV luminosities (see Equation 3.1), and the stars use the Hα derived SFRs - the three are connected by a dotted line for ease of comparison. SFRs based on the mid-IR-corrected FUV luminosities may be severely overestimated if the mid-IR emission is indeed dominated by an AGN as suggested by the *WISE* colors. Similarly, the Hα SFRs are also likely overestimated for the BPT AGNs/Composites since the AGN is contributing to or dominating the line ratios. Arrows indicate upper limits on the X-ray luminosities for galaxies with no significant hard X-ray source detections (calculated from the minimum fluxes). Galaxies classified as AGN, composite, and star-forming are in red, grey, and black, respectively (using the [N II]/Hα BPT diagram). The values and error bars in blue are the expected X-ray luminosity from XRBs from Lehmer et al. (2021). The $\sim$0.18 uncertainty in the metallicities is shown in black in the lower right-hand corner. 60

LIST OF FIGURES – CONTINUED

Figure Page

3.6 *WISE* W1-W2 color vs. $g - r$ color (from Table 3.1). The galaxies classified as AGN, composite, and star-forming are in red, grey, and black, respectively, based on the [N II]/Hα BPT diagram (left panel in Figure 3.2). In orange we show the W1-W2 > 0.8 selection criterion from Stern et al. (2012). 66

3.7 Observed X-ray luminosities vs W2 (top), Hα (middle), and [O III] (bottom) luminosities for our galaxies. Galaxies classified as AGN, composite, and star-forming are in red, grey, and black, respectively. The arrows indicate that the X-ray luminosity comes from an upper limit (calculated from minimum fluxes - see Section 3). The black dashed lines indicate the expected X-ray luminosity using the Secrest et al. (2015) relation (top, mid-IR; Equation 3.3) and the relations from Panessa et al. (2006) (middle, Hα, Equation 3.4; bottom, [O III], Equation 3.5). The dark blue shaded areas represent the 1σ scatters and the light blue shaded areas represent the 3σ scatters. The dashed grey lines represent the relations shifted down by 1 and 2 dex, for ease of comparison with the plotted points. 68

LIST OF FIGURES – CONTINUED

Figure Page

3.8 Estimated intrinsic absorption ($N_{\rm H}$) in each galaxy using the difference between the expected and observed X-ray luminosities. Galaxies classified as AGN, composite, and star-forming are in red, grey, and black, respectively. The dots, x's, and plus signs use the expected X-ray luminosity as calculated from the W2, Hα, or [O III] relations, respectively. The arrows indicate that the observed X-ray luminosity comes from an upper limit calculated from minimum fluxes, which translates into a lower limit for $N_{\rm H}$. The dotted blue line at $N_{\rm H} = 10^{24}$ cm^{-2} separates out the plot into Compton thick (above the line) and Compton thin (below the line) regions. Note that several estimates of $N_{\rm H}$ are unavailable (e.g. the Hα and [O III] relations for ID 6) – in these cases, the observed X-ray luminosity was higher than the expected X-ray luminosity, so an estimate was unable to be calculated. Note also that for ID 6, Baldassare et al. (2017) found via spectral fitting that the models did not prefer an $N_{\rm H}$ greater than the Galactic value, suggesting little to no intrinsic absorption. 71

4.1 Three-color images of our galaxies retrieved from the Dark Energy Camera Legacy Survey (DECaLS; Dey et al., 2019), with red, green, and blue showing the z, r, and g bands, respectively. We overlay the positions and the corrected combined positional uncertainty (via the `RADEC_ERR_CORR` parameter from the eFEDS main catalog) in magenta. 91

4.2 The results of matching 10^5 randomly generated coordinate sets (in the eFEDS field) to the eFEDS X-ray sources. 92

4.3 Total observed X-ray luminosities of the galaxies in our sample vs. what we would expect to see from XRBs via the relation of Lehmer et al. (2010). The dashed line represents the one-to-one relation, and the scatter of 0.34 dex in the expected XRB luminosities is shown in black in the lower right corner. The error bars shown are calculated using the 1σ error approximation from Gehrels (1986). Note also that the lower error on ID 1 was consistent with no detection; this is signified by the arrow for the lower error bar. 96

ABSTRACT

Identifying and analyzing massive black holes (BHs) in dwarf galaxies can advance our understanding of the formation and development of supermassive BHs. Searching for these objects can prove troublesome, however. Massive BHs, with masses of $M_{\rm BH} \lesssim 10^6\ M_\odot$, are smaller than their supermassive cousins ($M_{\rm BH} \sim 10^6{-}10^9\ M_\odot$), and the dwarf galaxies they reside in can yield very different environments than what one might find in a more standard massive galaxy, resulting in a different set of challenges than searching out active galactic nuclei (AGN) powered by supermassive BHs. Here we describe several methods for both identifying AGN candidates powered by massive BHs and searching for evidence to confirm the presence or absence of AGN candidates in dwarf galaxies. For the latter, we use different combinations of radio, X-ray, and mid-IR observations to search for AGN signatures, elucidating the various benefits and difficulties that lie with each one, and reporting the results when applied to our varying samples. For the former, we analyze the efficacy of a mid-IR color-color AGN selection method when applied to dwarf galaxies instead of massive galaxies, and use X-ray observations from a newly-released catalog to search for new AGN candidates in dwarf galaxies.

1

INTRODUCTION

Supermassive black holes (SMBHs) with typical masses of $M_{\rm BH} \sim 10^6{-}10^9\ M_\odot$ reside at the centers of most massive galaxies (Reines, 2022; Volonteri, 2010). From high-redshift quasar observations, we know that similarly sized SMBHs in early-universe galaxies formed relatively quickly in cosmological time (< 1 Gyr; e.g. Bañados et al., 2018), yet the origins of these SMBHs remain unclear. While more modern stellar-mass BH formation mechanisms are reasonably well understood as the final stage of a particular path of massive stars' stellar evolution, the mechanisms behind the formation and development of these early SMBHs is still an area of active research (Natarajan, 2014; Volonteri, 2010). Given the relative rapidity of their growth, several different theories have arisen in explanation.

The first generation of large (population III) stars could have resulted in early SMBH seeds with light BH masses ($\lesssim 10^2\ M_\odot$) - however it would be difficult for these seeds to accrete enough mass to result in the SMBH masses we see in observations. In light of this, other possibilities have been explored. For instance, these SMBH seeds could have arisen from interactions within dense star clusters (Antonini et al., 2019; Portegies Zwart et al., 2004; Tagawa et al., 2020), resulting in seeds with mass ranges of $\sim 10^2{-}10^4\ M_\odot$, or, alternatively, could have formed via direct collapse of giant dense gas clouds (Inayoshi et al., 2020), which would result in seed masses of $\sim 10^5\ M_\odot$ (Greene, 2012).

Ideally, we would undertake direct observations of early-universe galaxies to gain insight into the mass ranges these SMBH seeds spanned. Unfortunately, given how distant and faint these galaxies are, this is not a feasible avenue of exploration given current technological limitations - though the advent of new telescopes, such as the *James Webb Space Telescope* (*JWST*) and the *Laser Interferometer Space Antenna* (*LISA*) could help in this regard in

the future.

With these restrictions in mind, we turn instead to dwarf galaxies. Dwarf galaxies are generally defined as galaxies with stellar masses at most similar to that of the Large Magellanic Cloud (Reines et al., 2013), with $M_{\rm stellar} \lesssim 10^{9.5}\ M_{\odot}$; i.e. low-mass galaxies. In contrast with early-universe galaxies, dwarf galaxies can be found relatively close by and are thus more feasibly observed. We know that dwarf galaxies can host massive or intermediate-mass black holes (BHs; Reines et al., 2013, 2011), which in this context simply means BHs more massive than stellar-mass BHs and less massive than SMBHs, with masses $M_{\rm BH} \lesssim 10^{6}\ M_{\odot}$. These central BHs in dwarf galaxies have not grown to the same extent as their more widespread SMBH cousins as dwarf galaxies have relatively quiet histories when it comes to mergers (Volonteri et al., 2008). Additionally, BH growth is thought to be negatively impacted by supernova feedback, which could hamper the growth of massive BHs in dwarf galaxies (Anglés-Alcázar et al., 2017; Habouzit et al., 2017).

As dwarf galaxies play host to the smallest massive BHs, they can prove helpful in discriminating between different theories of SMBH seed formation. Scaling relations between galaxy stellar mass and host BH mass show that the lightest massive BHs live in dwarf galaxies (Reines & Volonteri, 2015), and BH growth models running on cosmological time scales predict that observational traces of the principal seeding mechanism will persist in the present day population of dwarf galaxies. Given that we expect smaller seeds to be more common than more massive BH seeds, the fraction of dwarf galaxies hosting massive BHs (i.e. the occupation fraction) can help shed light on the formation of SMBH seeds (Volonteri et al., 2008). Additionally, how the aforementioned scaling relation between BH and galaxy stellar mass appears at smaller masses would be affected by these different seeding scenarios. Heavy seeds would cause this relation to flatten towards an observable asymptote in BH mass e.g. $10^{5}\ M_{\odot}$, as in the direct collapse scenario, while light seeds would likely push this asymptote below observable levels (Reines & Volonteri, 2015; van Wassenhove et al., 2010;

Volonteri & Natarajan, 2009).

The problem now becomes how to find and observe these massive BHs. BHs, even massive ones, are difficult to directly observe as they have a relatively small gravitational sphere of influence and do not emit light on their own (Hawking radiation not withstanding). Instead what we would observe is an active galactic nucleus (AGN), which is a combination of the BH and the surrounding environment. It is the surrounding material that emits the light we see. A model of this is shown in Figure 1.1.

From observations of an AGN at various wavelengths, we can then infer knowledge about the BH at the center of the system. This sub-field is relatively new; work ignited after the discovery of the first detected massive BH in the dwarf starburst galaxy Henize 2-10 in Reines et al. (2011), so different techniques are still being tested and applied to the problem of detecting these massive BHs. This thesis focuses on using observations in different wavelength bands to apply a few of these techniques to the problem of detecting massive BHs in dwarf galaxies.

In Chapter 2 we use combined radio and X-ray observations to search for signs of a low-luminosity AGN in a sample of five blue compact dwarf galaxies. We look for spatially coincident radio and X-ray sources; if the emission in both bands is sourced by a single object, we can use the ratio of radio to X-ray luminosity to infer properties about said object, and how likely it is to be an AGN. The work presented in this chapter was published in the Astrophysical Journal (Latimer et al., 2019).

In Chapter 3 we focus on evaluating a specific mid-infrared (mid-IR) color-color diagnostic that uses observations from the *Wide-field Infrared Survey Explorer* (*WISE*) to search for AGN candidates. We use optical emission lines and high-resolution X-ray observations to search for signs of accreting massive BHs in a sample of 11 dwarf galaxies that were selected as potential AGN candidates using this mid-IR diagnostic in Hainline et al. (2016), with the goal of evaluating the efficacy of this diagnostic technique on dwarf

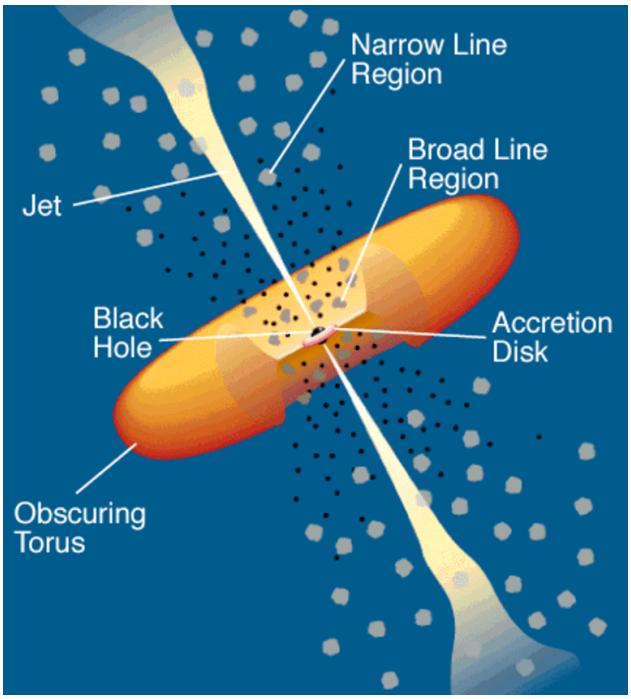


Figure 1.1 A simplified model of an AGN. The accretion disk is comprised of in-spiralling matter, and is responsible for the ultraviolet and visible continuum emission. The obscuring torus is made of hot dust and emits infrared radiation. Ionized gas clouds give us the broad-line and narrow-line regions; the former is closer to the central BH, which results in the broadening of the emission lines. The jet produces radio emission via synchrotron emission. Image credit: C.M. Urry & P. Padovani. `https://heasarc.gsfc.nasa.gov/docs/objects/agn/agn_model.html`.

galaxies. The work presented in this chapter was published in the Astrophysical Journal (Latimer et al., 2021b).

In Chapter 4 we search for potential AGN candidates in dwarf galaxies using the recently released eROSITA Final Equatorial Depth Survey (eFEDS) X-ray catalog of $\sim$28,000 X-ray sources that were drawn from observations from the performance verification phase of the recently launched eROSITA X-ray telescope. This catalog covers an area on the sky of $\sim$140

deg^2 (1/300th of the sky), and we extrapolate our results to an upcoming future all-sky X-ray survey by the eROSITA telescope to estimate how many new potential dwarf galaxy AGN candidates it could bring. The work presented in this chapter was published in the Astrophysical Journal Letters (Latimer et al., 2021a).

Finally, in Chapter 5 we summarize our work and draw conclusions as to how it affects the field as a whole. We further discuss the generalized difficulties in detecting low-luminosity AGN in dwarf galaxies, and lay out possible avenues of approach that future research might take.

AN X-RAY + RADIO SEARCH FOR MASSIVE BLACK HOLES IN BLUE COMPACT DWARF GALAXIES

Contribution of Authors and Co-Authors

Manuscript in Chapter 2

Author: Lilikoi J. Latimer

Contributions: Analyzed the radio data and performed multi-wavelength synthesis of analyzed data. Wrote the initial draft of the manuscript.

Author: Amy E. Reines

Contributions: Advised, helped edit the manuscript, provided scientific and editorial comments on the manuscript.

Author: Richard M. Plotkin

Contributions: Analyzed and reduced X-ray data, provided scientific and editorial comments on the manuscript.

Author: Thomas D. Russell

Contributions: Reduced the radio data, provided scientific and editorial comments on the manuscript.

Author: James J. Condon

Contributions: Provided scientific and editorial comments on the manuscript.

Manuscript Information

Lilikoi J. Latimer, Amy E. Reines, Richard M. Plotkin, Thomas D. Russell, James J. Condon

The Astrophysical Journal

Status of Manuscript:
____ Prepared for submission to a peer-reviewed journal
____ Officially submitted to a peer-reviewed journal
____ Accepted by a peer-reviewed journal
_X_ Published in a peer-reviewed journal

IOP Publishing
The Astrophysical Journal, Volume 884, Number 1
10.3847/1538-4357/ab3289

Introduction

Over the past several years there has been mounting evidence for the existence of massive black holes (BHs) in at least some dwarf galaxies (e.g., Baldassare et al., 2018; Baldassare et al., 2015, 2017, 2016; Dickey et al., 2019; Hainline et al., 2016; Lemons et al., 2015; Moran et al., 2014; Nguyen et al., 2019; Pardo et al., 2016; Reines et al., 2013, 2014, 2011; Schramm et al., 2013). This has important implications for the formation and growth of the first "seeds" of supermassive black holes that are ubiquitous in today's massive galaxies (e.g., Kormendy & Ho, 2013; Kormendy & Richstone, 1995). For example, present-day BH-host galaxy scaling relations at low masses and the BH occupation fraction in dwarf galaxies are predicted to be strong discriminants between seeds that were heavy ($\sim 10^5 M_\odot$) or light ($\sim 10^2 M_\odot$) (e.g., Greene, 2012; Ricarte & Natarajan, 2018; Volonteri, 2010).

While there has been recent progress on the observational front, the BH occupation fraction in dwarf galaxies is not yet well determined (although see Miller et al., 2015) and we know very little about the types of dwarf galaxies that may be preferential hosts to massive BHs. Dwarf galaxies come in a variety of flavors, including star-forming irregulars, spirals and blue compact dwarfs, early-type ellipticals and ultracompact dwarfs, and dark-matter-dominated dwarf spheroidals and ultra-faint dwarfs. So far the largest samples of massive BHs in dwarf galaxies have been found by applying optical emission line diagnostics (e.g., BPT selection and broad Hα; Reines et al., 2013) to Sloan Digital Sky Survey (SDSS) spectroscopy. However, these types of optical searches are biased towards active BHs that are more easily observed, such as those with high Eddington ratios and those that are unobscured by star formation. Indeed, the host galaxies of the Reines et al. (2013) sample tend to have bright nuclear point sources (from the active galactic nuclei, i.e., AGN), regular morphologies, and little ongoing star formation (Kimbrell et al., 2021; Schutte et al., 2019). This is similar to the slightly more massive counterparts in the earlier sample of Greene &

Ho (2007).

Given that our understanding of the demographics of massive BHs in different categories of dwarf galaxies is quite limited, and the surprising discovery of a massive BH in the blue compact dwarf (BCD) galaxy Henize 2-10 (Reines et al., 2011), we have observed a small sample of BCDs using X-ray and radio observations. High-resolution observations from the *Chandra X-ray Observatory* and the Karl G. Jansky Very Large Array (VLA) are especially well-suited to searching for weakly accreting massive BHs and those residing in star-forming host galaxies, as exemplified by detailed studies of Henize 2-10 (Reines & Deller, 2012; Reines et al., 2016, 2011) that reveal a spatially coincident compact, non-thermal radio and X-ray point source at the center of the galaxy.[1] Moreover, BCDs are characterized by blue colors, low metallicities, and concentrated regions of intense star formation (e.g. Gil de Paz et al., 2003), making them our best local analogues of low-mass, physically small, gas-rich, star-forming galaxies in the earlier Universe, where the first BH seeds likely formed.

Sample of Blue Compact Dwarf Galaxies

Our target galaxies are taken from the sample of BCDs from Gil de Paz et al. (2003). Gil de Paz et al. (2003) propose that a galaxy must fulfill the following observational criteria in order to be classified as a BCD: (1) blue with $\mu_{B,\rm peak} - \mu_{R,\rm peak} \lesssim 1$ mag arcsec^{-2}, (2) compact with $\mu_{B,\rm peak} < 22$ mag arcsec^{-2}, and (3) a dwarf with $M_K > -21$ mag. This definition separates the BCDs from other types of dwarf galaxies such as dwarf irregulars and dwarf ellipticals. Given that our search technique depends on high-resolution X-ray and radio observations, we adopted two complementary strategies for selecting our target BCDs from Gil de Paz et al. (2003).

First, we selected galaxies detected at 1.4 GHz in the Faint Images of the Radio Sky at

[1] Although see Hebbar et al. (2019) who argue for a supernova remnant origin. We defer a detailed discussion of this object to a forthcoming paper.

Twenty-cm (FIRST) survey (Becker et al., 1995) with distances < 20 Mpc. BCDs detected by FIRST are preferred targets since they must either have an AGN and/or intense star formation to produce the observed radio emission on scales of $\sim 5''$, making them good analogues of Henize 2-10. The distance cut was applied to retain both sensitivity to low luminosities and fine enough spatial resolution to accurately determine if X-ray and radio sources are co-incident. Out of the 80 BCDs in Gil de Paz et al. (2003) covered by the FIRST survey area, four galaxies met these selection criteria: Haro 3, Haro 9, Mrk 709[2] and II Zw 70. These four BCDs were the subject of a joint *Chandra*–VLA proposal (PI: Reines; CXO proposal number 13700563, VLA project SD0563). Our study of Mrk 709, and its candidate massive BH, has previously been presented in Reines et al. (2014).

To expand our sample, we also searched for BCDs in the sample of Gil de Paz et al. (2003) with available observations in the *Chandra* archive. We found 18 galaxies with *Chandra* coverage and, after obtaining and inspecting these data, found five BCDs with detectable hard X-ray point sources worthy of radio follow-up with the VLA (any existing VLA archival data were not deep enough and/or lacked sufficient resolution to meet our requirements). We proposed for VLA observations of these preferred targets with existing X-ray sources, however only two (Mrk 996 and SBS 0940+544) were ultimately observed for this project (PI Reines; VLA project 12B-206) due to scheduling priorities. We did not propose for the remaining 13 galaxies without detectable *Chandra* point sources since we are primarily interested in finding spatially coincident X-ray and radio sources as a signpost of massive BH accretion.

Our final sample consists of five BCD galaxies (see Figure 2.1) and their properties are given in Table 2.1. Note that while distances from Gil de Paz et al. (2003) were used to initially select our sample, in our analysis here we use distances derived from redshifts in the

[2]The distance of 15.7 Mpc for Mrk 709 provided in Gil de Paz et al. (2003) (from NED) was incorrect. Reines et al. (2014) present a redshift of $z = 0.052$ ($d \sim 214$ Mpc) based on SDSS spectroscopy.



(a) II Zw 70 (b) Haro 3 (c) Haro 9 (d) Mrk 996 (e) SBS 0940+544

Figure 2.1 SDSS color composite images of the galaxies in our sample. Each image has dimensions of $1.69' \times 1.69'$, except for (e), which has dimensions of $0\farcm85 \times 0\farcm85$.

NASA-Sloan Atlas[3] (NSA) with $h = 0.73$.

[3] `http://nsatlas.org`, version 0.1.2

Table 2.1. Sample of Blue Compact Dwarf Galaxies

Galaxy	R.A.	Decl.	$N_{\rm H}$ (10^{20} cm^{-2})	z	r_{50} (kpc)	Distance (Mpc)	M_g (mag)	$g-i$ (mag)	log $M_\star/M_\odot$
(1)	(2)	(3)	(4)	(5)	(6)	(7)	(8)	(9)	(10)
II Zw 70	14 50 56.5	+35 34 18	1.16	0.00470	0.30	19.31	−16.98	−0.289	7.82
Haro 3	10 45 22.4	+55 57 37	0.66	0.00409	0.61	16.81	−18.21	−0.062	8.58
Haro 9	12 45 17.1	+27 07 32	0.71	0.00443	0.84	18.18	−18.92	0.103	8.93
Mrk 996	01 27 35.5	−06 19 36	3.83	0.00491	0.46	20.18	−17.38	0.081	8.28
SBS 0940+544	09 44 16.6	+54 11 34	1.34	0.00652	0.83	26.78	−15.97	−0.256	7.58

Note. — Column 1: galaxy name. Column 2: right ascension in units of hours, minutes, seconds (J2000). Column 3: declination in units of degrees, arcminutes, arcseconds (J2000). Column 4: galactic neutral hydrogen column density. Column 5: redshift, specifically the `zdist` parameter from the NSA. Column 6: Petrosian 50% light radius. Column 7: distance estimate from `zdist`. Column 8: absolute g-band magnitude corrected for foreground Galactic extinction. Column 9: $g-i$ color. Column 10: log galaxy stellar mass. The values given in columns 5-10 are from the NSA[4] and we assume $h = 0.73$.

Observations and Data Reduction

Chandra X-ray Observatory

X-ray observations of our target galaxies were taken with *Chandra* between 2009 Sep 03 and 2012 Dec 31. Exposure times were between 16.8 ks and 53.3 ks. A summary of the *Chandra* X-ray observations is given in Table 2.2.

Each dwarf galaxy was placed at the aimpoint of the ACIS S3 chip. We used the *Chandra* Interactive Analysis of Observations (`CIAO`) software v4.7 (Fruscione et al., 2006) to reduce each observation. We first reprocessed the data by applying calibration files (CALDB 4.6.7), and we determined that no observations were affected by background flares.

We then aligned each *Chandra* observation to the optical SDSS astrometric frame, using the `CIAO` tool `reproject_aspect`. To align the astrometry, we created a list of X-ray point sources on the S3 chip by running the point source detection algorithm `wavdetect` on a *Chandra* image filtered from 0.5-7 keV. We then excluded all X-ray sources falling within $3r_{50}$ of the dwarf galaxy, and we correlated the remaining X-ray sources to optical point sources in the SDSS DR12 with $i < 22$ mag. We found 2-5 common X-ray and optical point sources on the S3 chip for each observation. Given the small number of common sources, we only applied a translation correction to the *Chandra* images in the x,y directions. The applied astrometric shifts range from $\pm$0.01-1.3 pixels, and the median shifts across all five observations were $|\Delta x| = 0.2$ and $|\Delta y| = 0.4$ pixels ($0\farcs1$ and $0\farcs2$, respectively).

Karl G. Jansky Very Large Array

Observations of our sample of galaxies were taken with the VLA in its extended A-configuration between 2012 December 1 and 2013 January 1. The observations typically provided between 50 minutes and 90 minutes of on source time (see Table 2.3). All observations were taken at C-band with two 1-GHz wide basebands centered at 5.0 and

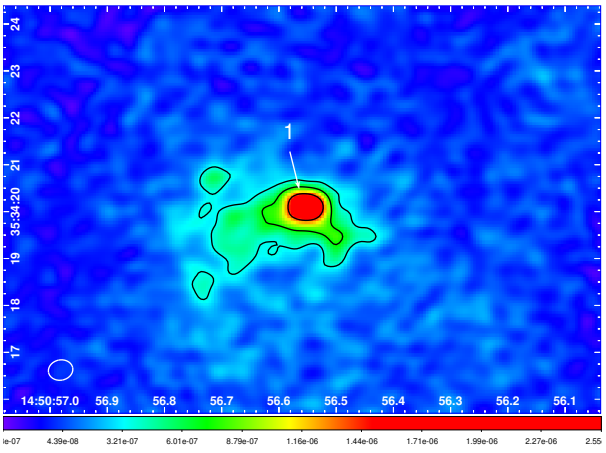
Table 2.2. Chandra Observations

Galaxy	Date observed	Obs ID	Exp. time (ks)	$N_{\rm background}$
II Zw 70	2011 Nov 06	13930	30.6	0.033
Haro 3	2012 Dec 31	13927	17.8	0.131
Haro 9	2012 Nov 13	13928	16.8	0.176
Mrk 996	2009 Sep 03	11567	53.3	0.104
SBS 0940+544	2010 Jan 18	11288	16.8	0.079

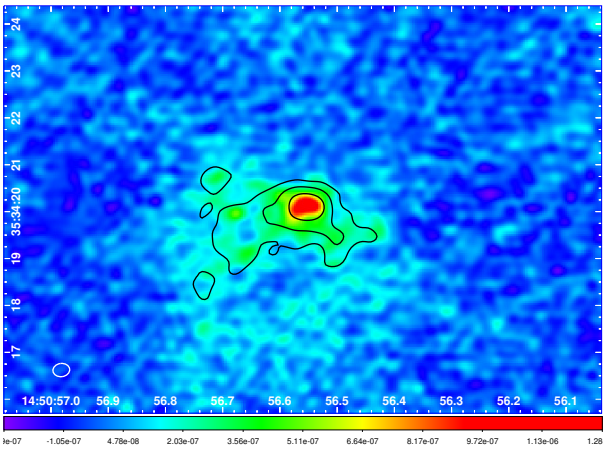
Note. — $N_{\rm background}$ is the number of expected 2-10 keV $N(>S)$ background sources within $3r_{50}$, using Moretti et al. (2003).

7.4 GHz, each comprised of eight 128-MHz sub-bands containing 64 spectral channels of width 2-MHz. The primary (bandpass and amplitude) and secondary (phase) calibrators are given in Table 2.3.

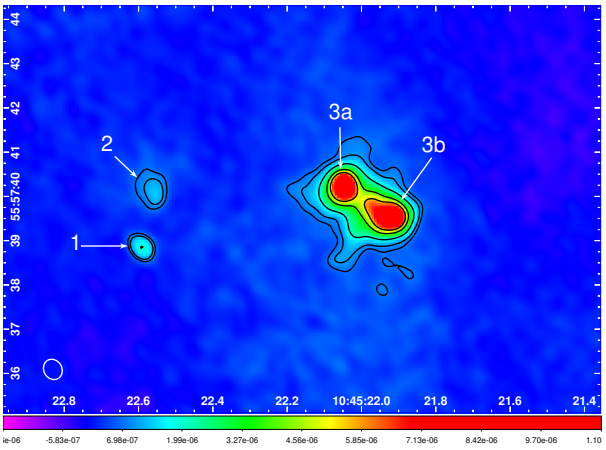
The data were edited and calibrated following standard procedures within the Common Astronomy Software Application (CASA; McMullin et al., 2007). Using natural weighting for maximum sensitivity, we imaged the calibrated data separately at 5.0 and 7.4 GHz (Figure 2.2), where deconvolution (cleaning) was carried out with the multi-frequency synthesis algorithm within CASA. The RMS noise and beam parameters are given for each image in Table 2.4. We also explored different antenna weightings, and used UV-cuts to filter out diffuse emission (as well as match spatial sensitivity between the 5.0 and 7.4 GHz images). However, these did not alter the results, and, therefore, we only present the images using natural weighting to maximize the sensitivity. The absolute astrometry of the VLA observations is accurate to $\lesssim 0\farcs1$.



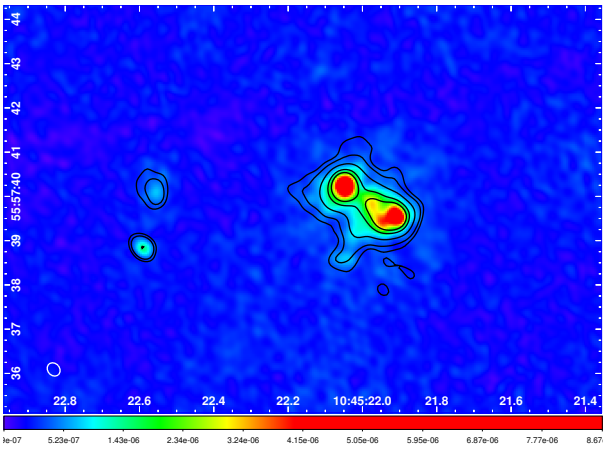
(a) II Zw 70 VLA 5 GHz image with contour levels of $(\sqrt{2})^n$ times the RMS noise, where $n = 5$, 7, and 9.



(b) II Zw 70 VLA 7.4 GHz image with the 5 GHz contour levels overlaid.

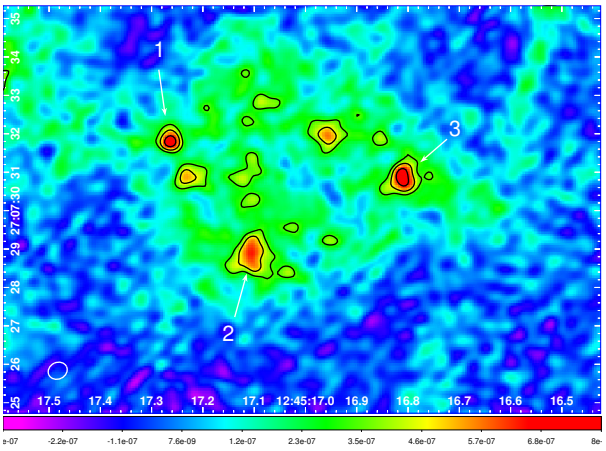


(c) Haro 3 VLA 5 GHz image with contour levels of $(\sqrt{2})^n$ times the RMS noise, where $n = 4$, 5, 7, 9, and 10.

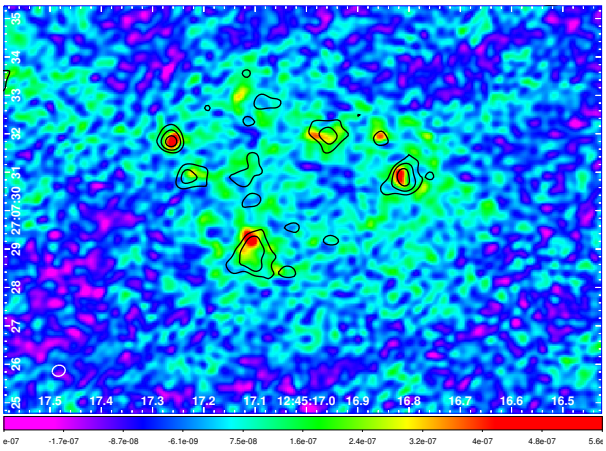


(d) Haro 3 VLA 7.4 GHz image with the 5 GHz contour levels overlaid.

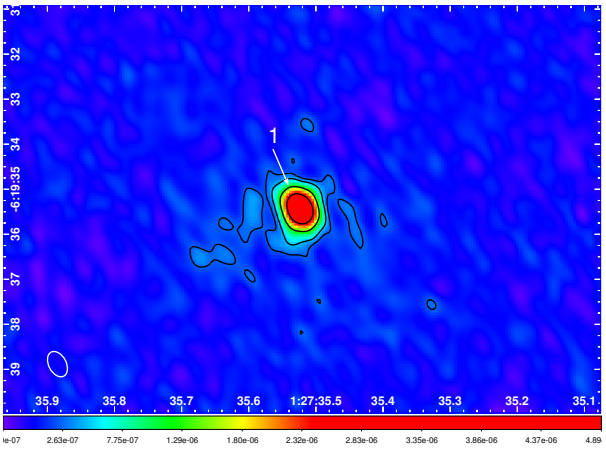
Figure 2.2 VLA 5 GHz (left) and 7.4 GHz (right) images of the galaxies in our sample. The beam sizes are shown in the lower left corners.



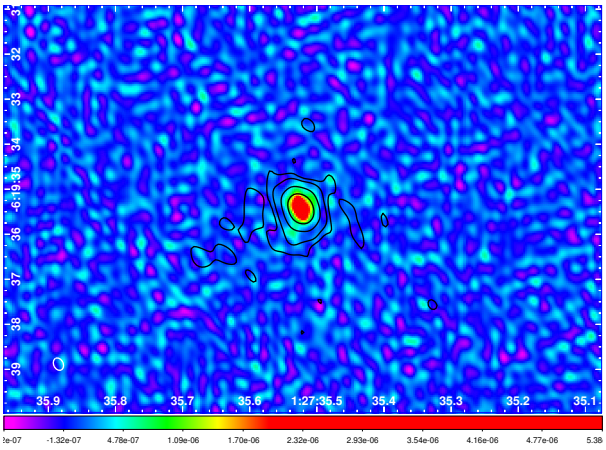
(e) Haro 9 VLA 5 GHz image with contour levels of $(\sqrt{2})^n$ times the RMS noise, where $n = 4$, 5, and 6.



(f) Haro 9 VLA 7.4 GHz image with the 5 GHz contour levels overlaid.

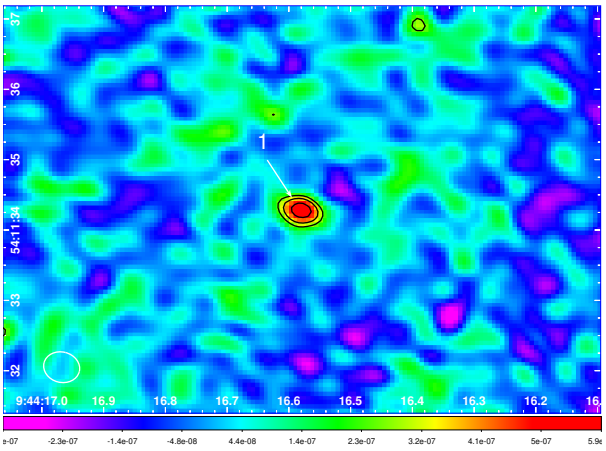


(g) Mrk 996 VLA 5 GHz image with contour levels of $(\sqrt{2})^n$ times the RMS noise, where $n = 3$, 5, 8, and 10.

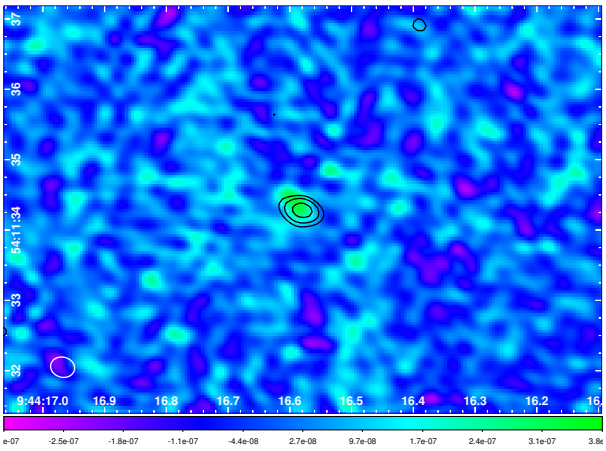


(h) Mrk 996 VLA 7.4 GHz image with the 5 GHz contour levels overlaid.

Figure 2.2 Same as above.



(i) SBS 0940+544 VLA 5 GHz image with contour levels of $(\sqrt{2})^n$ times the RMS noise, where $n = 4$, 5, and 6.



(j) SBS 0940+544 VLA 7.4 GHz image with the 5 GHz contour levels overlaid.

Figure 2.2 Same as above.

Table 2.3. VLA Observations

Galaxy	Date Observed	Project Code	Flux Calibrator	Phase Calibrator	Obs. Time
II Zw 70	2012 Dec 01	SD0563	3C 286	J1416+3444	90
Haro 3	2012 Dec 02	SD0563	3C 286	J1035+5628	50
Haro 9	2012 Dec 01	SD0563	3C 286	J1221+2813	80
Mrk 996	2013 Jan 01	12B-206	3C 48	J0110−0741	90
SBS 0940+544	2012 Dec 24	12B-206	3C 147	J0932+5306	50

Note. — All observations were taken at C-band while the VLA was in the A-configuration. The observing time is the time on the source, in minutes.

Table 2.4. Imaging Parameters for VLA Observations

Galaxy	ν (GHz)	Synthesized Beam (arcsec)	P.A. (deg)	rms Noise (μJy beam^{-1})
(1)	(2)	(3)	(4)	(5)
II Zw 70	5.0	0.52 × 0.43	−78.7	4.5
···	7.4	0.36 × 0.28	−83.0	4.3
Haro 3	5.0	0.47 × 0.41	30.2	10.4
···	7.4	0.32 × 0.27	40.5	5.7
Haro 9	5.0	0.51 × 0.43	−65.1	5.6
···	7.4	0.34 × 0.28	−74.2	4.4
Mrk 996	5.0	0.60 × 0.39	27.9	4.6
···	7.4	0.29 × 0.21	25.2	7.6
SBS 0940+544	5.0	0.52 × 0.43	75.9	5.9
···	7.4	0.35 × 0.29	75.1	5.2

Note. — Column 1: galaxy name. Column 2: rest frequency. Column 3: beam major axis × beam minor axis. Column 4: beam position angle. Column 5: RMS noise of the image. All images were produced using natural weighting for maximum sensitivity.

Optical Images

We obtained optical images of our target galaxies for comparison with the X-ray and radio observations. SDSS color composite images of the BCDs are shown in Figure 2.1. We also retrieved archival *Hubble Space Telescope (HST)* WFPC2 broadband images of three galaxies (Haro 3, Haro 9, and Mrk 996) from the Hubble Legacy Archive. The absolute astrometry of the *HST* images was adjusted to match the SDSS using common sources in each image. The astrometric corrections were $\lesssim 0\farcs2$.

Analysis and Results

Host Galaxies and Star Formation Rates

The five galaxies in our sample (see Figure 2.1) span a stellar mass range of $\sim 10^{7.6}-10^{8.9}$ $M_\odot$, with a median of $\sim 10^{8.3}$ $M_\odot$. It is worth noting that these galaxies have more irregular morphologies and significantly lower stellar masses than previous samples of dwarf galaxies found to host AGNs (e.g., Reines et al., 2013). The galaxies are also physically small, with half-light radii less than 1 kpc. All of the galaxies are relatively nearby, with distances in the range of ∼17-27 Mpc (using the `zdist` parameter in the NSA and adopting $h_0 = 0.73$). See Table 2.1 for information on the individual galaxies.

In general, BCDs are experiencing regions of intense star formation. We estimate the star formation rates (SFRs) of our target BCD galaxies using far-UV (FUV; 1528 Å) and mid-infrared (IR; 25 μm) luminosities via

$$\begin{aligned} \log \mathrm{SFR}(M_\odot\ \mathrm{yr}^{-1}) &= \log L(\mathrm{FUV})_{\mathrm{corr}} - 43.35 \\ \log L(\mathrm{FUV})_{\mathrm{corr}} &= L(\mathrm{FUV})_{\mathrm{obs}} + 3.89 L(25\ \mu\mathrm{m}) \end{aligned} \tag{2.1}$$

(Hao et al., 2011; Kennicutt & Evans, 2012; Murphy et al., 2011). We obtain FUV magnitudes from the *Galaxy Evolution Explorer* (*GALEX*), and 22 μm magnitudes from

the *Wide-field Infrared Survey Explorer* (*WISE*) (Wright et al., 2010). While the Hao et al. (2011) relation uses 25 μm luminosities from the *Infrared Astronomical Satellite* (*IRAS*), only three of the galaxies in our sample had *IRAS* detections while all five were detected by *WISE*. Therefore, we use 22 μm flux densities as a proxy for 25 μm flux densities as this ratio is expected to be of order unity (Jarrett et al., 2013). The resulting estimates for the SFRs are summarized in Table 2.5. The SFRs span $\sim$0.03-0.87 $M_\odot$ yr^{-1}, with a median of $\sim$0.27 $M_\odot$ yr^{-1}. The uncertainty in this method is $\sim$0.13 dex.

The specific star formation rates (sSFR=SFR/$M_\star$) of these BCDs are quite high. Using SFRs calculated above and stellar masses from the NSA, we estimate log sSFRs in the range -9.1 to -8.4 yr^{-1}. This is comparable to or greater than other dwarf galaxies with AGN candidates such as Mrk 709 and Henize 2-10 (which have log sSFRs of -8.6 and -9.3 yr^{-1}, respectively; Reines et al., 2014, 2011) and an order or two of magnitude higher than that of the Large Magellanic Cloud (log sSFR ~ -10 yr^{-1}; van der Marel et al., 2002; Whitney et al., 2008).

Table 2.5. Host Galaxy SFRs and Expected Luminosity from XRBs

Galaxy	FUV (mag)	log L(FUV) (erg s^{-1})	W_{22} (mag)	log L(22 μm) (erg s^{-1})	SFR_{FUV} ($M_\odot$ yr^{-1})	log sSFR	log $L^{XRB}_{2-10\ keV}$ (erg s^{-1})
(1)	(2)	(3)	(4)	(5)	(6)	(7)	(8)
II Zw 70	14.79	42.6	4.92	41.7	0.27	−8.4	39.0
Haro 3	14.30	42.7	2.50	42.6	0.87	−8.6	39.4
Haro 9	13.53	43.0	3.96	42.1	0.69	−9.1	39.4
Mrk 996	16.47	42.0	4.85	41.8	0.15	−9.1	38.8
SBS 0940+544	17.79	41.7	8.07	40.8	0.03	−9.1	38.2

Note. — Column 1: galaxy name. Column 2: FUV AB magnitudes from *GALEX* (through the NSA). Column 3: log FUV luminosities. Column 4: *WISE* magnitudes[5]. Column 5: log 22 μm luminosities. Column 6: estimated SFRs from *GALEX* and *WISE* data. Column 7: log specific SFRs (sSFR=SFR/$M_\star$) in units of yr^{-1}. Column 8: log total expected 2-10 keV luminosity from high-mass XRBs.

Hard X-ray Sources

We search for hard X-ray sources to identify the presence of an accreting BH, compared to star formation which produces high-energy radiation predominantly in the soft X-ray band. To identify hard X-ray sources in our sample of BCDs, we re-run `wavdetect` on (astrometrically corrected) hard images of the S3 chip filtered from 2-7 keV. We adopt wavelet scales of 1.0, 1.4, 2.0, 2.8, 4.0 pixels, a point spread function map describing the 39% enclosed energy fraction at 4 keV, and a significance threshold of 10^{-6} (corresponding to approximately one expected false point source detection across the S3 chip). We then restrict the list of hard X-ray sources identified by `wavdetect` to those that are located within $3r_{50}$ (Petrosian 50% light radii) of the galaxy optical center. How we assess the statistical significance of each hard X-ray source detection is described below.

We extract source counts within circular apertures centered on each source, with aperture radii of 3 pixels ($1\farcs5$). These apertures correspond to the 90% enclosed energy fraction at 4.5 keV at the S3 aimpoint (all X-ray sources are located $< 0\farcm5$ from the aimpoint). We adopt these (relatively small) 90% circular apertures to avoid contamination from nearby sources and we visually examine each image to confirm that there is no contamination within any source aperture.

The number of background counts per pixel is estimated by using a circular aperture with 25 arcsec radius centered on a manually selected source-free region of the chip near each galaxy. We consider a source to be detected if the source counts are above the background level within each source aperture at the >95% confidence level, following the Kraft et al. (1991) Bayesian formalism for Poisson counting statistics in the presence of a background. Only one `wavdetect` source in Haro 3 fails to meet this detection criterion.

Finally, after subtracting the expected number of background counts in each source aperture from the total counts, a 90% aperture correction is applied to calculate the net counts and net count rates from each source. A total of 10 hard X-ray sources are detected

in four galaxies (none are found in II Zw 70), and their properties are reported in Table 2.6. Note that we exclude an additional source (X2 in SBS 0940+544) from further analysis, as it is likely a background quasar. This source is ∼20 arcsec away from the main body of the galaxy and it appears in the Milliquas catalog of Flesch (2015) under object name SDSS J094418.57+541141.4 with a photometric redshift of ∼1.6.

The uncertainty of each hard X-ray position is quoted as the radius of the 95% error circle, as determined from Equation 5 of Hong et al. (2005), who ran simulations to determine the positional accuracy of sources detected by `wavdetect` as a function of counts and location on the ACIS detector. Error bars on counts are quoted at the 90% confidence level. For sources with <10 total counts, errors are calculated following Kraft et al. (1991), which incorporates the number of background counts in each source aperture. If ≥10 total counts, then we assume the background is negligible (all source apertures contain <0.5 background counts), and we adopt the 90% confidence interval from Gehrels (1986).

Unabsorbed hard X-ray fluxes are calculated from 2-10 keV using the Portable, Interactive Multi-Mission Simulator (PIMMS)[6]. We adopt the Galactic column density from the Dickey & Lockman (1990) maps, and we assume a power-law spectral model with photon index $\Gamma = 1.8$, which is typical for low-luminosity AGN (Ho, 2008, 2009) and ultraluminous X-ray sources (Swartz et al., 2008). Unabsorbed fluxes and corresponding luminosities are reported in Table 2.6. We ignore any potential absorption that is intrinsic to the source and/or host dwarf galaxy, hence these fluxes and luminosities should be considered lower limits.

Finally, we determine that there is a low probability of any of the detected hard X-ray sources in Table 2.6 being a chance alignment of a resolved X-ray source from the cosmic X-ray background. We estimate the minimum 2-10 keV (unabsorbed) flux sensitivity of each observation that corresponds to detecting 3 hard X-ray counts (i.e., the 1-sided 95%

[6] `http://heasarc.gsfc.nasa.gov/docs/software/tools/pimms.html`

confidence limit assuming no background), given the exposure time of each observation and the Galactic column density toward each galaxy (and assuming $\Gamma = 1.8$). The flux sensitivities range from $S_{\rm min}$=1-4$\times10^{-15}$ erg s^{-1} cm^{-2} for our five *Chandra* observations. We then use the resolved cosmic X-ray background $\log N - \log S$ relation of Moretti et al. (2003) to estimate $N\,(> S_{\rm min})$, the cumulative number of 2-10 keV X-ray sources per deg^2 with a flux $> S_{\rm min}$. Based on these $N\,(> S_{\rm min})$ estimates, the expected number of background sources to fall within $3r_{50}$ of each galaxy's optical center is small, ranging from 0.01-0.2 for each of the five galaxy targets.

Our observed 2-10 keV X-ray luminosities range from $\log L_{2-10{\rm keV}}({\rm erg\ s^{-1}}) \sim 38 - 39.5$ (Table 2.6). Most of our X-ray sources lack optical counterparts, with the exceptions of X1 in Haro 9 and X2 in SBS 0940+544. Two of the galaxies in our sample (with archival *Chandra* data) have previously detected X-ray sources. Georgakakis et al. (2011) searched Mrk 996 for indications of an intermediate mass BH using *Chandra* data, finding no conclusive evidence for one. They detected the same X-ray source presented here (X1) with $L_{0.3-10{\rm keV}} = 1.2\times10^{39}$ erg s^{-1}, about an order of magnitude higher than the 2-10 keV luminosity we report, as well as another less luminous off-nuclear X-ray source (that we did not detect in the hard 2-10 keV band) with $L_{0.3-10{\rm keV}} = 1.8 \times 10^{38}$ erg s^{-1}. Prestwich et al. (2013) detected an X-ray source in SBS 0940+544 (X1 in this paper) with $L_{0.3-8{\rm keV}} = 1.26 \times 10^{39}$ erg s^{-1}. While we use the same *Chandra* data as Georgakakis et al. (2011) and Prestwich et al. (2013), the reported source luminosities differ due to the different energy ranges considered.

Table 2.6. Hard X-ray Sources

Source ID	R.A. (deg)	Decl. (deg)	p_{err} (arcsec)	Net Counts	$N_{\rm bg}$ Counts	$F_{2-10\ \rm keV}$ (10^{-15} erg s^{-1} cm^{-2})	log $L_{2-10\ \rm keV}$ (erg s^{-1})
(1)	(2)	(3)	(4)	(5)	(6)	(7)	(8)
Haro 3−X1	161.346025	55.954587	0.34	76.39 ± 14.94	0.12	90.07	39.5
Haro 3−X2	161.341482	55.961223	0.42	$13.11^{+7.69}_{-5.34}$	0.12	15.46	38.7
Haro 3−X3	161.341573	55.959588	0.47	8.65 ± 4.75	0.12	10.20	38.5
Haro 3−X4	161.346679	55.961958	0.49	7.64 ± 4.45	0.12	9.01	38.5
Haro 3−X5	161.354910	55.961723	0.94	4.31 ± 3.46	0.12	5.08	38.2
Haro 9−X1	191.322023	27.125507	0.35	45.49 ± 11.68	0.08	56.59	39.4
Haro 9−X2	191.320506	27.126089	0.39	20.19 ± 8.02	0.08	25.12	39.0
Haro 9−X3	191.320973	27.126501	0.39	19.28 ± 7.86	0.08	23.98	39.0
Mrk 996−X1	21.898420	−6.325036	0.52	6.72 ± 4.51	0.47	2.66	38.1
SBS 0940+544−X1	146.068446	54.192835	0.40	16.58 ± 7.34	0.12	20.69	39.2

Note. — Column 1: hard X-ray source identification. Column 2: right ascension. Column 3: declination. Column 4: 95% positional uncertainty. Column 5: net counts in the 2-7 keV energy range, after applying a 90% aperture correction. Error bars represent 90% confidence intervals. Column 6: number of background counts expected within each source extraction circle (after applying a 90% aperture correction). Column 7: 2-10 keV flux corrected for Galactic absorption. Column 8: log 2-10 keV luminosity corrected for Galactic absorption.

Expected Contribution from X-ray Binaries The luminosities of our detected X-ray sources ($L_{2-10\mathrm{keV}} \sim 10^{38-39.5}$ erg s^{-1}) are consistent with either massive BHs accreting well below their Eddington luminosity (e.g., a $\sim 10^4 M_\odot$ BH with an Eddington ratio of $\sim 10^{-3}$), or stellar-mass BHs (or neutron stars) in XRBs radiating at a significant fraction of their Eddington luminosity. X-ray emission from high-mass XRBs is known to increase as a function of SFR for late-type galaxies (Gilfanov et al., 2004; Grimm et al., 2003; Grimm, H.-J. et al., 2002; Mineo et al., 2012), whereas low-mass XRBs dominate the XRB population in early-type galaxies and scale with stellar mass (Gilfanov, 2004; Humphrey & Buote, 2008; Lehmer et al., 2010, 2014). As our target galaxies are generally late-type (irregular) and have high SFRs relative to their stellar mass (see Section 2), most of the expected X-ray emission will likely be due to high-mass XRBs.

Enhanced X-ray emission relative to the expected contribution from XRBs *could* indicate the presence of a massive BH, however this is neither a necessary nor sufficient condition. For example, a highly sub-Eddington massive BH would likely not contribute significantly to the cumulative X-ray emission, and enhanced X-ray emission can originate from very luminous stellar-mass XRBs (Brorby et al., 2014).

Nevertheless, we estimate the expected cumulative 2-10 keV luminosity from XRBs in each galaxy using the relation in Lehmer et al. (2010) which accounts for high-mass XRBs:

$$L_{\mathrm{HX}} = \begin{cases} 10^{(39.57\pm0.11)}\mathrm{SFR}^{(0.94\pm0.15)} & \mathrm{SFR} \lesssim 0.4 M_\odot \ \mathrm{yr}^{-1} \\ 10^{(39.49\pm0.21)}\mathrm{SFR}^{(0.74\pm0.12)} & \mathrm{SFR} \gtrsim 0.4 M_\odot \ \mathrm{yr}^{-1}. \end{cases} \tag{2.2}$$

We use the SFRs derived in Section 2 (Table 2.5). We note that the uncertainty in the SFRs is ~ 0.13 dex (Hao et al., 2011) and the 1σ scatter in the Lehmer et al. (2010) relationship is ~ 0.4 dex. We find the expected 2-10 keV luminosities from XRB emission to be in the range $\sim 10^{38.2-39.4}$ erg s^{-1} (see Table 2.5).

The observed X-ray luminosities for the galaxies (cumulative from point sources) are

generally within the 1σ scatter of the Lehmer et al. (2010) relationship, with the exception of SBS 0940+544 which has an X-ray luminosity $\sim 3\sigma$ higher than would be expected from star formation (see Figure 2.3; note that II Zw 70 is not plotted as it did not have any observed hard X-ray sources). This discrepancy is unlikely to be due to metallicity, as the metallicities of SBS 0940+544 and Mrk 996 are comparable (at most $\sim$0.2 dex difference, from the NSA values) and Mrk 996 has slightly *lower* X-ray luminosity than expected. However, a combination of stochastic effects (regarding XRB formation in galaxies) and the relatively low SFR of SBS 0940+544 could explain this unexpectedly high X-ray luminosity.

If the X-ray source in SBS 0940+544 were a massive BH, we would expect corresponding radio emission as predicted using the fundamental plane of BH activity from Merloni et al. (2003). The luminosity of X1 in SBS 0940+544 is $L_{2-10\ \mathrm{keV}} \sim 10^{39.2}$ erg s^{-1} (see Table 2.6). Assuming a BH mass of $\log\ (M_{\mathrm{BH}}/M_{\odot}) \sim 3.9 \pm 0.6$ (Reines & Volonteri, 2015), we would expect a radio luminosity of $L_{5\mathrm{GHz}} \sim 10^{33.9}$ erg s^{-1} where the Merloni et al. (2003) relation has a scatter of ~ 0.9 dex. Given that the expected radio emission is within our detection limits, and we do not detect radio emission from this source, we do not consider a massive BH to be a likely explanation.

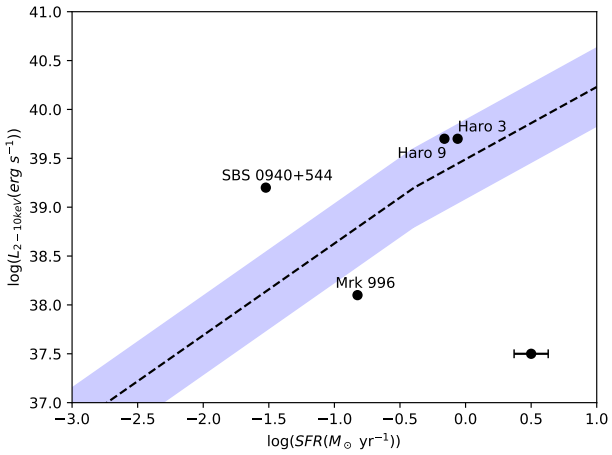


Figure 2.3 X-ray luminosity vs. SFR for the galaxies. The points represent the observed X-ray luminosities (cumulative from the point sources), while the black dashed line and shaded blue area represent the expected X-ray luminosity and the 1σ scatter using the relation from Lehmer et al. (2010). The uncertainty of $\sim$0.13 dex in the SFR is shown in black in the lower right-hand corner. Note that II Zw 70 is absent from this plot as we did not significantly detect any hard X-ray sources.

Table 2.7. Compact Radio Sources

Source ID	R.A. (deg)	Decl. (deg)	P_{5GHz} (μJy/beam)	$P_{7.4GHz}$ (μJy/beam)	F_{5GHz} (μJy)	$F_{7.4GHz}$ (μJy)	log L_{5GHz}	log $L_{7.4GHz}$
(1)	(2)	(3)	(4)	(5)	(6)	(7)	(8)	(9)
II Zw 70−R1	222.735642	35.572258	181	91	360 ± 32	331 ± 33	35.9	36.0
Haro 3−R1	161.344137	55.960794	119	89	93 ± 5	90 ± 5	35.2	35.4
Haro 3−R2	161.343988	55.961128	80	46	77 ± 8	101 ± 12	35.1	35.4
Haro 3−R3a	161.341874	55.961178	725	526	1500 ± 83	1540 ± 86	36.4	36.6
Haro 3−R3b	161.341309	55.960978	664	432	2080 ± 112	2080 ± 113	36.5	36.7
Haro 9−R1	191.321930	27.125492	55	38	24 ± 3	38 ± 3	34.7	35.1
Haro 9−R2	191.321275	27.124692	44	37	45 ± 5	52 ± 10	34.9	35.2
Haro 9−R3	191.320058	27.125258	53	32	39 ± 5	26 ± 4	34.9	34.9
Mrk 996−R1	21.898009	−6.326506	359	230	590 ± 31	549 ± 31	36.2	36.3
SBS 0940+544−R1	146.069071	54.192850	42	24	23 ± 2	19 ± 2	35.0	35.1

Note. — Column 1: radio source identification. Column 2: right ascension. Column 3: declination. Columns 4-5: peak flux values of each source at 5 GHz and 7.4 GHz. Columns 6-7: flux densities (F_ν) at 5 GHz and 7.4 GHz. Columns 8-9: log luminosities (νL_ν) at 5 GHz and 7.4 GHz in units of erg s^{-1}.

Compact Radio Sources

Compact radio emission is detected in all five of our target galaxies (see Figure 2.2). We use the `detect_sources` and `deblend_sources` functions from the Astropy-affiliated Photutils Python package to select our sources. We use multiples of σ, where σ is the RMS noise (see Table 2.4) as thresholds for source detection, adapting the threshold to each image as so to eliminate spurious detections. We then relax these thresholds to measure the flux densities to ensure we capture all the emission from the source.

While the flux densities have an intrinsic $\sim$5% error due to calibration[7], we also introduce uncertainty into our measurements via the exact choice of background we use for each source. To account for this, we take take multiple measurements of each source, varying said background. We report the average flux densities from these measurements, and include both the intrinsic $\sim$5% error and the standard deviation of these measurements in our reported uncertainties.

We identify a total of 10 compact radio sources across the five galaxies, with luminosities in the range $4.8 \times 10^{34} - 5.2 \times 10^{36}$ erg s^{-1}. Due to uncertainties in flux densities and limited frequency coverage, we are not able to reliably determine the spectral indices for most of our sample. Two of the galaxies in our sample have previously detected compact radio sources. Cox et al. (2001) combined 1.4 GHz radio and optical observations to analyze the polar ring of II Zw 71, the companion galaxy to II Zw 70; they also detected the radio source we denote as R1 in this work. Johnson et al. (2004) used 8.3 GHz and 23 GHz radio observations to study the ongoing star formation in Haro 3 and detected the same radio sources presented here.

Comparison to Thermal HII Regions and SNRs While we are primarily interested in detecting potential radio emission from accreting massive BHs, we must also consider

[7] `https://science.nrao.edu/facilities/vla/docs/manuals/oss/performance/fdscale`

alternative origins for the observed compact radio emission since we are dealing with lower luminosities compared to more massive systems. We are mainly concerned about free-free emission from dense HII regions and synchrotron emission from supernova remnants.

We first consider the possibility that the radio emission is entirely thermal and emanating from dense HII regions associated with extragalactic massive star clusters. Under this assumption, we estimate the ionizing flux, Q_{Lyc}, of the radio sources following Condon (1992):

$$\left(\frac{Q_{Lyc}}{\mathrm{s}^{-1}}\right) \gtrsim 6.3 \times 10^{52} \left(\frac{T_e}{10^4\ \mathrm{K}}\right)^{-0.45} \left(\frac{\nu}{\mathrm{GHz}}\right)^{0.1} \times \left(\frac{L_{\nu,\ \mathrm{thermal}}}{10^{27}\ \mathrm{erg\ s^{-1}\ Hz^{-1}}}\right). \quad (2.3)$$

We assume an electron temperature $T_e \sim 10^4$ K for all sources and use the 7.4 GHz luminosities from Table 2.7. Adopting $Q_{\mathrm{Lyc}} = 10^{49}\ \mathrm{s}^{-1}$ as the ionizing flux of a typical O-type main sequence star (O7.5 V star; Vacca et al., 1996), we find ionizing fluxes corresponding to the equivalent of $\sim$ 80 to 5410 O-type stars (median value of 250 O-type stars). The calculated ionizing fluxes are consistent with thermal radio sources associated with young massive star clusters in other star-forming dwarf galaxies (e.g., Aversa et al., 2011; Johnson et al., 2004; Kepley et al., 2014; Reines et al., 2008).

We also calculate the expected galaxy-wide ionizing fluxes using the UV-derived SFRs in Section 2 and Equation 2 in Kennicutt (1998), and compare these values to those from adding up the individual radio sources. We find the two to generally be in agreement, differing by at most a factor of $\sim$2 with the exception of Haro 9. The UV-derived galaxy-wide ionizing flux of Haro 9 is greater by a factor of $\sim$18 compared to the sum of the radio sources. This discrepancy is likely due to the large amount of extended emission in Haro 9 (see Figures 2.2e, 2.2f), which is included in the galaxy-wide UV-derived ionizing flux but excluded when simply adding up the ionizing fluxes of the individual sources.

Next we compare the luminosities of our detected radio sources with known radio SNRs.

We assume a typical SNR spectral index of $\alpha = 0.7$, where $F_\nu \propto \nu^{-\alpha}$, and convert our 7.4 GHz flux densities (Table 2.7) to 1.45 GHz spectral luminosities to compare with the SNR spectral luminosities in Chomiuk & Wilcots (2009).

The corresponding 1.45 GHz spectral luminosities span a range of $\sim 2 \times (10^{25}$-$10^{27})$ erg s^{-1} Hz^{-1}, which are consistent with or slightly above the radio SNRs in Chomiuk & Wilcots (2009) ($L_{1.4\mathrm{GHz}} \sim 10^{23}$ - 10^{27} erg s^{-1} Hz^{-1}). We therefore conclude that the compact radio sources in our sample are not so luminous as to exclude star-formation-related emission in the form of HII regions and/or SNRs.

A Candidate Low-luminosity AGN in Haro 9

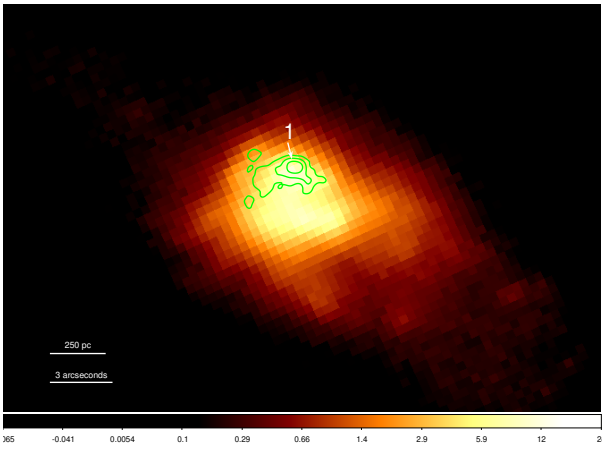
As described above, we have detected 10 hard X-ray point sources and 10 compact radio sources in our sample of five blue compact dwarf galaxies. The luminosities of these sources could be produced by sub-Eddington massive BHs, however the X-ray and radio luminosities alone are also within the expected ranges for stellar processes (see Sections 2, 2). We therefore search for spatially coincident X-ray and radio sources (Figure 2.4), for which the ratio of the luminosities can provide some clues to the origin of the emission.

We find one example of a spatially coincident X-ray and radio source in Haro 9 (X1 and R1 in Figure 2.4c) within the positional uncertainties. The hard X-ray source has a luminosity of log $L_{2-10\mathrm{keV}} = 39.4$ and the compact radio source has a luminosity of log $L_{5\mathrm{GHz}} = 34.7$, where the units are in erg s^{-1}. We make use of the ratio of the radio and X-ray luminosities following Terashima & Wilson (2003),

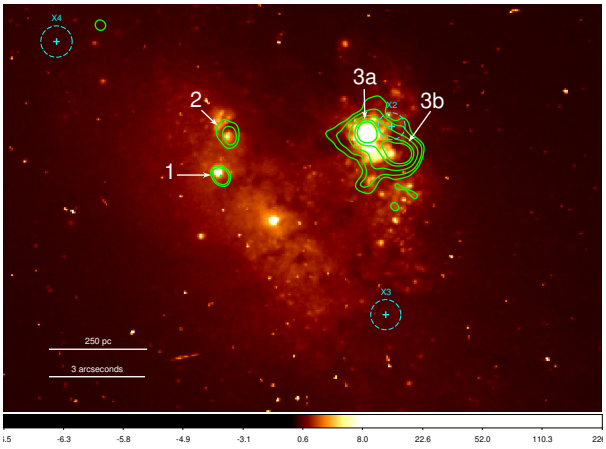
$$R_X = \frac{\nu L_\nu(5\ \mathrm{GHz})}{L_X(2\text{-}10\ \mathrm{keV}),} \tag{2.4}$$

and find that log $R_X \sim -4.7$.

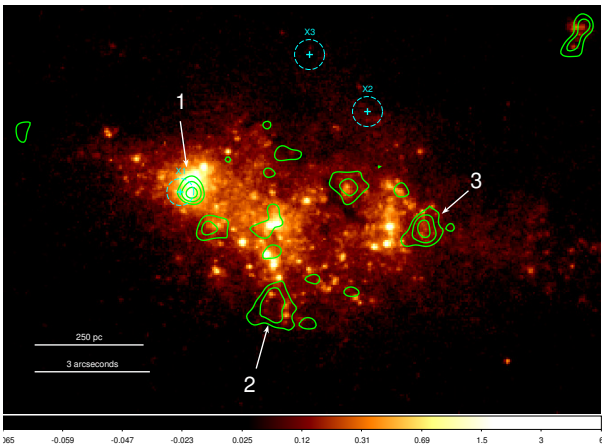
We see that the source is too luminous in the radio to be a stellar-mass XRB (e.g., Gallo et al., 2018), which have log $R_X \lesssim -5.3$. While in principle the radio emission could



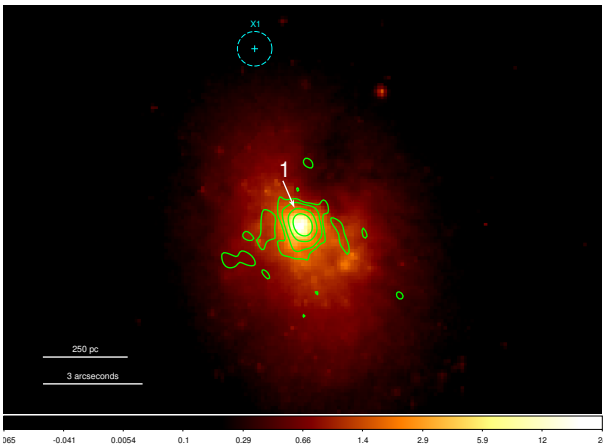
(a) II Zw 70 optical image from the SDSS (g band).



(b) Haro 3 optical image from *HST*/WFPC2 (F606W filter). Note that X-ray sources X1 and X5 are out of view.

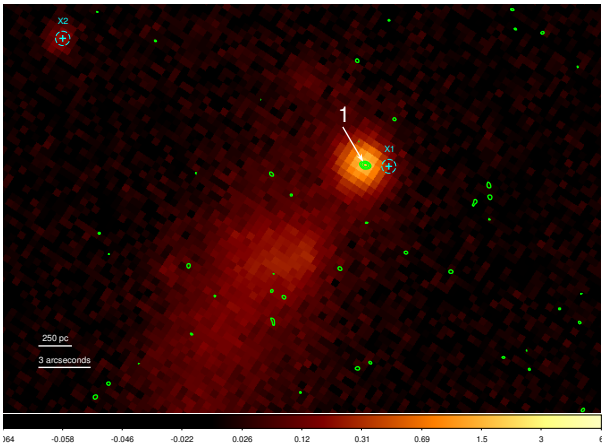


(c) Haro 9 optical image from *HST*/WFPC2 (F439W filter).



(d) Mrk 996 optical image from *HST*/WFPC2 (F569W filter).

Figure 2.4 Optical images from *HST* or the SDSS as indicated, with X-ray sources (cyan) and 5 GHz radio contours (green) overlaid. For the X-ray sources, the cyan crosses and circles mark the position of the source and the 95% positional uncertainty. The only case of spatially coincident X-ray and radio sources within the positional uncertainties is in Haro 9, between X1 and R1.



(e) SBS 0940+544 optical image from the SDSS (g band). Note that X-ray source X2 is likely a background quasar (see Section 2), and thus is excluded from our analysis.

Figure 2.4 Same as above.

be due to a radio flare associated with an XRB state transition, with a radio luminosity of log $L_{5\mathrm{GHz}} \sim 34.7$ the source would be brighter than the brightest flare we have seen from an XRB in our own galaxy (Cyg X-3, log $L_{15\mathrm{GHz}} \sim 34.3$; Corbel et al., 2012). Additionally, the likelihood of catching a state transition is rare, especially with both the radio and X-ray emission so bright, given that the observations were taken ∼3 weeks apart (state transitions usually last from a few days to a few weeks; Yu & Yan, 2009). As such, the source is unlikely to be a stellar-mass XRB, even one undergoing a state transition.

The X-ray/radio source is also not likely to be a SNR, since these objects are typically much more luminous in the radio with log $R_X > -2.7$ (see Supplementary Information in Reines et al., 2011, and references therein).

A more reasonable possibility is an ultra-luminous X-ray source (ULX) bubble. This would account for the X-ray luminosity, and the observed radio luminosity does not exceed values for ULX bubbles found in the literature (e.g. Cseh et al., 2012; Motch et al., 2010,

with log $L_{\rm R} \sim 35.3$). While many ULX bubbles are extended, measuring hundreds of pc across in the optical (Pakull & Mirioni, 2002, 2003), bubbles as small as ∼40 pc have been observed in the radio (Lang et al., 2007), which is consistent with the VLA resolution of our observed point-like source. Thus, if the source is a ULX bubble, it would have to be a luminous and relatively compact one.

The source is also consistent with a low-luminosity AGN. From Figure 3 in Merloni et al. (2003), we see that the source falls within the range of massive black holes in the compact radio luminosity versus hard X-ray luminosity plane. Under the assumption that the source is indeed an accreting massive BH, the fundamental plane of BH activity relating BH mass to radio and X-ray luminosity implies a BH mass of log $(M_{\rm BH}/M_{\odot}) \sim 4.8 \pm 1.1$ using the Merloni et al. (2003) relation and log $(M_{\rm BH}/M_{\odot}) \sim 5.2 \pm 0.44$ using the Miller-Jones et al. (2012) relation. Using the scaling between BH mass and host galaxy total stellar mass ($\sim 10^{8.93}\ M_{\odot}$ for Haro 9; see Table 2.1) for local AGNs from Reines & Volonteri (2015) provides a BH mass of log $(M_{\rm BH}/M_{\odot}) \sim 5.3 \pm 0.55$. If the source is indeed a massive black hole, it must be accreting at a modest rate given the low X-ray luminosity. Assuming a black hole mass of $M_{\rm BH} \sim 10^5\ M_{\odot}$ and an X-ray bolometric correction of 20 (Vasudevan & Fabian, 2009), the corresponding Eddington fraction would be ∼0.4%.

We note that the ratios and comparisons discussed above are only valid if the X-ray and radio emission are indeed coming from the same source. The positional offset between X1 and R1 in Haro 9 is $0\farcs3$. While this is within the positional uncertainties, we cannot definitively say the X-ray and radio emission come from the same object. Moreover, there is a star cluster complex in the same region as the X-ray/radio source(s) that could plausibly host both an XRB and SNR (or HII region). Therefore, we caution that this apparently coincident X-ray/radio source in Haro 9 should be considered a *candidate* low-luminosity AGN.

Detection Limits

AGNs in dwarf galaxies are powered by less massive BHs than typical AGNs in more massive galaxies (e.g., Reines & Volonteri, 2015), and will therefore be less luminous. As an example, the Eddington luminosity of a $10^4 M_\odot$ BH is only $\sim 10^{42}$ erg s^{-1}. However, we know that BHs with high accretion rates are rare (e.g., Schulze, A. & Wisotzki, L., 2010) so the actual luminosities of AGNs in dwarf galaxies may be orders of magnitude lower. Therefore, we must lower our luminosity threshold for what *could* be an AGN in dwarf galaxy, which we have explored in the preceding sections. We also require sensitive, high-resolution observations in order to probe lower luminosities and isolate compact X-ray/radio emission from that of the host galaxy on larger scales.

Here we estimate detection limits of potential massive BHs in our sample of BCDs. We first estimate the expected BH masses based on the scaling relation between BH mass and host galaxy total stellar mass for local AGNs in Reines & Volonteri (2015). Given the stellar masses in Table 2.1, we expect BH masses in the range $\log (M_{\rm BH}/M_\odot) \sim 3.9 - 5.3$, with a median of $\log (M_{\rm BH}/M_\odot) \sim 4.6$. The scatter in the Reines & Volonteri (2015) relation is ~ 0.55 dex. Next we use our X-ray detection limits to determine the minimum detectable Eddington fractions of BHs with these masses. The Eddington fraction is given by

$$f_{\rm Edd} = (\kappa L_X)/(L_{\rm Edd}) \tag{2.5}$$

where κ is the 2-10 keV bolometric correction and L_X, $L_{\rm Edd}$ are the X-ray and Eddington luminosity of the BH, respectively. We find $L_{\rm Edd}$ from the BH masses via

$$L_{\rm Edd} \approx 1.26 \times 10^{38}\ M_{\rm BH}/M_\odot \text{ erg s}^{-1} \tag{2.6}$$

and take $L_X \sim 10^{38}$ erg s^{-1}, which is the minimum detectable X-ray luminosity corresponding

to our X-ray flux sensitivity of $F_X \sim 2.5 \times 10^{-15}$ erg s^{-1} cm^{-2} (see Section 2) at the distances of our galaxies ($\sim$ 20 Mpc). We assume these BHs are accreting at low rates ($f_{\rm Edd} \lesssim 0.1$) giving $\kappa \sim 15 - 30$ (Vasudevan & Fabian, 2009). Adopting $\kappa \sim 30$ (for an upper bound) and $M_{\rm BH} \sim 10^4$ $M_\odot$, we find log $f_{\rm Edd} \sim -2.8$. In other words, our X-ray observations are sensitive enough to detect a $\sim 10^4$ $M_\odot$ BH radiating at $\sim 0.1\%$ of its Eddington luminosity. The corresponding radio luminosity predicted from the fundamental plane of BH activity (Merloni et al., 2003) is $\sim 10^{33}$ erg s^{-1}, albeit with large uncertainty – the 1σ scatter in the relation is ~ 0.9 dex. Our VLA observations are sensitive to radio luminosities of $\sim$ a few $\times 10^{34}$ erg s^{-1}, making this right on the edge of what we could detect (including the ~ 0.9 dex uncertainty).

Summary and Conclusions

We have presented high-resolution *Chandra* and VLA observations of five low-mass blue compact dwarf galaxies in a search for X-ray and radio signatures of accreting massive BHs. We detected 10 hard X-ray point sources and 10 compact radio sources in our sample, which in all but one case did not overlap. While we were primarily interested in detecting signatures of massive BHs, we considered possible alternative origins for the observed radio and X-ray emission such as thermal HII regions, SNRs, and XRBs. None of the X-ray and radio sources alone were so luminous as to rule out star-formation-related emission.

In the BCD Haro 9, however, we detected a spatially coincident X-ray and radio source (within the astrometric uncertainties) that was consistent with an active massive BH ($M_{\rm BH} \sim 10^5$ $M_\odot$) under the assumption that the X-ray and radio emission originated from the same source. We cautioned that the combination of a stellar-mass X-ray binary plus a supernova remnant (or HII region) could also account for the X-ray and radio sources, respectively, which are located in the vicinity of a star cluster complex.

Compared to other dwarf galaxies found to host active massive BHs (e.g., Reines et al.,

2013, 2014, 2011), our sample of BCDs have lower stellar masses ($\sim 3\times$ on average). Moreover, in contrast to optically-selected samples (e.g., Reines et al., 2013), the BCDs studied here are actively star-forming with somewhat disturbed morphologies. The lack of convincing detections of massive BHs in our sample of BCDs could be suggestive of the BH occupation fraction dropping off with decreasing galaxy mass, or that BHs in BCDs are not commonly accreting at a detectable rate. Indeed, recent simulations indicate that BH growth in low-mass galaxies can be stunted by supernova feedback (e.g., Anglés-Alcázar et al., 2017; Habouzit et al., 2017) and that the conditions for rapid BH accretion in dwarf galaxies are rare (Bellovary et al., 2019).

While this work has broadened the parameter space in the search for massive BHs in dwarf galaxies, future studies with larger sample sizes are necessary to more accurately determine the prevalence of massive BHs in low-mass star-forming dwarfs such as BCDs and help shed light on the origin of BH seeds (e.g., Plotkin & Reines, 2018).

We thank the referee for their comments and gratefully acknowledge helpful conversations with Gregory Sivakoff and Kelsey Johnson during the early stages of this project. Support for this work was provided by NASA through *Chandra* Award Number GO2-13126 issued by the *Chandra X-ray Observatory Center*, which is operated by the Smithsonian Astrophysical Observatory for and on behalf of the NASA under contract NAS8-03060. TDR acknowledges support from the Netherlands Organisation for Scientific Research (NWO) Veni Fellowship. The National Radio Astronomy Observatory is a facility of the National Science Foundation operated under cooperative agreement by Associated Universities, Inc. The scientific results reported in this article are based in part on observations made by the *Chandra X-ray Observatory*. They are also based on observations made with the NASA/ESA Hubble Space Telescope, and obtained from the Hubble Legacy Archive, which is a collaboration between the Space Telescope Science Institute (STScI/NASA), the European Space Agency (ST-ECF/ESAC/ESA) and the Canadian Astronomy Data Centre (CADC/NRC/CSA). Funding for the Sloan Digital Sky Survey IV has been provided by the Alfred P. Sloan Foundation, the U.S. Department of Energy Office of Science, and the Participating Institutions. SDSS acknowledges support and resources from the Center for High-Performance Computing at the University of Utah. The SDSS web site is www.sdss.org. This publication makes use of data products from the Wide-field Infrared Survey Explorer, which is a joint project of the University of California, Los Angeles, and the Jet Propulsion Laboratory/California Institute of Technology, funded by the National Aeronautics and Space Administration. This work has also used observations made with the NASA Galaxy Evolution Explorer. GALEX is operated for NASA by the California Institute of Technology under NASA contract NAS5-98034. Funding for the NASA-Sloan Atlas has been provided by the NASA Astrophysics Data Analysis Program (08-ADP08-0072) and the NSF (AST-1211644).

A *CHANDRA* AND *HST* VIEW OF *WISE*-SELECTED AGN CANDIDATES IN DWARF GALAXIES

Contribution of Authors and Co-Authors

Manuscript in Chapter 3

Author: Lilikoi J. Latimer

Contributions: Reduced and analyzed X-ray data, wrote initial draft of the manuscript.

Author: Amy E. Reines

Contributions: Advised, helped edit the manuscript, provided scientific and editorial comments on the manuscript.

Author: Kevin N. Hainline

Contributions: Provided scientific and editorial comments on the manuscript.

Author: Jenny E. Greene

Contributions: Provided scientific and editorial comments on the manuscript.

Author: Daniel Stern

Contributions: Provided scientific and editorial comments on the manuscript.

Manuscript Information

Lilikoi J. Latimer, Amy E. Reines, Kevin N. Hainline, Jenny E. Greene, Daniel Stern

The Astrophysical Journal

Status of Manuscript:
____ Prepared for submission to a peer-reviewed journal
____ Officially submitted to a peer-reviewed journal
____ Accepted by a peer-reviewed journal
_X_ Published in a peer-reviewed journal

IOP Publishing
The Astrophysical Journal, Volume 914, Number 2
10.3847/1538-4357/abfe0c

Introduction

The vast majority of massive galaxies play host to supermassive black holes (BHs) at their cores. However, we do not know how these monster BHs came to be. Ideally, we would directly observe galaxies in the early Universe and the "seed" BHs they harbor, but these BHs currently remain out of observational reach. They are simply too distant and faint to detect with existing facilities (e.g., Vito et al., 2018; Volonteri & Reines, 2016). Instead, we turn to nearby dwarf galaxies. These galaxies are relatively low mass ($M_\star \lesssim 10^{9.5}\ M_\odot$) and may host BHs of similar mass to those in early-universe galaxies (for reviews, see Greene et al., 2020; Mezcua, 2017; Reines & Comastri, 2016). We can use the occupation fraction of massive BHs in these proxy galaxies as well as scaling relations at low mass to help distinguish between different theories concerning the formation of seed BHs such as remnants from Pop III stars, stellar mergers in compact star clusters, or direct collapse of protogalactic gas (Greene, 2012; Ricarte & Natarajan, 2018; van Wassenhove et al., 2010; Volonteri, 2010).

There is now growing evidence for the existence of BHs in dwarf galaxies, with detailed studies of single galaxies to large-scale surveys (e.g. Baldassare et al., 2018; Baldassare et al., 2020, 2015, 2017, 2016; Birchall et al., 2020; Dickey et al., 2019; Hainline et al., 2016; Latimer et al., 2019; Lemons et al., 2015; Lupi et al., 2020; Mezcua et al., 2018; Mezcua & Sánchez, 2020; Mezcua et al., 2019; Moran et al., 2014; Nguyen et al., 2019; Pardo et al., 2016; Reines et al., 2020, 2013, 2014, 2011; Schramm et al., 2013; Schutte et al., 2019). Multiple studies have tried to make progress identifying massive BHs in the mid-infrared (mid-IR) using data from the *Wide-field Infrared Survey Explorer* (*WISE*) (Wright et al., 2010) by extrapolating active galactic nuclei (AGN) diagnostics (e.g. Jarrett et al., 2011; Stern et al., 2012) to low-mass galaxies (Marleau et al., 2017; Sartori et al., 2015; Satyapal et al., 2014). These studies find that the IR-selected AGN fraction seems to increase at low galaxy masses, a puzzling conclusion that contradicts studies at other wavelengths. Motivated by these results, as well

as earlier work (e.g., with *WISE*) that revealed extreme star-forming dwarf galaxies could produce very red mid-IR colors (Griffith et al., 2011; Hirashita & Hunt, 2004; Izotov et al., 2011, 2014; O'Connor et al., 2016; Reines et al., 2008; Rémy-Ruyer et al., 2015), Hainline et al. (2016) revisited mid-IR AGN selection techniques applied to dwarf galaxies.

Table 3.1. Sample of Dwarf Galaxies with Mid-IR Selected Candidate AGNs

ID	BPT Class.	NSAID	RGG ID	SDSS Name	$N_{\rm H}$ (10^{20} cm^{-2})	z	r_{50} (kpc)	M_g (mag)	$g-r$ (mag)	log $M_\star/M_\odot$
(1)	(2)	(3)	(4)	(5)	(6)	(7)	(8)	(9)	(10)	(11)
1	AGN	68765	3	J032224.64+401119.8	13.60	0.02679	1.0	−18.7	0.467	9.4
2	AGN	10779	9	J090613.75+561015.5	2.83	0.04697	1.7	−19.0	0.400	9.4
3	AGN	125318	11	J095418.15+471725.1	1.03	0.03284	2.0	−18.7	0.438	9.1
4	AGN	113566	18	J114359.58+244251.7	2.09	0.04992	1.3	−18.7	0.647	9.5
5	AGN	104527	24	J133245.62+263449.3	0.99	0.04693	1.2	−19.1	0.272	9.4
6	Comp.	79874	119	J152637.36+065941.6	3.47	0.03829	0.8	−18.7	0.248	9.3
7	SF	6205	···	J005904.10+010004.2	3.06	0.01743	0.9	−18.3	0.211	8.7
8	SF	98135	···	J154748.99+220303.2	4.64	0.03154	0.7	−18.1	−0.459	8.2
9	SF	57649	···	J160135.95+311353.7	2.72	0.03085	1.3	−18.1	0.109	8.6
10	SF	4610	···	J173501.25+570308.8	3.44	0.04797	0.9	−20.5	−1.050	8.8
11	SF	151888	···	J233244.60−005847.9	4.00	0.02437	1.3	−18.9	0.344	9.3

Note. — Column 1: Identification number used in this paper. Column 2: Classification of the galaxy as AGN, composite (Comp.) or star-forming (SF) from the N II/Hα BPT diagram (left panel in Figure 3.2) Column 3: Identification number in the NSA. Column 4: Identification number assigned by Reines et al. (2013) Column 5: SDSS name. Column 6: Galactic neutral hydrogen column density (Dickey & Lockman, 1990)[1]. Column 7: redshift, specifically the `zdist` parameter from the NSA. Column 8: Petrosian 50% light radius. Column 9: absolute g-band magnitude corrected for foreground Galactic extinction. Column 10: $g-r$ color. Column 11: log galaxy stellar mass. The values given in columns 7-11 are from the NSA and we assume $h = 0.73$. IDs 2, 3, and 6 were confirmed as broad-line AGNs by Baldassare et al. (2017)

Hainline et al. (2016) find that dwarf galaxies with the reddest mid-IR colors have the youngest stellar populations and highest star formation rates, demonstrating that dwarf galaxies can heat dust in a way that can mimic luminous AGNs. In particular, they show that using a single $W1 - W2$ color cut to select candidate AGNs leads to severe contamination from dwarf starburst galaxies. While this mid-IR color selection often fails for the dwarf population, it appears to be quite robust for more luminous galaxies (Stern et al., 2012). From Hainline et al. (2016), it was not clear whether employing the two-color AGN selection of Jarrett et al. (2011) would suffer from contamination as well. They therefore presented a sample of candidate AGNs in dwarf galaxies falling within the color-color AGN selection box of Jarrett et al. (2011) rather than employing a single color cut (Stern et al., 2012). Overall, their results are more in line with findings at optical wavelengths; that is, no enhanced active fraction at low galaxy masses is seen. A subsequent theoretical investigation by Satyapal et al. (2018) also showed that some extreme starbursts with high ionization parameters or gas densities could mimic AGNs in mid-IR color space.

In this paper, we observationally probe the efficacy of the mid-IR *WISE* color-color selection box of Jarrett et al. (2011) in dwarf galaxies using high resolution X-ray and optical/near-IR (NIR) observations with *Chandra* and *HST*. Specifically, we seek to understand whether this AGN selection technique can effectively distinguish between BH activity and star formation when applied to low-mass galaxies.

Sample Selection

The dwarf galaxies studied here come from the sample of Hainline et al. (2016) that have mid-IR colors suggestive of AGNs. Hainline et al. (2016) start with a sample of $\sim$18,000 dwarf galaxies ($M_* \lesssim 3 \times 10^9\ M_\odot$) in the NASA-Sloan Atlas (v0_1_2)[2] with significant

[2] http://nsatlas.org/

detections in the first three bands of the ALLWISE data release (see Section 2 in Hainline et al., 2016). From this, they identify 41 galaxies with $W1 - W2$ vs. $W2 - W3$ colors that fall within the Jarrett et al. (2011) *WISE* AGN selection box. Eleven of these galaxies have optical emission-line measurements (both redshifts and fluxes) and signal-to-noise ratios >5 in all four *WISE* bands. We obtained new *Chandra X-ray Observatory* and *Hubble Space Telescope* (*HST*) observations for seven of these dwarf galaxies (Proposal ID: 20700286; PI: Reines) and archival *Chandra* and *HST* observations for three additional galaxies (Proposal ID: 16700103; PI: Reines); the latter are broad-line AGNs/Composites from the Reines et al. (2013) sample and the *Chandra* X-ray + *HST* ultraviolet (UV; $\sim$ 2700 Å) observations have previously been presented by Baldassare et al. (2017). The final galaxy had an archival *Chandra* observation, but not *HST* imaging.

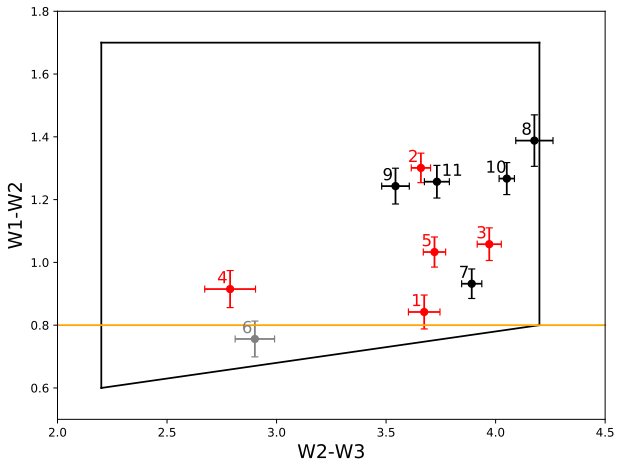


Figure 3.1 *WISE* color-color diagram for the dwarf galaxies in our sample. The galaxies classified as AGN, composite, and star-forming are in red, grey, and black, respectively, using the [N II]/Hα BPT diagram (left panel in Figure 3.2). In black, we plot the AGN selection box from Jarrett et al. (2011), and in orange we show the W1-W2 > 0.8 selection criterion from Stern et al. (2012).

Table 3.2. *WISE* magnitudes

ID	W1 (mag)	W2 (mag)	W3 (mag)	W1-W2 (mag)	W2-W3 (mag)
(1)	(2)	(3)	(4)	(5)	(6)
1	14.01	13.17	9.50	0.84	3.67
2	13.40	12.10	8.44	1.30	3.66
3	13.86	12.80	8.83	1.06	3.97
4	14.28	13.36	10.57	0.92	2.79
5	13.51	12.48	8.76	1.03	3.72
6	14.12	13.37	10.46	0.76	2.90
7	13.31	12.38	8.49	0.93	3.89
8	15.58	14.20	10.02	1.39	4.18
9	14.53	13.28	9.74	1.24	3.54
10	13.04	11.77	7.72	1.27	4.05
11	13.76	12.50	8.77	1.26	3.73

Properties of the eleven dwarf galaxies in our sample are summarized in Table 3.1, and we plot our galaxies on the *WISE* color-color diagram in Figure 3.1 (see Table 3.2 for magnitudes). Five of our galaxies are classified as AGNs, one as Composite, and five as star-forming using the [N II]/Hα BPT diagram (left panel in Figure 3.2). The line fluxes used for the ratios in Figure 3.2 are measured from Sloan Digital Sky Survey (SDSS) spectra, as described in Reines et al. (2013). Three-color *HST* images of our galaxies are shown in Figure 3.3, except in the case of ID 10 for which we use Dark Energy Camera Legacy Survey (DECaLS) imaging.

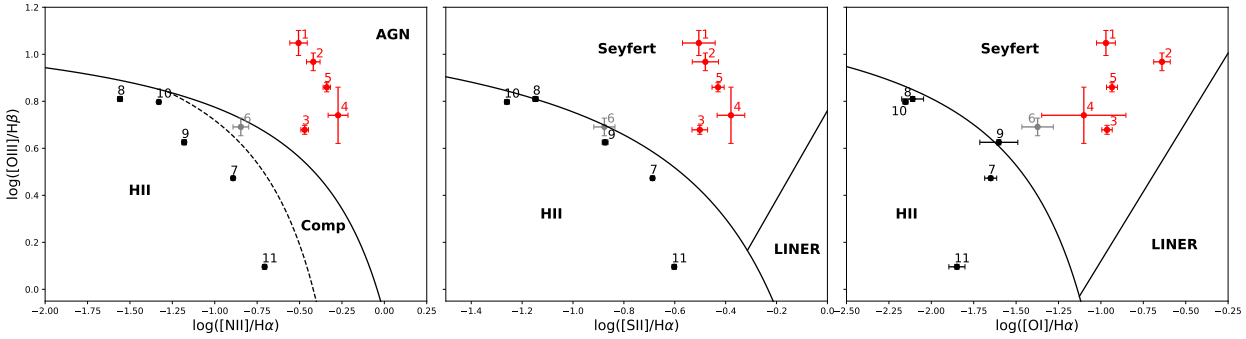


Figure 3.2 Optical narrow emission line diagnostic diagrams for our galaxies. Regions are separated according to the classification scheme in Kewley et al. (2006). The galaxies falling in the AGN, composite, and star-forming regions in the leftmost diagram are in red, grey, and black, respectively.

Observations and Data Reduction

Chandra X-ray Observatory

X-ray observations of our target galaxies were taken with *Chandra* between 2014 Jan 07 and 2020 Jan 03, with exposure times ranging between 8.0 and 24.4 ks. A summary of the *Chandra* observations is given in Table 3.3. In each observation, the target galaxy was placed at the center of the ACIS S3 chip. We used the `CIAO` software v4.11 (Fruscione et al., 2006) to reprocess the data and apply calibration files (CALDB 4.8.4.1), creating new level 2 event files.

We next corrected the *Chandra* astrometry by matching to SDSS catalog sources (DR12). We created a list of X-ray point sources by using the `CIAO` function `wavdetect`, a point source detection algorithm, on the S3 chip of the *Chandra* image filtered from 0.5-7 keV. We excluded any `wavdetect` sources falling within $3r_{50}$ of the galaxy, and used the `CIAO` function `wcs_match` to match the remaining sources to optical point sources in the SDSS DR12 catalog with i-band magnitudes < 22. We found between zero and five matching

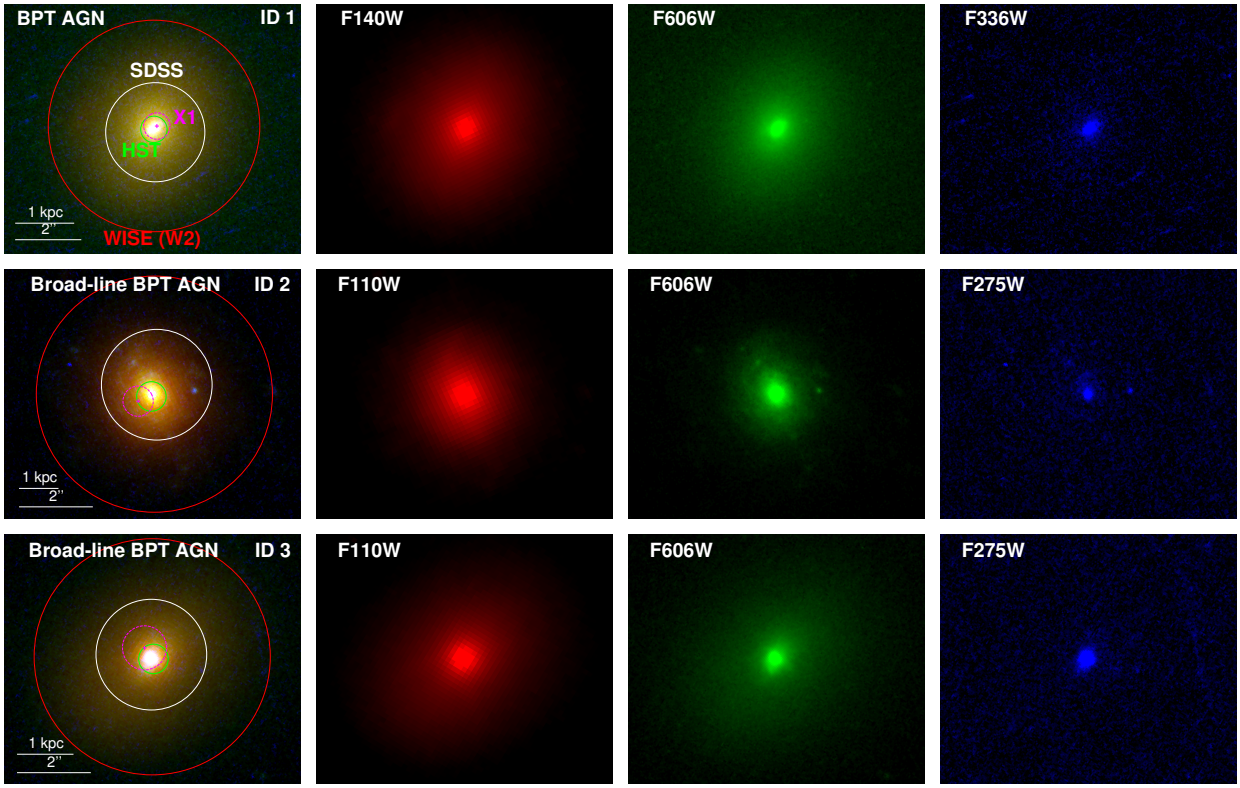


Figure 3.3 Three-color *HST* images of our galaxies. Red shows the NIR image (F140W for IDs 1,4-5,7-9,11, F110W for IDs 2-3,6), green shows the optical band (F606W), and blue shows the U/UV band (F336W for IDs 1,4-5,7-9,11, F275W for IDs 2-3,6). We overlay green circles of radii 0.″4 at the peak of the NIR emission in the *HST* images, as well as the positions and 95% positional uncertainties of the detected X-ray sources in magenta. The SDSS 3″ spectroscopic apertures are shown as white circles and the resolution of the *WISE* W2-band (6.4″) is in red. The text in the upper left corner denotes the BPT classification of the galaxy. Note that for ID 10, *HST* imaging was unavailable, so DECaLS imaging was used instead, with red, green, and blue as the z, r, and g bands, respectively.

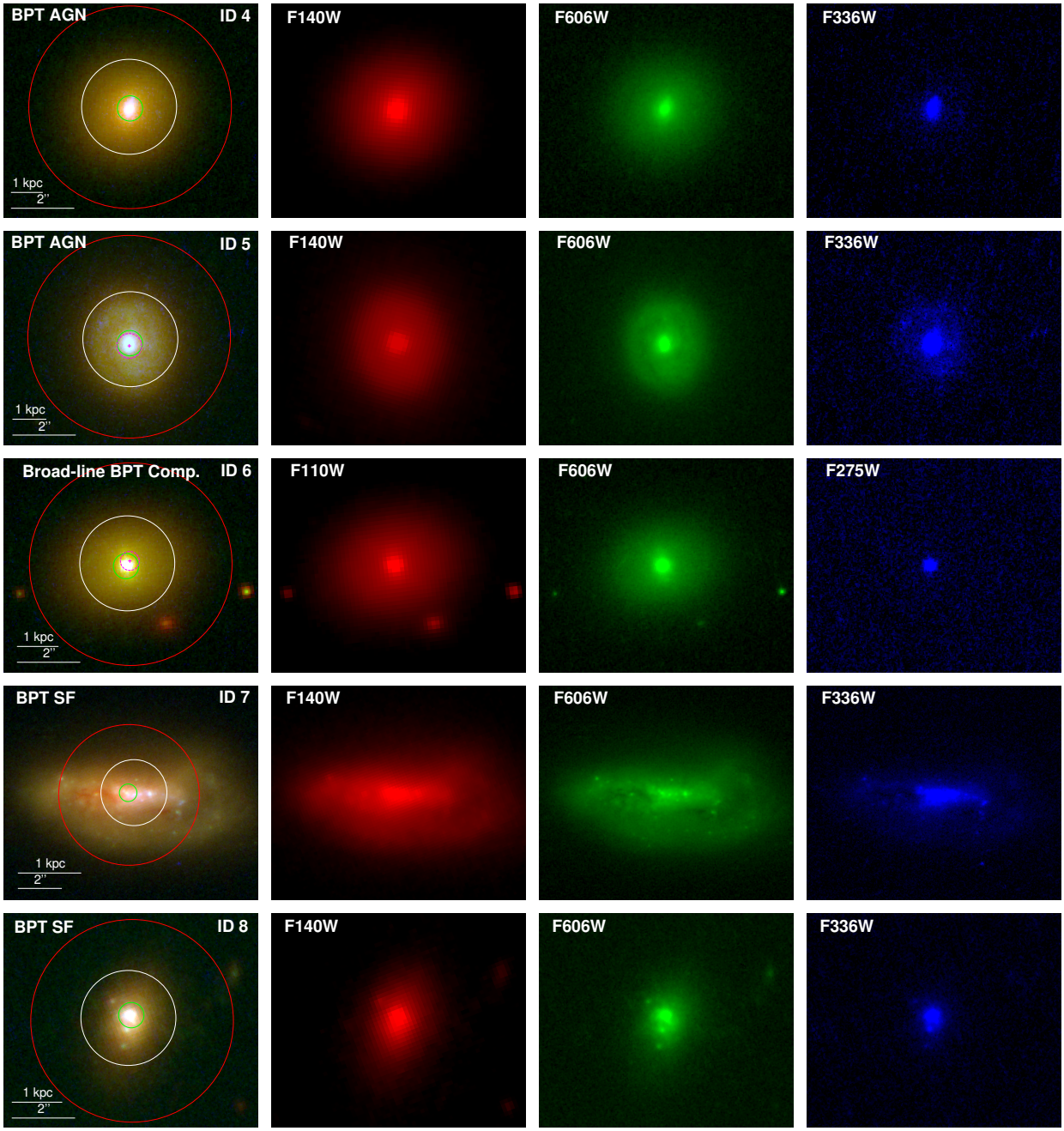


Figure 3.3 Same as above.

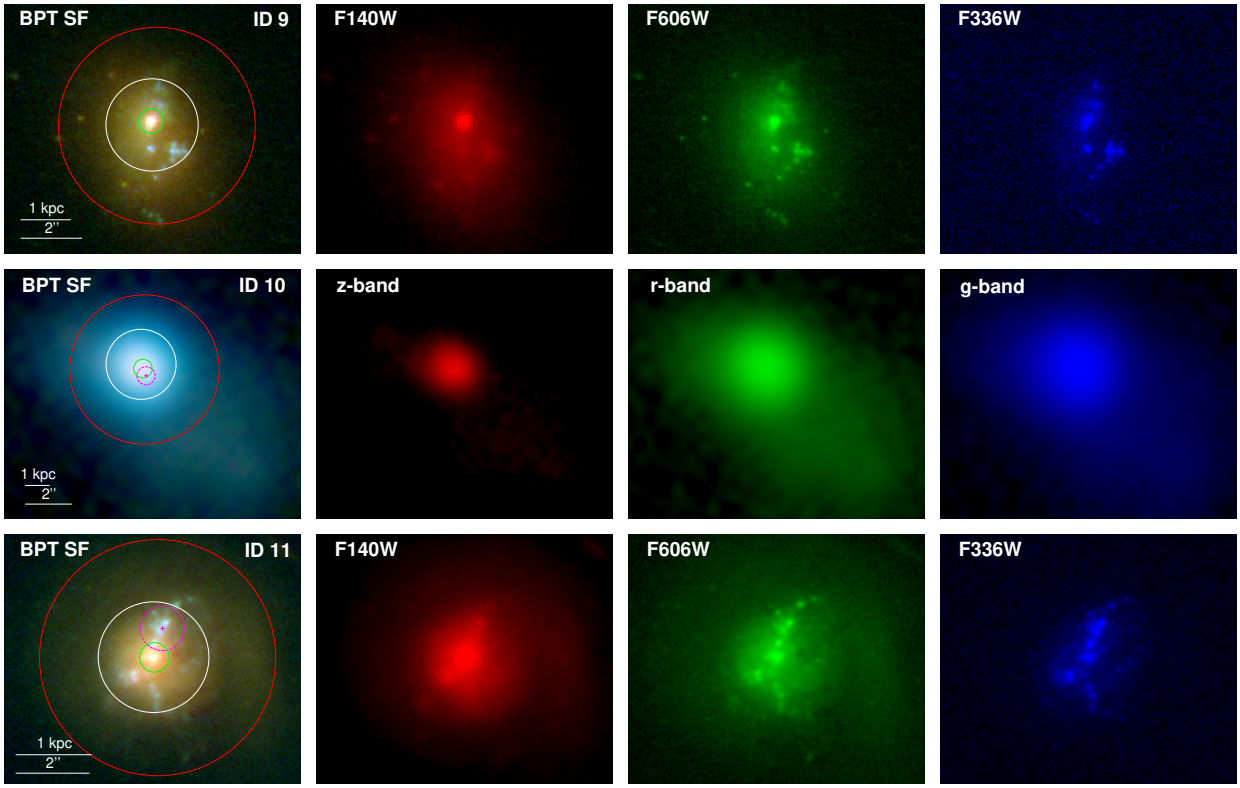


Figure 3.3 Same as above.

Table 3.3. *Chandra* Observations

ID	Date observed	Obs ID	Exp. time (ks)	$N_{\rm background}$
1	2019 Mar 26	21446	14.9	0.0070
2	2014 Dec 26	17033	15.8	0.0073
3	2016 Apr 06	17034	8.0	0.0112
4	2019 Mar 10	21447	24.4	0.0057
5	2019 Aug 03	21448	21.8	0.0047
6	2015 Feb 10	17037	10.9	0.0019
7	2019 Sep 20	21449	9.9	0.0085
8	2020 Jan 03	21450	20.8	0.0036
9	2019 Dec 07	21451	19.8	0.0117
10	2014 Jan 07	14908	10.3	0.0015
11	2019 May 08	21452	12.9	0.0144

Note. — $N_{\rm background}$ is the number of expected 2-10 keV $N(>S)$ background sources within $3r_{50}$, using Moretti et al. (2003).

`wavdetect` and SDSS sources on the S3 chip for each observation. We only updated the astrometry if we found at least 1 match, and given the small number of matches, only applied a translation correction. This resulted in updated astrometry for six of the eleven galaxies (IDs 1, 2, 5-6, 8-9), with astrometric shifts ranging between ±0.02-1.53 pixels (0.″01-0.″75).

Optical/NIR Images

HST/WFC3 images spanning ultraviolet to NIR wavelengths were taken between 2016 Feb 18 and 2019 Nov 02. The new data (galaxy IDs 1, 4-5, 7-9, and 11; Proposal 15607,

PI: Reines) were taken in the F336W ($\sim U$-band), F606W ($\sim$ wide V-band), and F140W ($\sim H$-band) filters. The archival data (galaxy IDs 2-3 and 6; Proposal 13943, PI: Reines) were taken in the F275W (near-UV), F606W, and F110W ($\sim$ wide YJ-band) filters.

Each galaxy was allocated one orbit, with exposure times of $\sim$7-9 minutes in the NIR, $\sim$11-12 minutes in the V-band and $\sim$12-15 minutes in the short wavelength filters. The images were processed using the AstroDrizzle routine in the standard *HST* pipeline. We adjust the astrometry of the *HST* images to match that of the SDSS by comparing common sources between the two, resulting in astrometric shifts up to $0\farcs52$, with a median shift of $0\farcs22$. As galaxy ID 10 had no *HST* imaging observations, we retrieved images from DECaLS in the g, r, and z bands for use in Figure 3.3.

Table 3.4. X-ray Sources

ID	R.A.	Decl.	Net Counts		Flux (10^{-15} erg s^{-1} cm^{-2})		Luminosity (log(erg s^{-1}))	
	(deg)	(deg)	0.5-2 keV	2-7 keV	0.5-2 keV	2-10 keV	0.5-2 keV	2-10 keV
(1)	(2)	(3)	(4)	(5)	(6)	(7)	(8)	(9)
1	50.602662	40.188872	$6.04^{+5.07}_{-3.46}$	$10.58^{+7.58}_{-4.98}$	4.15	16.21	39.8	40.4
2	136.557572	56.170866	$14.66^{+8.30}_{-5.83}$	$2.02^{+3.62}_{-1.86}$	5.51	2.79	40.4	40.1
3	148.575716	47.290371	$2.07^{+3.66}_{-1.76}$	$2.11^{+3.74}_{-1.83}$	1.69	5.76	39.6	40.1
4	···	···	···	···	<0.74	<2.03	<39.6	<40.0
5	203.190100	26.580321	16.82±7.67	$4.09^{+4.48}_{-3.11}$	6.60	4.18	40.5	40.3
6	231.655677	6.994941	484.37±37.9	127.75±20.24	271.89	255.72	41.9	41.9
7	···	···	···	···	<1.99	<5.22	<39.1	<39.5
8	···	···	···	···	<0.96	<2.42	<39.3	<39.7
9	···	···	···	···	<0.94	<2.49	<39.3	<39.7
10	263.755101	57.052294	$13.36^{+7.94}_{-5.50}$	$6.48^{+5.44}_{-3.70}$	6.73	13.58	40.5	40.8
11	353.187593	−0.979194	···	$3.12^{+4.16}_{-2.48}$	<1.43	5.40	<39.2	39.8

Note. — Column 1: galaxy ID. Column 2: right ascension of X-ray source. Column 3: declination of X-ray source. Columns 4-5: net counts after applying a 90% aperture correction. Error bars represent 90% confidence intervals. Columns 6-7: fluxes corrected for Galactic absorption. Columns 8-9: log luminosities corrected for Galactic absorption; calculated using a photon index of $\Gamma = 1.8$. IDs 4, 7-9, 11 had no detected soft and/or hard band X-ray sources. The reported fluxes and luminosities are upper limits (see Section 3).

Analysis and Results

X-ray Sources

Using high-resolution X-ray observations from *Chandra*, we search for X-ray point sources that could indicate the presence of accreting massive BHs in our target dwarf galaxies. We first check our *Chandra* images for background flares, removing time intervals where the background rate was $> 3\sigma$. We then re-run `wavdetect` on images of the S3 chip filtered from 0.5-7 keV. We use wavelet scales of 1.0, 1.4, 2.0, 2.8, and 4.0, with a point spread function map of 39% enclosed energy fraction at 2.3 keV (for hard band; 2-7 keV) and 1.56 keV (for soft band; 0.5-2 keV). We set a significance threshold of 10^{-6}, at which we expect approximately one false source detection over the entire S3 chip. We then restrict further analysis to the `wavdetect` sources that lie within $3r_{50}$ of the galaxy to exclude any X-ray sources not associated with the target.

We find source counts using circular apertures corresponding to the 90% enclosed energy fraction at 4.5 keV ($\sim 2''$ for our sources). We estimate background counts per pixel using circular annuli centered on the source with an inner radius equal to the source aperture radius and an outer radius of 12 $\times$ the inner radius. We consider a source to be detected if the source counts are above the background counts in the source aperture to within a 95% confidence level using the Bayesian methods in Kraft et al. (1991) for Poisson-distributed data with low source counts. All detected sources pass this test.

After subtracting off the background counts in the source aperture from the source counts, we apply a 90% aperture correction to arrive at the net counts for each source. We detect a total of seven X-ray point sources across eleven galaxies, and report their properties in Table 3.4. Note that galaxy IDs 2-3 and 6 were analyzed in Baldassare et al. (2017), and we find the same sources with similar luminosities.

We estimate 95% positional uncertainties using the empirical formula from Hong et al.

(2005) involving the `wavdetect` counts and off-axis position of the sources. The error bars on the net counts represent 90% confidence intervals. If the source counts are < 10, we take the background counts into account and follow the formalism of Kraft et al. (1991). If the source counts are ≥ 10 we use the confidence intervals from Gehrels (1986), which assume that the background counts are negligible.

We calculate unabsorbed hard (2-10 keV) and soft (0.5-2 keV) X-ray fluxes using the `CIAO` function `srcflux`. We use a power-law spectral model with photon index $\Gamma = 1.8$, which is typical for low-luminosity AGN (Ho, 2008, 2009) and ultraluminous X-ray sources at these energies (Swartz et al., 2008), and Galactic column densities from the Dickey & Lockman (1990) maps. The unabsorbed fluxes and corresponding luminosities are summarized in Table 3.4. We ignore any potential absorption intrinsic to the sources, so these values should be taken as lower limits.

Finally, we find the expected number of foreground/background hard (soft) X-ray sources to fall within $3r_{50}$ of the galaxy. We use Equation 2 from Moretti et al. (2003) which, given an input flux, returns the expected number of background sources with that flux or higher that we would expect to see (per square degree). As our input fluxes, we use the minimum flux that we would classify as a source; we adopt 2 source counts, corresponding to the dimmest source we detected in each band. The resulting 2-10 keV (0.5-2 keV) minimum fluxes range from $S_{min} \sim$ 2-4.7 (0.7-2) in units of 10^{-15} erg s^{-1} cm^{-2} for our eleven *Chandra* observations. Using these fluxes, we find the expected number of hard band (soft band) background sources within $3r_{50}$ of our galaxies range between $\sim$0.001-0.014 (0.001-0.011).

X-ray sources are detected in seven of our eleven target galaxies (at most one per galaxy) − four BPT AGNs, one composite, and two star-forming galaxies. Six of the seven sources are consistent with being associated with the galaxy nucleus (see Section 3 for further discussion). The 2-10 keV X-ray luminosities have a range of $\log(L_{2-10\mathrm{keV}}/\mathrm{erg\ s^{-1}}) = 39.8$–41.9 (see Table 3.4). We use the aforementioned minimum fluxes to provide upper limits

on X-ray source luminosities for the remaining four galaxies with non-detections (one BPT AGN and three star-forming galaxies).

As most of our X-ray sources have a low number of counts, we estimate hardness ratios using the Bayesian Estimation of Hardness Ratios code (BEHR; Park et al., 2006), which is useful in the Poisson regime of low counts and works even if only one of the bands has a detection. Hardness ratio here is defined as $(H - S)/(H + S)$, where H and S are the number of detected counts in the hard and soft X-ray bands, respectively. Here, the soft and hard bands correspond to the energy ranges 0.5-2 keV and 2-7 keV, respectively. We have seven galaxies with detections in at least one of the two bands, and the resulting hardness ratios are displayed in Figure 3.4. We also estimate the hardness ratios using the Portable, Interactive Multi-Mission Simulator (PIMMS)[3] for absorbed power laws with $\Gamma = 1.8$ and $N_{\rm H} = 10^{22-24}$ cm^{-2} and for unabsorbed power laws with $\Gamma = 1.8$, 2.0, and 2.5. We plot these in Figure 3.4 as well.

Expected Contribution from X-ray Binaries

It can be helpful to establish a rough baseline of how much X-ray luminosity we would expect to see coming from each galaxy in the absence of any AGN − i.e. from X-ray binaries (XRBs). This expected X-ray luminosity scales with stellar mass for low-mass XRBs (Gilfanov, 2004) and with SFR for high-mass XRBs (Grimm et al., 2003). Applying the relation from Gilfanov (2004) between expected X-ray luminosity and stellar mass to our galaxies, we expect a luminosity of at most $\sim 10^{38}$ erg s^{-1} from low-mass XRBs. As this is $\sim$1.5 orders of magnitude smaller than the lowest observed X-ray luminosity, we conclude that low-mass XRBs are unlikely to significantly contribute to the luminosity of any of our observed X-ray sources; thus, we focus on high-mass XRBs.

We compare our observed X-ray luminosities to those expected from high-mass XRBs

[3] `https://heasarc.gsfc.nasa.gov/cgi-bin/Tools/w3pimms/w3pimms.pl`

Table 3.5. Host Galaxy SFRs and Expected Luminosity from XRBs

ID	FUV (mag)	log L(FUV) (erg s^{-1})	W_{22} (mag)	log L(22 μm) (erg s^{-1})	SFR^{Cor} ($M_\odot$ yr^{-1})	SFR^{Uncor} ($M_\odot$ yr^{-1})	12+log O/H
(1)	(2)	(3)	(4)	(5)	(6)	(7)	(8)
1	21.70	41.3	6.72	42.5	0.60	0.01	8.61
2	20.04	42.5	6.06	43.3	3.46	0.14	8.66
3	19.86	42.2	5.94	43.0	1.90	0.08	8.63
4	23.62	41.1	7.83	42.6	0.74	0.01	8.74
5	20.60	42.3	5.76	43.4	4.46	0.08	8.71
6	20.62	42.1	7.84	42.4	0.48	0.05	8.42
7	18.13	42.4	5.44	42.7	0.92	0.11	8.39
8	18.99	42.6	7.05	42.5	0.76	0.16	8.01
9	20.07	42.1	7.50	42.3	0.44	0.06	8.23
10	16.96	43.7	4.62	43.9	15.5	2.44	8.14
11	17.90	42.8	6.04	42.7	1.17	0.26	8.50

Note. — Column 1: Galaxy identification number used in this paper. Column 2: FUV AB magnitudes from *GALEX* (in the NSA). Column 3: log FUV luminosities. Column 4: *WISE* magnitudes (W4, 22 μm). Column 5: log 22 μm luminosities. Column 6: estimated SFRs from *GALEX* and *WISE* data. Column 7: estimated SFRs using only the uncorrected FUV luminosities. Column 8: metallicity estimated using the relation from Pettini & Pagel (2004).

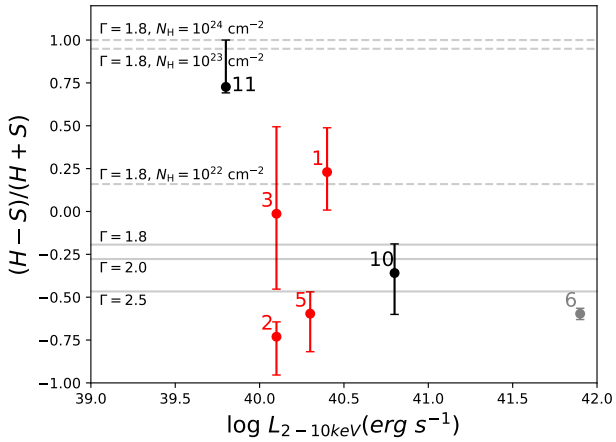


Figure 3.4 Hardness ratio vs. log 2-10 keV X-ray luminosity for the seven of our galaxies that had a detected X-ray source in at least one of the two bands. The hardness ratio was calculated using BEHR (see Section 3). The error bars are the 68% confidence intervals. Galaxies classified as AGN, composite, and star-forming are in red, grey, and black, respectively, based on the [N II]/Hα BPT diagram. Hardness ratios for unabsorbed power laws with $\Gamma = 1.8$, 2.0, and 2.5 are shown as grey solid lines, while power laws with various absorptions and $\Gamma = 1.8$ are shown as dashed grey lines.

using the model of Lehmer et al. (2021), which relates the expected XRB X-ray luminosity, SFR, and gas-phase metallicity. Figure 3.5 shows the median values and $16-84\%$ ranges of $L_{\rm X}$/SFR as a function of 12 + log(O/H) from their model (i.e., column 5 of table 3 in Lehmer et al., 2021). Here, $L_{\rm X}$ refers to X-ray luminosities in the 0.5-8 keV energy band. To this end, we re-analyze the *Chandra* data for our galaxies in the 0.5-8 keV band, using the same methodology as in Section 3. While the 1σ scatter for the Lehmer et al. (2021) relation is metallicity dependent (as evidenced by the changing 16-84% confidence intervals shown in blue in Figure 3.5), our target galaxies all have 12+ log (O/H) > 8.0 (see below) and the scatter in this range is less variable with a value of $\sim$0.2 dex.

In general, SFRs can be estimated using far-UV (FUV; 1528 Å) and mid-infrared (IR;

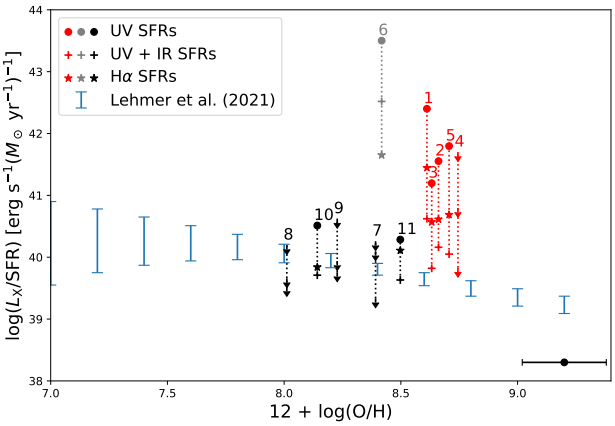


Figure 3.5 Log ratio of X-ray luminosity over host galaxy SFR vs. metallicity. The crosses represent SFRs calculated with the mid-IR-corrected FUV luminosities, the dots use the uncorrected FUV luminosities (see Equation 3.1), and the stars use the Hα derived SFRs - the three are connected by a dotted line for ease of comparison. SFRs based on the mid-IR-corrected FUV luminosities may be severely overestimated if the mid-IR emission is indeed dominated by an AGN as suggested by the *WISE* colors. Similarly, the Hα SFRs are also likely overestimated for the BPT AGNs/Composites since the AGN is contributing to or dominating the line ratios. Arrows indicate upper limits on the X-ray luminosities for galaxies with no significant hard X-ray source detections (calculated from the minimum fluxes). Galaxies classified as AGN, composite, and star-forming are in red, grey, and black, respectively (using the [N II]/Hα BPT diagram). The values and error bars in blue are the expected X-ray luminosity from XRBs from Lehmer et al. (2021). The $\sim$0.18 uncertainty in the metallicities is shown in black in the lower right-hand corner.

25 μm) luminosities as follows:

$$\begin{aligned} \log \mathrm{SFR}(M_\odot\ \mathrm{yr}^{-1}) &= \log\ L(\mathrm{FUV})_{\mathrm{corr}} - 43.35 \\ L(\mathrm{FUV})_{\mathrm{corr}} &= L(\mathrm{FUV})_{\mathrm{obs}} + 3.89 L(25\ \mu\mathrm{m}) \end{aligned} \tag{3.1}$$

(Hao et al., 2011; Kennicutt & Evans, 2012). The Hao et al. (2011) sample used to derive $L(\mathrm{FUV})_{\mathrm{corr}}$ includes normal star-forming galaxies in the local Universe drawn from the *Spitzer* Infrared Nearby Galaxies Survey (SINGS; Kennicutt et al., 2003) and the integrated spectrophotometric survey of Moustakas & Kennicutt (2006). Overall, the FUV and mid-IR luminosities of our target galaxies fall within the range of these samples (Hao et al., 2011; Kennicutt et al., 2009), albeit at the more sparsely populated low-luminosity end for the FUV. The uncertainty in the resulting SFRs is $\sim$0.13 dex.

These equations hold assuming the FUV and mid-IR emission is dominated by star formation. Given that our galaxies have mid-IR colors similar to luminous AGNs, and some show optical evidence for AGNs as well, it is likely that the mid-IR emission is contaminated or even dominated by AGNs in some cases. Therefore we treat SFRs calculated using the relations above as upper limits. We also calculate SFRs using only the FUV data since any potential (mid-IR selected) AGN is less likely to contribute at these short wavelengths. There could still be contamination from AGN emission, which would lead to overestimating the FUV luminosity and thus the SFR. However, this would move galaxies further upwards in Figure 3.5, resulting in even higher relative observed X-ray luminosities compared to what we would expect from XRBs.

We use FUV magnitudes from the *Galaxy Evolution Explorer* (*GALEX*) and 22 μm magnitudes from *WISE* in place of 25 μm luminosities from the *Infrared Astronomical Satellite* (*IRAS*). The ratio between 22 μm and 25 μm flux densities is expected to be of order one (Jarrett et al., 2013), and while none of our galaxies have *IRAS* detections, all eleven are detected by *WISE*. We summarize the resulting estimates for the SFRs in Table 3.5. The SFRs estimated from both FUV and mid-IR data (i.e., "corrected SFRs") span a range of 0.48–15.50 $M_{\odot}$ yr^{-1}, with a median of 0.92 $M_{\odot}$ yr^{-1}. The SFRs estimated from the uncorrected FUV luminosities are substantially lower with a range of 0.01–2.44 $M_{\odot}$ yr^{-1} and a median of 0.08 $M_{\odot}$ yr^{-1}.

As an additional check, we also estimate SFRs based on Hα emission in the SDSS spectroscopic fiber using the calibration in Kennicutt & Evans (2012). We use the flux measurements in the NSA and correct for extinction using the Balmer decrement. It is worth noting, however, that the 3″ fibers do not always cover the full extent of the galaxies, which could result in underestimating the SFRs. On the other hand, AGN emission will artificially boost the Hα luminosities and SFRs for the BPT AGN/Composite galaxies. We find that the Hα-derived SFRs generally fall in between the FUV and FUV+mid-IR SFRs discussed above.

We estimate metallicities via the relation from Pettini & Pagel (2004):

$$12 + \log\,(\mathrm{O/H}) = 8.90 + 0.57 \times \log\,[\mathrm{N\ II}]/\mathrm{H}\alpha. \tag{3.2}$$

The 1σ scatter in this relation is 0.18. Using our emission line measurements from SDSS spectroscopy, the metallicities of our targets have a range of 12+log (O/H) = 8.01-8.74, with a median of 8.50 (see Table 3.5). As this relation is derived from HII regions, it may not provide accurate results when applied to galaxies with AGNs. An AGN would likely increase the [N II]/Hα flux, thus increasing the derived metallicity. This provides a possible explanation for the separation via metallicity between the BPT AGN and SF galaxies in our sample, as can be seen in Figure 3.5.

From Figure 3.5, we can also see that the four BPT AGNs and one composite galaxy with X-ray detections have X-ray luminosities that are well above the expected contributions from high-mass XRBs when adopting the SFRs derived from FUV data and excluding the mid-IR emission (the latter of which is likely dominated by the AGN). The two BPT star-forming galaxies with X-ray detections have X-ray source luminosities closer to what is expected from XRBs. Specifically, using the FUV SFRs, the BPT AGN/Composite galaxies are $\sim 1.6 - 3.7$ dex higher than expected from the relation of Lehmer et al. (2021),

while the BPT star-forming galaxies are $\sim 0.1 - 0.7$ dex higher. In other words, the BPT AGN/Composite galaxies are at least $\sim 8\sigma$ higher than expected, while the BPT SF galaxies are at most $\sim 3.5\sigma$ higher. While these results do not rule out the presence of AGNs in the star-forming galaxies, it certainly does not add confidence to the AGN interpretation for star-forming galaxies with anomalous mid-IR colors. Table 3.6 summarizes the origin of the X-ray emission in our target galaxies.

The detected X-ray source luminosities are also generally consistent with ultra-luminous X-ray (ULX) sources, which are defined to be off-nuclear X-ray sources with $L_X > 10^{39}\,\mathrm{erg\,s^{-1}}$ (for a recent review of ULXs, see Kaaret et al., 2017). Though ULXs were initially considered strong candidates for typical sub-Eddington accretion onto intermediate-mass BHs (e.g., Sutton et al., 2012), spectroscopic and timing studies now strongly indicate super-Eddington accretion onto stellar mass sources, with several sources clearly identified as neutron stars due to the detection of X-ray pulsations (e.g., Bachetti et al., 2014) or cyclotron absorption features (Brightman et al., 2018). Indeed, based on broadband X-ray spectroscopy, Walton et al. (2018) suggest that the ULX population as a whole might be strongly dominated by neutron star accretors. However, ULXs are rare. ULXs are perhaps viable explanations for the X-ray sources in our BPT star-forming galaxies, though invoking such a scenario is unnecessary since the X-ray luminosities of these galaxies are consistent with the expectations for their X-ray binary population (e.g., Figure 3.5). We do not consider ULXs likely for the BPT AGN/Composite galaxies since the X-ray sources in these galaxies reside in prominent nuclei with additional multi-wavelength evidence for AGNs.

Optical/IR Counterparts of the X-ray Sources

Figure 3.3 shows the *HST* images of our target dwarf galaxies with the X-ray source positions overlaid in magenta (the magenta crosses and circles mark the positions and the 95% positional uncertainties). We also indicate the peak of the NIR emission in the galaxy

Table 3.6. Multiwavelength Properties of Dwarf Galaxies with Red Mid-IR Colors

ID	BPT Classification	X-ray Source	HST Optical/NIR Counterpart
1	AGN	AGN	prominent nucleus
2	AGN (with broad Hα)	AGN	prominent nucleus
3	AGN (with broad Hα)	AGN	prominent nucleus
4	AGN	non-detection	···
5	AGN	AGN	prominent nucleus
6	Comp. (with broad Hα)	AGN	prominent nucleus
7	SF	non-detection	···
8	SF	non-detection	···
9	SF	non-detection	···
10	SF	XRB/ULX or AGN	unknown (no *HST)*
11	SF	XRB/ULX or AGN	blue star clusters

Note. — All of our target galaxies were selected to have *WISE* mid-IR colors falling in the Jarrett et al. (2011) AGN selection box. Optical emission lines are measured from SDSS spectroscopy (Reines et al., 2013) and the classification is based on the BPT [O III]/Hβ vs. [N II]/Hα diagnostic diagram. X-ray classifications are based on whether the luminosity exceeds that expected from high-mass XRBs (indicating an AGN) or not (see Section 3; the BPT AGN/Composite galaxies are higher than the BPT SF galaxies by at least $\sim$4.5σ). Counterparts of the X-ray sources were determined from the *HST* imaging shown in Figure 3.3.

images using a green circle of radius 0.″4. The X-ray sources are almost certainly associated with the peak of the NIR emission for the four BPT AGNs (IDs 1-3,5) and one composite galaxy (ID 6) with X-ray detections. In these cases, the positions of the X-ray sources are consistent with prominent nuclei and there are no other obvious alternative optical/NIR counterparts. Of the two star-forming galaxies with detected X-ray sources, IDs 10 and 11, only ID 11 has *HST* imaging allowing us to determine optical counterparts of the X-ray source. In Figure 3.3 we see that the X-ray source has a larger offset from the peak of the NIR emission, and there are multiple blue (i.e., young) star clusters consistent with the position of the X-ray source that could host high-mass XRBs. While the X-ray source is consistent with being nuclear for ID 10, we lack HST images and are unsure whether or not this galaxy hosts star clusters close to the nucleus.

Given that our targets were selected to have mid-IR *WISE* colors falling in the Jarrett et al. (2011) AGN selected box, we also show the *WISE* W2 angular resolution as a red circle in Figure 3.3. In all cases, *WISE* is capturing mid-IR emission on galaxy-wide scales and we cannot definitively determine which *HST* sources are physically associated with the mid-IR emission. However, we deem it reasonable to conclude that the mid-IR emission in the BPT AGNs and the composite galaxy is in fact associated with AGNs since these galaxies have low amounts of star formation and compelling evidence for active massive BHs at multiple wavelengths. On the other hand, the mid-IR emission in the BPT star-forming galaxies could certainly be associated with young massive star clusters still partially embedded in their birth cocoons (e.g., Reines et al., 2008). None of the BPT star-forming galaxies have evidence for hosting AGNs other than red mid-IR colors. Moreover, they generally have relatively blue optical colors (Figure 3.6; also see Hainline et al., 2016) and multiple star clusters visible in the *HST* images, and one (ID 7) has visible extended dust lanes (see Figure 3.3). Nevertheless, we cannot rule out highly obscured AGNs in these star-forming galaxies, which could also account for the mid-IR colors.

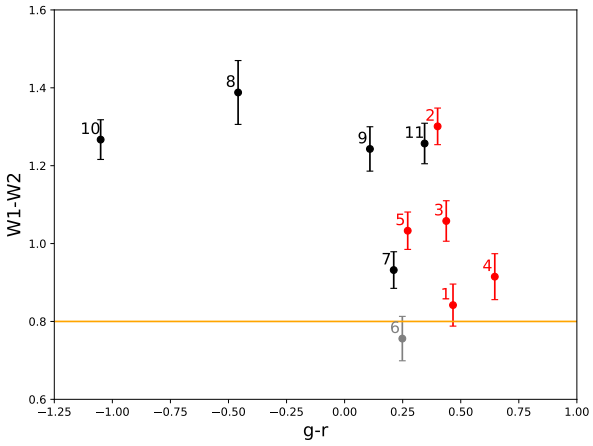


Figure 3.6 *WISE* W1-W2 color vs. $g-r$ color (from Table 3.1). The galaxies classified as AGN, composite, and star-forming are in red, grey, and black, respectively, based on the [N II]/Hα BPT diagram (left panel in Figure 3.2). In orange we show the W1-W2 > 0.8 selection criterion from Stern et al. (2012).

Multiwavelength AGN Scaling Relations

Here we compare the observed X-ray source luminosities to expectations based on AGN scaling relations for more massive galaxies relating X-ray luminosity to mid-IR luminosity, Hα luminosity and [O III] luminosity.

$L_{\rm X}$ vs. $L_{\rm IR}$ Figure 3.7 (top panel) shows the relation between $L_{2-10\ \rm keV}$ and $L_{\rm W2}$ (4.6 μm) from Secrest et al. (2015):

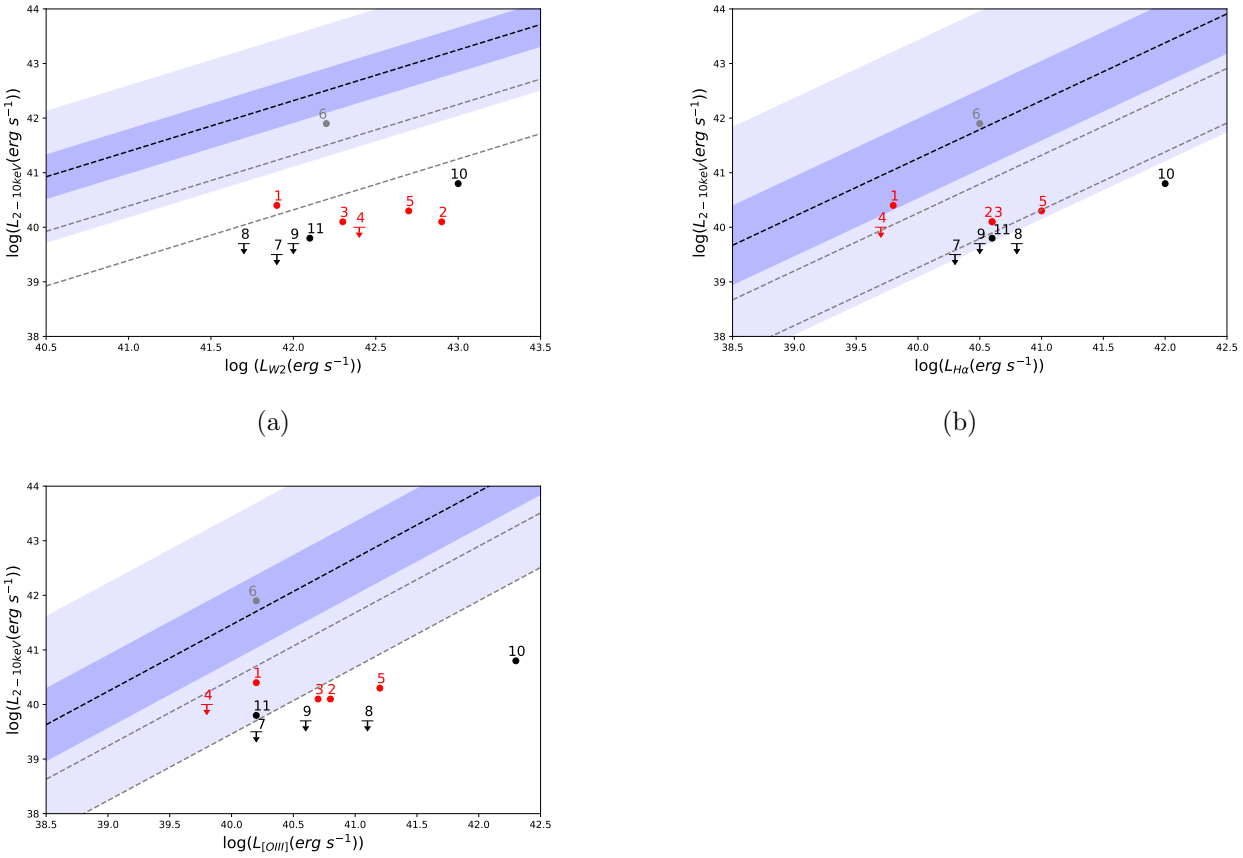
$$\log(L_{2-10\ \rm keV}) = (0.93 \pm 0.03) \cdot \log(L_{\rm W2}) + (3.26 \pm 1.25), \tag{3.3}$$

where the luminosities are in units of erg s^{-1} and the 1σ scatter is 0.40 dex. This relation was derived from a sample of 184 AGNs detected with *XMM* and *WISE* having both X-ray and mid-IR luminosities $\gtrsim 10^{42}$ erg s^{-1}. With the exception of ID 6 (a broad-line BPT

composite), all of the observed X-ray luminosities and upper limits in our sample are ~ 2 dex lower than the relation between $L_{2-10\ \mathrm{keV}}$ and L_{W2} based on more luminous and massive AGNs. We check this result using the relation from Gandhi et al. (2009), which was derived from a sample of 22 well-resolved AGNs and compares 12 μm luminosity to 2-10 keV X-ray luminosity. For this relation we use W3 fluxes from *WISE* and find similar results; the observed X-ray luminosities are lower than the relation by at least $\sim$1.5 dex (except ID 6). We consider three possible explanations for this discrepancy.

First, the mid-IR luminosities could be overestimated (and the sources could be pushed to the right) if there is a significant contribution from star formation. While our *Chandra* X-ray observations have high angular resolution ($\lesssim 1''$), the *WISE* W2 band data has an angular resolution of $6.4''$, which in nearly all cases is roughly on par with the size of the galaxies in our sample. However, we do not expect significant contamination from star formation in the mid-IR for the BPT AGNs (IDs 1-5). In order for these sources to be consistent with the $L_{\mathrm{X}} - L_{\mathrm{IR}}$ relation in Figure 3.7, we would have to be overestimating the mid-IR AGN luminosities by between 2.0-3.3 dex. This would imply the mid-IR emission is actually dominated by extreme star-formation, which seems highly unlikely given the optical line ratios and X-ray emission are dominated by AGNs. The origin of the mid-IR and X-ray emission in the BPT star-forming galaxies is unclear and may not have anything to do with AGNs.

A second possibility is that the mid-IR emission is dominated by highly obscured AGNs, such that the X-rays are greatly diminished. There are examples of Compton-thick AGNs in low-mass galaxies in the literature (e.g. Cann et al., 2020; Chen et al., 2017). Under the assumption that an AGN does indeed reside in each of our target galaxies, we can estimate the column density required to suppress the X-ray emission below the $L_{\mathrm{X}} - L_{\mathrm{IR}}$ relation (assuming that intrinsic X-ray luminosity is consistent with said relation). Using PIMMS, we find that the estimated column densities are all (except ID 6) high enough to qualify as



(a) (b) (c)

Figure 3.7 Observed X-ray luminosities vs W2 (top), Hα (middle), and [O III] (bottom) luminosities for our galaxies. Galaxies classified as AGN, composite, and star-forming are in red, grey, and black, respectively. The arrows indicate that the X-ray luminosity comes from an upper limit (calculated from minimum fluxes - see Section 3). The black dashed lines indicate the expected X-ray luminosity using the Secrest et al. (2015) relation (top, mid-IR; Equation 3.3) and the relations from Panessa et al. (2006) (middle, Hα, Equation 3.4; bottom, [O III], Equation 3.5). The dark blue shaded areas represent the 1σ scatters and the light blue shaded areas represent the 3σ scatters. The dashed grey lines represent the relations shifted down by 1 and 2 dex, for ease of comparison with the plotted points.

Compton-thick with $N_{\rm H} > 10^{24}$ cm^{-2}. See Table 3.7 for specific values and Figure 3.8 for a visual depiction. However, if Compton-thick AGNs resided in our target galaxies, we would expect to see hints in the X-ray emission. For example, if the AGNs were Compton-thick we would expect more photons at higher energies yielding a positive hardness ratio. Figure 3.4 demonstrates this is generally not the case. Three of the five BPT AGNs/composities (IDs 2,5,6) fall firmly in the soft range, and two BPT AGNs (IDs 1,3) are ambiguous. While Compton-thick AGNs also typically have strong Fe Kα emission, this may not always be the case for heavily obscured and X-ray faint AGNs (see Chen et al., 2017). Nevertheless, using the `CIAO` function `specextract`, we check both individual and stacked X-ray spectra for the BPT AGN and Composite galaxies with X-ray detections and find no evidence for Fe Kα emission. Additionally, broad optical emission lines are generally not observed in obscured AGNs (Hickox & Alexander, 2018), and we do see broad Hα in three of our X-ray detected AGNs (IDs 2,3,6).

An alternative explanation for the low X-ray luminosities is that the AGNs could be intrinsically X-ray weak (e.g., Baldassare et al., 2017; Dong et al., 2012). It has been proposed that some AGNs in metal-poor host galaxies could simply lack the hard X-ray emission we would expect to see (Simmonds et al., 2016). Similar conclusions have been found regarding AGNs with weak broad lines that are not necessarily obscured (Denney et al., 2014; Hickox & Alexander, 2018; LaMassa et al., 2015; MacLeod et al., 2016).

Finally, it is entirely possible that the $L_{\rm X} - L_{\rm IR}$ relation simply breaks down at low BH masses or is steeper than has been captured by relations calibrated at higher luminosities. Perhaps these relations cannot be properly extrapolated to dwarf galaxies, where there may be a change in the AGN spectral energy distribution and/or dust properties.

$L_{\rm X}$ vs. $L_{\rm H\alpha}$ and $L_{\rm [O\ III]}$ Figure 3.7 (middle, bottom panels) shows the $L_{\rm 2-10\ keV} - L_{\rm H\alpha}$ and $L_{\rm 2-10\ keV} - L_{\rm [O\ III]}$ relations from Panessa et al. (2006):

Table 3.7. Expected $L_{\rm X}$ from $L_{\rm IR}$

ID	$W_{4.6}$ (mag)	log $W_{4.6}$ (erg s^{-1})	log $L_{\rm X}^{\rm Obs}$ (erg s^{-1})	log $L_{\rm X}^{\rm Exp}$ (erg s^{-1})	$N_{\rm H}$ (10^{24} cm^{-2})
(1)	(2)	(3)	(4)	(5)	(6)
1	13.17	41.9	40.4	42.3	3.21
2	12.10	42.9	40.1	43.1	6.00
3	12.80	42.3	40.1	42.6	4.60
4	13.36	42.4	<40.0	42.7	>5.14
5	12.48	42.7	40.3	43.0	5.19
6	13.37	42.2	41.9	42.5	0.59
7	12.38	41.9	<39.5	42.2	>5.20
8	14.20	41.7	<39.7	42.0	>4.25
9	13.28	42.0	<39.7	42.3	>5.06
10	11.77	43.0	40.8	43.3	4.56
11	12.50	42.1	39.8	42.4	4.99

Note. — Column 1: Identification number used in this paper. Column 2: *WISE* magnitudes (W2, 4.6 μm). Column 3: log 4.6 μm ($W2$) luminosities. Column 4: log observed 2-10 keV X-ray luminosities; galaxy IDs 4, 7-9 had no X-ray detections, so we instead state the calculated minimum detectable luminosities using the minimum observable fluxes (see Section 3). Column 5: expected log 2-10 keV X-ray luminosities, calculated using Equation 3.3. Column 6: Estimated intrinsic hydrogen column density required to match our observed X-ray luminosities with those predicted by the Secrest et al. (2015) relation (see Equation 3.3).

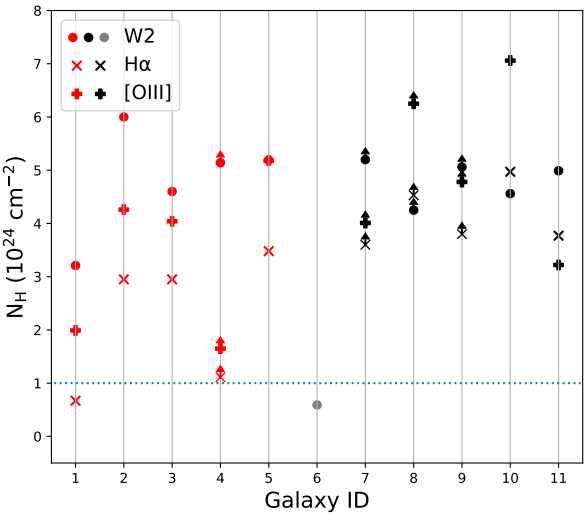


Figure 3.8 Estimated intrinsic absorption ($N_{\rm H}$) in each galaxy using the difference between the expected and observed X-ray luminosities. Galaxies classified as AGN, composite, and star-forming are in red, grey, and black, respectively. The dots, x's, and plus signs use the expected X-ray luminosity as calculated from the W2, Hα, or [O III] relations, respectively. The arrows indicate that the observed X-ray luminosity comes from an upper limit calculated from minimum fluxes, which translates into a lower limit for $N_{\rm H}$. The dotted blue line at $N_{\rm H} = 10^{24}$ cm^{-2} separates out the plot into Compton thick (above the line) and Compton thin (below the line) regions. Note that several estimates of $N_{\rm H}$ are unavailable (e.g. the Hα and [O III] relations for ID 6) − in these cases, the observed X-ray luminosity was higher than the expected X-ray luminosity, so an estimate was unable to be calculated. Note also that for ID 6, Baldassare et al. (2017) found via spectral fitting that the models did not prefer an $N_{\rm H}$ greater than the Galactic value, suggesting little to no intrinsic absorption.

$$\log(L_{2-10\ \rm keV}) = (1.06 \pm 0.04) \cdot \log(L_{\rm H\alpha}) + (-1.14 \pm 1.78) \tag{3.4}$$

$$\log(L_{2-10\ \mathrm{keV}}) = (1.22 \pm 0.06) \cdot \log(L_{[\mathrm{O\ III}]}) + (-7.34 \pm 2.53), \tag{3.5}$$

where the luminosities are in erg s^{-1}. These relations are based on a sample of Seyferts from the Palomar optical spectroscopic survey of nearby galaxies (Ho et al., 1995), and the luminosities ($\log L_{\mathrm{X}}/\mathrm{erg\ s}^{-1} = 38.2$-$43.3$) are measured in the nuclear regions of the galaxies (i.e., not the entire galaxy; Panessa et al., 2006). The Hα luminosities used in Panessa et al. (2006) are from the combined narrow and broad (if present) components and are corrected for extinction. We also include both narrow and broad Hα components (when detected). While our Hα luminosities are not corrected for extinction, this would only increase our luminosities and push them further to the right in Figure 3.7, thereby increasing the disparity between expected and observed X-ray luminosities.

We estimate the scatter in these relations by taking the standard deviation of the differences between the observed and expected X-ray luminosities of the original sample of Panessa et al. (2006), excluding galaxies that lack detection in one or more of X-ray, Hα, or [O III] bands (see Table 2 in Panessa et al., 2006). We find a scatter of $\sim$0.72 and $\sim$0.66 dex for the Hα and [O III] relations, respectively. This does not include uncertainties associated with the fitted parameters in the Panessa et al. (2006) relation.

Our dwarf galaxies are also shown in Figure 3.7 using our *Chandra* X-ray luminosities and line measurements from SDSS spectroscopy (Reines et al., 2013) $-$ see Tables 3.8 and 3.9 for specific values. The points fall systematically below the $L_{\mathrm{X}} - L_{[\mathrm{O\ III}]}$ and $L_{\mathrm{X}} - L_{\mathrm{H}\alpha}$ relations, but some of the sources are within the 3σ scatter. We note that we do not find any systematic difference between the broad-line and narrow-line AGNs with respect to these relations when considering our sample and the additional broad-line AGNs in dwarf galaxies presented in Baldassare et al. (2017).

Again, we consider various explanations for our targets generally falling below the

relations. We do not expect that we are significantly overestimating the line luminosities even though the measurements come from SDSS spectra taken with a 3″-aperture (see Figure 3.3). In order to match the relation, we would have to be overestimating the Hα and [O III] luminosities of the BPT AGNs by 0.6-1.9 dex and 1.0-2.2 dex, respectively, and therefore star formation would have to dominate the line emission. Given that the line ratios for these galaxies indicate the emission is dominated by AGNs, we rule this scenario out. Similar to the $L_{\rm X} - L_{\rm IR}$ relation, we conclude that the $L_{\rm X} - L_{\rm [O\ III]}$ and $L_{\rm X} - L_{\rm H\alpha}$ relations are either not applicable to AGNs with low BH masses, which may be intrinsically X-ray weak, or the relations do not properly extrapolate to dwarf galaxies and may need to be revisited with expanded samples including more such objects.

Summary and Conclusions

We have presented high-resolution *Chandra* observations of eleven dwarf galaxies having mid-IR selected candidate AGNs culled from the sample of Hainline et al. (2016). Multi-band *HST* observations are also presented for ten of these galaxies. Based on optical SDSS spectroscopy (Reines et al., 2013), five of our target galaxies are classified as BPT AGNs (two of which have broad lines), five as star-forming, and one as Composite (which also has broad lines). Using a suite of multiwavelength diagnostics, we investigate whether mid-IR color-color AGN selection (e.g. Jarrett et al., 2011) is effective when applied to low-mass galaxies. Our primary findings are summarized below (also see Table 3.6).

1. We detect seven X-ray point sources across our sample of eleven dwarf galaxies, with luminosities in the range $\log(L_{2-10{\rm keV}}/{\rm erg\ s^{-1}}) = 39.8$–$41.9$. Five of these sources are in BPT AGN or Composite galaxies, and two are in BPT star-forming galaxies.

2. There is strong evidence that the X-ray sources detected in the five optically-selected BPT AGN and Composite galaxies (IDs 1,2,3,5,6) are indeed accreting massive BHs

Table 3.8. Expected $L_{\rm X}$ from $L_{\rm H\alpha}$

ID	$F_{\rm H\alpha}$ (10^{-16} erg s^{-1} cm^{-2})	log $L_{\rm H\alpha}$ (erg s^{-1})	log $L_{\rm X}^{\rm Obs}$ (erg s^{-1})	log $L_{\rm X}^{\rm Exp}$ (erg s^{-1})	$N_{\rm H}$ (10^{24} cm^{-2})
(1)	(2)	(3)	(4)	(5)	(6)
1	41.77	39.8	40.4	41.0	0.67
2	53.02	40.6	40.1	41.9	2.95
3	164.28	40.6	40.1	41.9	2.95
4	9.43	39.7	<40.0	40.9	>1.11
5	204.76	41.0	40.3	42.3	3.48
6	49.84	40.5	41.9	41.8	N/A[4]
7	315.78	40.3	<39.5	41.6	>3.60
8	329.23	40.8	<39.7	42.1	>4.53
9	177.75	40.5	<39.7	41.8	>3.80
10	2343.00	42.0	40.8	43.4	4.97
11	368.45	40.6	39.8	41.9	3.77

Note. — Column 1: Identification number used in this paper. Column 2: Hα flux. Column 3: log Hα luminosity. This include both narrow and broad (if present) components. Column 4: log observed 2-10 keV X-ray luminosity. Column 5: expected log 2-10 keV X-ray luminosity, calculated using Equation 3.4. Column 6: Estimated intrinsic hydrogen column density required to match our observed X-ray luminosities with those predicted by the Panessa et al. (2006) relation (see Equation 3.4).

Table 3.9. Expected $L_{\rm X}$ from $L_{\rm [O\ III]}$

ID	$F_{\rm [O\ III]}$ (10^{-16} erg s^{-1} cm^{-2})	log $L_{\rm [O\ III]}$ (erg s^{-1})	log $L_{\rm X}^{\rm Obs}$ (erg s^{-1})	log $L_{\rm X}^{\rm Exp}$ (erg s^{-1})	$N_{\rm H}$ (10^{24} cm^{-2})
(1)	(2)	(3)	(4)	(5)	(6)
1	111.86	40.2	40.4	41.7	1.99
2	139.83	40.8	40.1	42.4	4.26
3	243.27	40.7	40.1	42.3	4.04
4	11.97	39.8	<40.0	41.2	>1.65
5	390.51	41.2	40.3	43.0	5.18
6	51.16	40.2	41.9	41.7	N/A[5]
7	275.72	40.2	<39.5	41.7	>4.01
8	630.52	41.1	<39.7	42.8	>6.25
9	219.95	40.6	<39.7	42.2	>4.78
10	3969.37	42.3	40.8	44.2	7.06
11	133.58	40.2	39.8	41.7	3.22

Note. — Column 1: Identification number used in this paper. Column 2: [O III] flux. Column 3: log [O III] luminosity. Column 4: log observed 2-10 keV X-ray luminosity. Column 5: expected log 2-10 keV X-ray luminosity, calculated using Equation 3.5. Column 6: Estimated intrinsic hydrogen column density required to match our observed X-ray luminosities with those predicted by the Panessa et al. (2006) relation (see Equation 3.5).

in the nuclei of their host galaxies. The X-ray luminosities are well above the expected contribution from XRBs, and the positions of the X-ray sources are consistent with prominent nuclei, the peak of the NIR emission in the *HST* images, and the centroid of the mid-IR emission from *WISE* (see Figure 3.3). It is thus reasonable to attribute the detected mid-IR emission from *WISE* to these optically-selected AGNs.

3. The same cannot be said of the BPT star-forming galaxies. Only two of five of these galaxies have X-ray detections (IDs 10,11) and the X-ray luminosities are not so high as to rule out high-mass XRBs. Additionally, *HST* imaging of ID 11 indicates the X-ray source is associated with blue (i.e. young) star clusters that are plausible hosts of an XRB/ULX. The X-ray source in this galaxy is also significantly offset from the peak of the NIR emission and the centroid of the mid-IR emission (see Figure 3.3), strongly suggesting different origins for the X-ray and mid-IR sources. While the X-ray source in ID 10 is consistent with the nucleus of the galaxy, without HST imaging we cannot rule out the possibility of star clusters close to the nucleus, and as such cannot reliably determine the optical counterpart of the X-ray source.

4. We compare the observed X-ray luminosities to those expected from AGN scaling relations using mid-IR, Hα, and [O III] luminosities. In nearly all cases, we find that the observed X-ray emission falls below the relations (see Figure 3.7), with the largest discrepancies for the $L_{\rm X} - L_{\rm IR}$ relation. We consider various explanations and hypothesize that the sources are either intrinsically X-ray weak, or that the scaling relations break down in (or cannot be reliably extrapolated to) the regime of low-mass galaxies/BHs (see Sections 3 and 3).

The work of Hainline et al. (2016) demonstrated that using a single *WISE* $W1 - W2$ color cut to select AGN candidates in dwarf galaxies led to severe contamination from young starbursts. Here we show that using a more stringent color-color selection (i.e., Jarrett et al.,

2011) still leads to unreliable results for optically-selected star-forming dwarf galaxies. While the WISE color-color selection for our sample of BPT AGN and Composite galaxies seems to be reliable, this mid-IR selection method misses many optically selected AGN and Composite galaxies (see Figure 1 in Hainline et al., 2016). We also demonstrate that $\sim 80-90\%$ of the secure mid-IR selected AGNs in our sample (with optical and X-ray evidence for AGNs) have lower than expected X-ray luminosities when compared to multiwavelength scaling relations based on more massive/luminous systems, suggesting these mid-IR selected AGNs are either highly obscured, intrinsically X-ray weak, or that the scaling relations break down when applied to low-mass galaxies such as we have here.

Recently, there have been additional papers analyzing the efficacy of these mid-IR selection techniques. Satyapal et al. (2018) use photoionization and stellar population synthesis models to model AGNs and starbursts, finding that in some extreme cases these starbursts can have mid-IR colors that would classify them as AGNs using a one-band ($W1-W2$) color cut (e.g., Stern et al., 2012). They also find that abnormally high ionization parameters or gas densities would be required for a starburst to be classified as an AGN using the two-band color cut of Jarrett et al. (2011), and that these conditions are inconsistent with current observations of star-forming galaxies. Our observational findings presented here suggest such extreme conditions do exist in at least some star-forming dwarf galaxies, or that other physical processes are causing them to fall in the Jarrett et al. (2011) AGN selection box.

Mid-IR AGN selection in dwarfs also has issues due to the relatively poor resolution of *WISE* compared to optical surveys, potentially resulting in contamination due to overlapping sources. Lupi et al. (2020) re-analyzed the sample of Kaviraj et al. (2019), who combined optical and infrared data from the Hyper Suprime-Cam (HSC; Aihara et al., 2018) and *WISE*, respectively, in order to search for AGN in dwarf galaxies. Kaviraj et al. (2019) find an AGN occupation fraction of $10-30\%$ in their sample of $\sim$800 galaxies, which is much

larger than surveys at other wavelengths. The re-analysis by Lupi et al. (2020) takes into account resolution effects and source overlapping, as HSC has a resolution of $\sim 0\farcs6$ compared to *WISE* with $\sim 6''$. Lupi et al. (2020) match HSC sources to *WISE* sources (and apply an additional signal-to-noise ratio cut for the W3 emission), arriving at a sample of $\sim$500 dwarf galaxies. All but 15 of these dwarfs are in groups, with multiple HSC sources associated with one *WISE* source. Assuming the *WISE* source is associated with a dwarf, as opposed to a more luminous galaxy in the group that is also consistent with the *WISE* source, leads to errors in the AGN fraction in dwarf galaxies. Lupi et al. (2020) account for this effect and find an AGN occupation fraction of $\sim$0.4%, consistent with other results.

While mid-IR AGN selection in dwarf galaxies at the angular resolution of *WISE* appears to be fraught with problems, mid-IR prospects are likely to improve in the near future. The *James Webb Space Telescope (JWST)* will yield significantly higher resolution images in the infrared and facilitate the study of IR coronal emission lines to help identify elusive AGNs (Cann et al., 2018; Satyapal et al., 2021).

We thank the anonymous referee for their helpful comments. Support for this work was provided by NASA through *Chandra* Award Number GO9-20094X issued by the *Chandra X-ray Observatory Center*, which is operated by the Smithsonian Astrophysical Observatory for and on behalf of the NASA under contract NAS8-03060. Based on observations with the NASA/ESA *Hubble Space Telescope* obtained from MAST at the Space Telescope Science Institute, which is operated by the Association of Universities for Research in Astronomy, Incorporated, under NASA contract NAS5-26555. Support for Program number HST-GO-15607.001-A was provided through a grant from the STScI under NASA contract NAS5-26555. AER also acknowledges support for this work provided by NASA through EPSCoR grant number 80NSSC20M0231. The work of DS was carried out at the Jet Propulsion Laboratory, California Institute of Technology, under a contract with NASA.

The Legacy Surveys consist of three individual and complementary projects: the Dark Energy Camera Legacy Survey (DECaLS; Proposal ID #2014B-0404; PIs: David Schlegel and Arjun Dey), the Beijing-Arizona Sky Survey (BASS; NOAO Prop. ID #2015A-0801; PIs: Zhou Xu and Xiaohui Fan), and the Mayall z-band Legacy Survey (MzLS; Prop. ID #2016A-0453; PI: Arjun Dey). DECaLS, BASS and MzLS together include data obtained, respectively, at the Blanco telescope, Cerro Tololo Inter-American Observatory, NSF's NOIRLab; the Bok telescope, Steward Observatory, University of Arizona; and the Mayall telescope, Kitt Peak National Observatory, NOIRLab. The Legacy Surveys project is honored to be permitted to conduct astronomical research on Iolkam Du'ag (Kitt Peak), a mountain with particular significance to the Tohono O'odham Nation.

NOIRLab is operated by the Association of Universities for Research in Astronomy (AURA) under a cooperative agreement with the National Science Foundation.

This project used data obtained with the Dark Energy Camera (DECam), which was constructed by the Dark Energy Survey (DES) collaboration. Funding for the DES Projects has been provided by the U.S. Department of Energy, the U.S. National Science

Foundation, the Ministry of Science and Education of Spain, the Science and Technology Facilities Council of the United Kingdom, the Higher Education Funding Council for England, the National Center for Supercomputing Applications at the University of Illinois at Urbana-Champaign, the Kavli Institute of Cosmological Physics at the University of Chicago, Center for Cosmology and Astro-Particle Physics at the Ohio State University, the Mitchell Institute for Fundamental Physics and Astronomy at Texas A&M University, Financiadora de Estudos e Projetos, Fundacao Carlos Chagas Filho de Amparo, Financiadora de Estudos e Projetos, Fundacao Carlos Chagas Filho de Amparo a Pesquisa do Estado do Rio de Janeiro, Conselho Nacional de Desenvolvimento Cientifico e Tecnologico and the Ministerio da Ciencia, Tecnologia e Inovacao, the Deutsche Forschungsgemeinschaft and the Collaborating Institutions in the Dark Energy Survey. The Collaborating Institutions are Argonne National Laboratory, the University of California at Santa Cruz, the University of Cambridge, Centro de Investigaciones Energeticas, Medioambientales y Tecnologicas-Madrid, the University of Chicago, University College London, the DES-Brazil Consortium, the University of Edinburgh, the Eidgenossische Technische Hochschule (ETH) Zurich, Fermi National Accelerator Laboratory, the University of Illinois at Urbana-Champaign, the Institut de Ciencies de l'Espai (IEEC/CSIC), the Institut de Fisica d'Altes Energies, Lawrence Berkeley National Laboratory, the Ludwig Maximilians Universitat Munchen and the associated Excellence Cluster Universe, the University of Michigan, NSF's NOIRLab, the University of Nottingham, the Ohio State University, the University of Pennsylvania, the University of Portsmouth, SLAC National Accelerator Laboratory, Stanford University, the University of Sussex, and Texas A&M University.

BASS is a key project of the Telescope Access Program (TAP), which has been funded by the National Astronomical Observatories of China, the Chinese Academy of Sciences (the Strategic Priority Research Program "The Emergence of Cosmological Structures" Grant # XDB09000000), and the Special Fund for Astronomy from the Ministry of

Finance. The BASS is also supported by the External Cooperation Program of Chinese Academy of Sciences (Grant # 114A11KYSB20160057), and Chinese National Natural Science Foundation (Grant # 11433005).

The Legacy Survey team makes use of data products from the Near-Earth Object Wide-field Infrared Survey Explorer (NEOWISE), which is a project of the Jet Propulsion Laboratory/California Institute of Technology. NEOWISE is funded by the National Aeronautics and Space Administration.

The Legacy Surveys imaging of the DESI footprint is supported by the Director, Office of Science, Office of High Energy Physics of the U.S. Department of Energy under Contract No. DE-AC02-05CH1123, by the National Energy Research Scientific Computing Center, a DOE Office of Science User Facility under the same contract; and by the U.S. National Science Foundation, Division of Astronomical Sciences under Contract No. AST-0950945 to NOAO.

THE AGN FRACTION IN DWARF GALAXIES FROM EROSITA: FIRST RESULTS AND FUTURE PROSPECTS

Contribution of Authors and Co-Authors

Manuscript in Chapter 4

Author: Lilikoi J. Latimer

Contributions: Reduced and analyzed X-ray data, wrote initial draft of manuscript.

Author: Amy E. Reines

Contributions: Advised, helped edit manuscript, provided scientific and editorial comments on the manuscript.

Author: Akos Bogdan

Contributions: Helped analyze X-ray data, provided scientific and editorial comments on the manuscript.

Author: Ralph Kraft

Contributions: Provided scientific and editorial comments on the manuscript.

Manuscript Information

Lilikoi J. Latimer, Amy E. Reines, Akos Bogdan, Ralph Kraft

The Astrophysical Journal Letters

Status of Manuscript:
____ Prepared for submission to a peer-reviewed journal
____ Officially submitted to a peer-reviewed journal
____ Accepted by a peer-reviewed journal
_X_ Published in a peer-reviewed journal

IOP Publishing
The Astrophysical Journal Letters, Volume 922, Number 2
10.3847/2041-8213/ac3af6

Introduction

Massive black holes (BHs) with $M_{\rm BH} \sim 10^{6-9} M_{\odot}$ reside at the center of nearly all massive galaxies. Some of these BHs are accreting at sufficient rates such that they are detectable as active galactic nuclei (AGNs). The prevalence of massive BHs and the AGN fraction in dwarf galaxies ($M_{\star} \lesssim 10^{9.5}\ M_{\odot}$; $M_{\rm BH} \lesssim 10^{5} M_{\odot}$) is much more uncertain, yet extremely important for our understanding of the origin of BH seeds (Greene et al., 2020), the role of BH feedback at low masses (Silk, 2017), and the overall demographics of massive BHs since dwarfs are the most numerous types of galaxies in the Universe.

There are various ways to search for active massive BHs in dwarf galaxies, including optical emission line diagnostics (e.g., Molina et al., 2021; Reines et al., 2013), optical variability (e.g., Baldassare et al., 2020), mid-IR colors (e.g., Hainline et al., 2016; Latimer et al., 2021b; Lupi et al., 2020) and radio observations (Mezcua et al., 2019; Reines et al., 2020). While all techniques suffer from various selection effects, X-ray observations are particularly well-suited to detecting BHs that are accreting at low Eddington ratios (Gallo et al., 2008; Hickox et al., 2009) and/or residing in host galaxies with ongoing star formation (Kimbro et al., 2021; Reines et al., 2016).

Previous X-ray studies have been used to explore the BH occupation fraction in low mass early-type spheroidal galaxies and late-type spirals, as well as to search for AGNs in the general population of dwarf galaxies. For example, Miller et al. (2015) used *Chandra* X-ray data from the AMUSE[1]-Virgo (Gallo et al., 2008; Gallo et al., 2010) and AMUSE-Field (Miller et al., 2012) surveys to constrain the BH occupation fraction to be $> 20\%$ for early-type galaxies with $M_{\star} \sim 10^{9} - 10^{10}\ M_{\odot}$. A similar occupation fraction is found for late-type spirals by She et al. (2017) using data in the *Chandra* archive. Candidate AGNs in dwarf galaxies with $M_{\star} \lesssim 10^{9.5}\ M_{\odot}$ have been found using the Chandra Deep Field South

[1]AGN Multiwavelength Survey of Early-Type Galaxies

Survey (Schramm et al., 2013), archival data in the Chandra Source Catalog (Lemons et al., 2015), the Chandra COSMOS-Legacy Survey (Mezcua et al., 2018) and the 3XMM catalog (Birchall et al., 2020).

While much progress has been made in recent years, previous X-ray studies have been affected by incompleteness effects, small sample sizes, and are generally expensive with pointing telescopes since most of the dwarf galaxies will not have an AGN. Large-area X-ray surveys can overcome these issues and are one of the best methods to identify AGNs. In this Letter, we explore the AGN fraction in dwarf galaxies using unbiased X-ray observations from the eROSITA Final Equatorial Depth Survey (eFEDS; Brunner et al., 2021). This work provides a sneak peek into the very near future when the eROSITA All-Sky Survey (eRASS) will be available, which could revolutionize our understanding of AGNs in dwarf galaxies.

Data

eROSITA/eFEDS

eROSITA is the primary instrument on the Spectrum-Roentgen-Gamma (SRG) mission. It was launched into space on July 13, 2019 and five months later started a survey of the entire sky, which is predicted to finish in 2023. eROSITA is a wide-field X-ray telescope operating in the 0.2-8 keV energy range, with an average on-axis resolution of $\sim$16″at 1.5 keV. It was designed to be $\sim$25 times more sensitive than the ROSAT all-sky survey in the 0.2-2.3 keV band. The nominal positional accuracy of eROSITA is 3″. For more details on eROSITA, see Predehl et al. (2021).

The eFEDS catalog is based off of observations taken by eROSITA during its performance verification phase ahead of the all-sky survey. eFEDS has a sky footprint of $\sim$140 deg^2 (1/300th of the sky), which is broken up into four $\sim$35 deg^2 rectangular, semi-adjacent sub-fields of 4.2°$\times$ 7.0° (for a visualization, see Figure 1 in Brunner et al., 2021).

This observational strategy was designed to provide uniform exposure over this field and to be ∼50% deeper than is expected for the future eROSITA all-sky survey. The eFEDS catalog contains 27,910 X-ray sources detected in the 0.2-2.3 keV band, with a nominal (point source) flux limit of $\sim 7 \times 10^{-15}$ erg cm^{-2} s^{-1} in the $0.5 - 2$ keV band − at this level, the fraction of spurious contaminating sources is expected to be 6.4%. The completeness is given as 96% at a $0.5 - 2$ keV band flux limit of 10^{-14} erg cm^{-2} s^{-1}, and down to 65% at a flux limit of 4×10^{-15} erg cm^{-2} s^{-1}.

The eFEDS catalog has a source density larger than the ROSAT All-Sky survey (Boller et al., 2016) by a factor of 70, and has a quite uniform source density across its coverage. Astrometric corrections were found by matching eFEDS sources to the catalog of Gaia-unWISE AGN candidates from Shu et al. (2019), as described in Brunner et al. (2021). Additionally, Brunner et al. (2021) compare the eFEDS source fluxes to those of sources in the same footprint appearing in the XMM-ATLAS survey (Ranalli et al., 2015), and find no evidence for strong systematic offsets.

Sample of Dwarf Galaxies

We draw our parent sample of dwarf galaxies from the NSA (v1_0_1), a catalog of local ($z \leq 0.15$) galaxies and associated parameters derived via images from the Sloan Digital Sky Survey (SDSS) and the *Galaxy Evolution Explorer (GALEX)*. Galaxy stellar masses are calculated using `kcorrect` v4_2 (Blanton & Roweis, 2007), and are given in units of $M_{\odot}h^{-2}$. We adopt $h = 0.73$, and use the catalog values derived from elliptical Petrosian photometry. We filter the NSA for dwarf galaxies by excluding any galaxies with masses above 3×10^9 $M_{\odot}$. This results in a parent sample of 63,582 dwarf galaxies.

While we use this entire parent sample for matching dwarf galaxies to eFEDS sources (Section 4), we note that the eFEDS sky coverage is significantly smaller than that of the

NSA; 140 deg^2 (Brunner et al., 2021) vs. 14,555 square degrees[2]. To estimate how many dwarf galaxies (in the NSA catalog) reside within the eFEDS footprint, we first approximate the eFEDs sky coverage by using a bounding box, determined by the maximum and minimum X-ray source R.A. and Declination values as reported in the eFEDS catalog. We then search the NSA for dwarf galaxies lying within this area, resulting in 495 dwarf galaxies (an upper limit, given our use of a bounding box).

We also note that, while the NSA sky footprint overlays nearly the entire eFEDS coverage, there are a few small parts of the southern-most regions of eFEDS that may lie outside the NSA coverage (see Figure 1 in Brunner et al., 2021); however, as the overwhelming majority of eFEDS is covered, we expect this effect to be negligible.

Analysis and Results

Dwarf Galaxies with X-ray Detections

To find dwarf galaxies with coincident X-ray detections, we first cross-match X-ray sources from the eFEDS main catalog[3] with the NSA sample of 495 dwarf galaxies that lie within the eFEDS footprint. We include matches in which the separation between the X-ray source and the galaxy optical center is less than two Petrosian 50% light radii ($2r_{50}$). This results in six galaxies matching to six X-ray sources (one per galaxy; see Figure 4.1). We check to ensure that our matched galaxies are indeed dwarfs by determining if they have reliable redshifts and ensuring that the absolute magnitudes are not anomalously bright. All six galaxies pass these tests.

Our final sample consists of six dwarf galaxies, each with a single associated eFEDS X-ray point source. We check these X-ray sources against the ROSAT all-sky survey source catalog (Boller et al., 2016), the XMM-ATLAS catalog (Ranalli et al., 2015), and the Chandra

[2] https://www.sdss.org/dr13/scope/

[3] https://erosita.mpe.mpg.de/edr/eROSITAObservations/Catalogues/

Source Catalog 2.0[4], finding no matches. The galaxy properties of our sample are summarized in Table 4.1, and three-color optical images with X-ray source positions are shown in Figure 4.1. Only one galaxy has an X-ray source clearly associated with the nucleus (ID 3). The remaining five X-ray sources have centroids that are offset from the optical centers of the galaxies by 1.″8-25.″8, although three of these (IDs 2,4,5) are marginally consistent with the optical centers within the X-ray positional uncertainties (see Figure 4.1). While off-nuclear AGNs are possible (Bellovary et al., 2019; Reines et al., 2020), we also consider chance alignments between the dwarf galaxies and background X-ray sources.

[4]https://cxc.cfa.harvard.edu/csc/

Table 4.1. Sample

ID	NSAID	R.A. (deg)	Decl. (deg)	$N_{\rm H}$ (10^{20} cm^{-2})	z	r_{50} (kpc)	Distance (Mpc)	log $M_\star/M_\odot$	SFR ($M_\odot$ yr^{-1})
(1)	(2)	(3)	(4)	(5)	(6)	(7)	(8)	(9)	(10)
1	82162	140.942967	2.753302	3.58	0.0177	8.24	73	9.08	0.16
2	623354	145.180051	3.958864	3.64	0.0051	0.91	21	8.40	0.04
3	648474	141.572049	3.134800	3.82	0.0149	3.24	61	9.44	0.27
4	56620	134.438656	−0.356626	3.28	0.0277	2.69	114	9.09	0.32
5	623313	143.913363	−1.261538	3.38	0.0141	0.30	58	6.87	0.07
6	647996	133.967782	2.524284	3.89	0.0132	6.35	54	9.43	0.34

Note. — Column 1: Identification number used in this paper. Column 2: NSAIDs from v1_0_1 of the NSA. Column 3: right ascension of the galaxy. Column 4: declination of the galaxy. Column 5: galactic neutral hydrogen column density (Dickey & Lockman, 1990)[5]. Column 6: redshift, specifically the `zdist` parameter from the NSA. Column 7: Petrosion 50% light radius. Column 8: galaxy distance. Column 9: log galaxy stellar mass. Column 10: estimated SFRs from *GALEX* and *WISE* data (see Section 4). The values given in columns 6-9 are from the NSA and we assume $h = 0.73$.

Chance Alignments with Background Sources

Due to the large number of eFEDS sources ($\sim$28,000), some of the galaxies in our sample may have matched to X-ray sources purely due to spatial coincidence. Here we estimate how many matches we would expect to find due to this phenomenon. Following the same general method as in Kovács et al. (2020), we start with our estimation of how many (NSA-detected) dwarf galaxies lie in the eFEDS footprint: 495 galaxies (see Section 4). Next, we perform Monte Carlo simulations to estimate how many of these 495 dwarf galaxies may have coincidentally matched with one or more eFEDS sources. We randomly generate 495 coordinate pairs within the bounding box of the eFEDS footprint and match these random coordinates to the eFEDS X-ray sources. We use the same matching criteria as we used for our sample selection in Section 4 (i.e., the separation between the eFEDS and 'galaxy' sources be less than $2r_{50}$). As our randomly generated coordinates do not come with attached half-light radii, we instead take the r_{50} values from the actual dwarf galaxies (via the NSA) and randomly assign one to each generated coordinate. Note that of the 495 dwarf galaxies, five had bad r_{50} data; for these, we substituted the median r_{50} value of $\sim 3\farcs7$ (we also obtained near-identical results when instead using the mean r_{50} value of $\sim 4\farcs6$, or simply excluding those five galaxies/coordinates altogether). We record the number of coordinate pairs that match to at least one eFEDS X-ray source, and then repeat this process 10^5 times. The results are shown in the histogram in Figure 4.2. The distribution of random matches in our Monte Carlo simulations has a mean and median of $\sim$3.

We estimate the 95% confidence interval for the number of dwarf galaxies with X-ray sources in eFEDS following the Kraft et al. (1991) Bayesian formalism for Poisson-distributed data with low counts in the presence of a background. We have six 'counts' (the six detected matches in our sample) with a background of three counts (from chance alignment), which results in lower and upper limits of $(0, 8.90)$. From this we conclude that there are between 0-9 actual X-ray matches to dwarf galaxies in the eFEDS field. Note that these matches

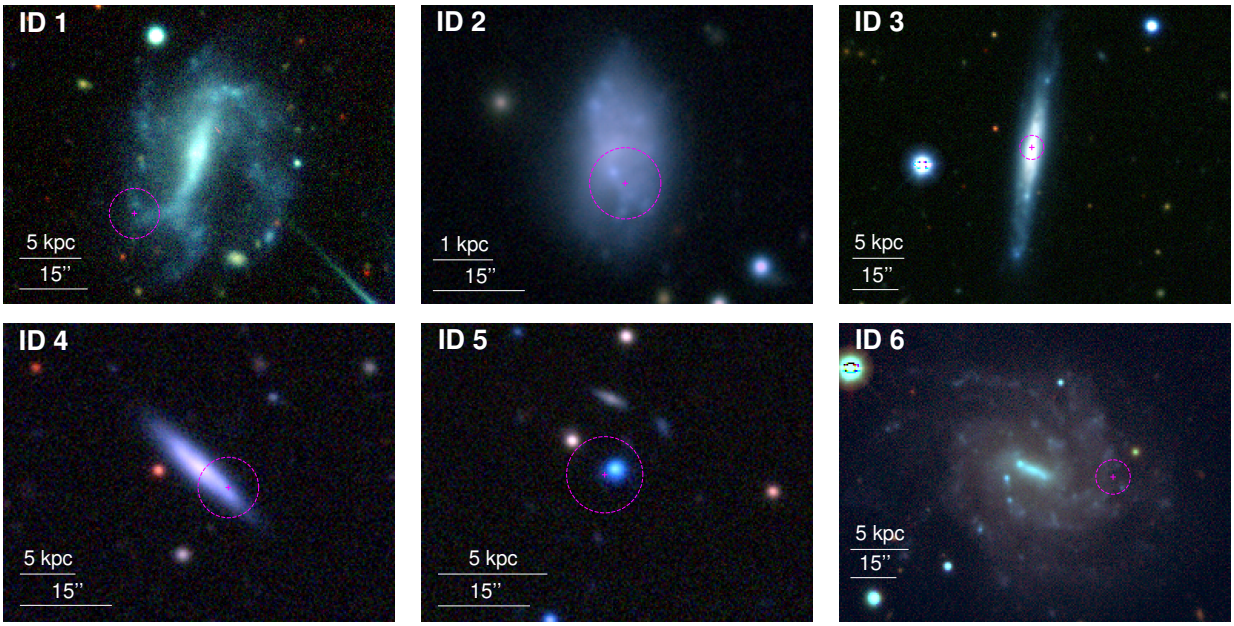


Figure 4.1 Three-color images of our galaxies retrieved from the Dark Energy Camera Legacy Survey (DECaLS; Dey et al., 2019), with red, green, and blue showing the z, r, and g bands, respectively. We overlay the positions and the corrected combined positional uncertainty (via the `RADEC_ERR_CORR` parameter from the eFEDS main catalog) in magenta.

represent dwarf galaxies with an associated X-ray source, but they are not necessarily AGNs (see Section 4 below).

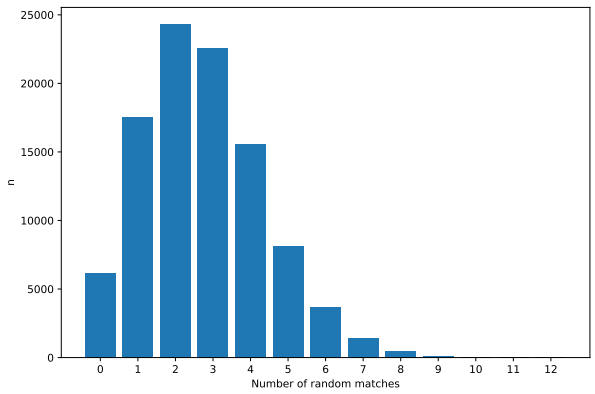


Figure 4.2 The results of matching 10^5 randomly generated coordinate sets (in the eFEDS field) to the eFEDS X-ray sources.

Origin of the X-ray Emission in Dwarf Galaxies

Here we discuss the origin of the X-ray emission under the assumption that the X-ray sources are indeed associated with the matched dwarf galaxies (although see Section 4 above). To get X-ray source properties, we re-analyze the eFEDS images[6]. We filter the images to the $0.5-2$ keV energy band to cut down on noise for our measurements. To extract counts, we use circular source regions with radii of $20''$ and accompanying background annuli regions with inner and outer radii of $30''$ and $80''$, respectively (except for ID $1-$ it had other sources nearby, so we used a background region with $30''$ and $55''$ inner and outer radii). We convert our measured net counts to $0.5-2$ keV fluxes using the $0.5-2$ keV band Energy Conversion Factor (ECF) from Brunner et al. (2021) of 1.185×10^{12} cm^2 erg^{-1}, which was found assuming an absorbed power-law with a slope of 2.0 and a Galactic absorption of 3×10^{20} cm^{-2}.

[6]retrieved from `https://erosita.mpe.mpg.de/edr/eROSITAObservations/`

To get flux values in the $0.5-8$ keV band, we apply a correction factor of $\sim$0.32 dex (a factor of $\sim$2.07), calculated via the *Chandra*-based Portable, Interactive Multi-Mission Simulator (PIMMS)[7], assuming a photon index of $\Gamma = 2$ and an absorption of $N_{\rm H} = 3 \times 10^{20}$ cm^{-2}. Note also that our sources have differing spectra (some harder than the others) so while we are consistent in our methodology, the accuracy of this one-size-fits-all extrapolation approach may vary from source to source. Our resulting $0.5-8$ keV log luminosities range between log $L_{0.5-8\ \rm keV} \sim$ 39.1-40.0 erg s^{-1} (Table 4.2). These values are similar to those of other AGNs in dwarf galaxies (e.g., Baldassare et al., 2017; Mezcua et al., 2018; Reines et al., 2014).

We next compare our observed X-ray source luminosities to the expected galaxy-wide contribution from X-ray binaries (XRBs). While enhanced X-ray emission could indicate the presence of an AGN, it is not a required condition for one. The expected X-ray luminosity from low-mass XRBs scales with stellar mass (Gilfanov, 2004), and with star-formation rate (SFR) for high-mass XRBs (Grimm et al., 2003; Mineo et al., 2012). We use the relation of Lehmer et al. (2010), which accounts for both: $L^{\rm XRB}_{2-10\ \rm keV}({\rm erg\ s^{-1}}) = \alpha M_* + \beta {\rm SFR}$ with $\alpha = (9.05 \pm 0.37) \times 10^{28}$ erg s^{-1} $M_\odot{}^{-1}$ and $\beta = (1.62 \pm 0.22) \times 10^{39}$ erg s^{-1} $(M_\odot\ {\rm yr}^{-1})^{-1}$. The relation has a scatter of 0.34 dex. The Lehmer et al. (2010) relation uses $2-10$ keV X-ray luminosities; we convert our $0.5-8$ keV luminosities to this band using a correction factor of -0.22 dex (a factor of $\sim$1.7), found using PIMMS in the same manner as before.

We estimate SFRs of the galaxies using mid-infrared (IR; 25 μm) and far-UV (FUV; 1528 Å) luminosities via the relations

$$\begin{aligned} \log {\rm SFR}(M_\odot\ {\rm yr}^{-1}) &= \log L({\rm FUV})_{\rm corr} - 43.35 \\ L({\rm FUV})_{\rm corr} &= L({\rm FUV})_{\rm obs} + 3.89 L(25\ \mu{\rm m}) \end{aligned} \tag{4.1}$$

[7] `https://cxc.harvard.edu/toolkit/pimms.jsp`

Table 4.2. X-ray sources

ID	R.A. (deg)	Decl. (deg)	Sep. (kpc)	$F_{0.5-8\ \mathrm{keV}}$ (10^{-15} erg s^{-1} cm^{-2})	log $L_{0.5-8\ \mathrm{keV}}$ (erg s^{-1})
(1)	(2)	(3)	(4)	(5)	(6)
1	140.9471979	2.7490836	7.59	3.86	39.4
2	145.1794807	3.9583302	0.29	26.21	39.1
3	141.5719005	3.1352167	0.47	12.74	39.8
4	134.4373197	−0.3575533	3.23	6.97	40.0
5	143.9138111	−1.2617757	0.51	21.34	39.9
6	133.9606284	2.5236514	6.80	12.19	39.6

Note. — Column 1: galaxy ID associated with the X-ray source. Column 2: right ascension of the X-ray source. Column 3: declination of the X-ray source. Column 4: separation between galaxy center and X-ray source position. Column 5: Flux in $0.5-8$ keV band, in erg s^{-1} cm^{-2}. Column 6: Log luminosity in $0.5-8$ keV band, in erg s^{-1}.

(Hao et al., 2011; Kennicutt & Evans, 2012). The uncertainty in the resulting SFRs is ∼0.13 dex. We retrieve FUV magnitudes from *GALEX* via the NSA. We use 22 μm magnitudes from the *Wide-field Infrared Survey Explorer (WISE)* in lieu of 25 μm luminosities from the *Infrared Astronomical Satellite (IRAS)* since none of our galaxies were detected by *IRAS* and all six of our galaxies had *WISE* detections. Moreover, the ratio between 25 μm and 22 μm flux densities is expected to be of order one (Jarrett et al., 2013), making 22 μm observations a reasonable proxy. The resulting SFRs span a range of 0.04-0.34 $M_\odot$ yr^{-1}, with a median of 0.21 $M_\odot$ yr^{-1} (Table 4.1).

We plot the observed X-ray luminosities of our sources vs. the expected cumulative X-ray luminosity from XRBs in the host galaxies in Figure 4.3. All of the galaxies have moderately significant enhanced X-ray emission at the level of 0.5-1.7 dex. Given the relatively coarse angular resolution of the X-ray data (∼16″; Predehl et al., 2021), we also consider the expected galaxy-wide luminosities from diffuse X-ray emission; we use the relation from Mineo et al. (2012), which gives the expected diffuse X-ray emission as a function of host galaxy SFR. The resulting luminosities (in the $0.5-2$ keV band) are consistently lower than the expected XRB luminosities (in the $2-10$ keV band) by 0.3-0.5 dex (factors of 2-3). In sum, the observed X-ray luminosities are suggestive of AGNs in the host galaxies but higher-resolution X-ray observations (e.g., with *Chandra*) are needed to provide a more accurate description of the emission from these galaxies.

We also consider the possibility of ultra-luminous X-ray (ULX) sources in our sample of six dwarf galaxies. The observed X-ray luminosities of our detected sources are consistent with ULXs, which are defined as off-nuclear X-ray sources having $L_X > 10^{39}$ erg s^{-1} (see Kaaret et al., 2017, for a review). We estimate the expected number of ULXs in our sample of six galaxies, which scales with SFR and metallicity (Prestwich et al., 2013). We used the combined SFR of our sample (∼1.2 $M_\odot$ yr^{-1}). Half of our sample (IDs 2-4) had line fluxes in the NSA which we could use to estimate metallicity via the relation from Pettini

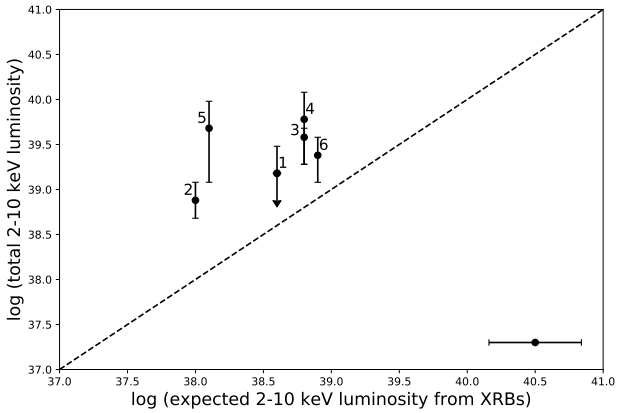


Figure 4.3 Total observed X-ray luminosities of the galaxies in our sample vs. what we would expect to see from XRBs via the relation of Lehmer et al. (2010). The dashed line represents the one-to-one relation, and the scatter of 0.34 dex in the expected XRB luminosities is shown in black in the lower right corner. The error bars shown are calculated using the 1σ error approximation from Gehrels (1986). Note also that the lower error on ID 1 was consistent with no detection; this is signified by the arrow for the lower error bar.

& Pagel (2004); these three fell into the intermediate or high metallicity bins used in Table 10 of Prestwich et al. (2013). We make the assumption that the remaining three galaxies in our sample will fall into the same metallicity bins; this results in < 1 expected ULX in our sample (using either high or intermediate metallicity). As a consistency check, we also use the results of Swartz et al. (2004) and Mapelli et al. (2010). Swartz et al. (2004) relate the expected number of ULXs in a sample to SFR and galaxy mass independently − these both result in < 1 expected ULX in our sample as well. Using the results of Mapelli et al. (2010), which are SFR-based, we find an estimated $\sim$1.5 ULXs in our sample of six galaxies. This suggests that $\sim$1 of our X-ray sources could be a ULX. If we incorporate this possibility into the confidence intervals as estimated in Section 4, this would translate to a background of four counts (instead of three), giving us 95% confidence intervals of $(0, 8.05)$.

Conclusions and Discussion

eROSITA Constraints on the AGN Fraction in Low-redshift Dwarf Galaxies

From matching dwarf galaxies in the NSA to X-ray sources in the recently released eFEDS catalog, and accounting for chance alignments with background AGNs, we find that there could be between 0-9 real associations between dwarf galaxies and X-ray sources. This puts an upper limit of $\leq 1.8\%$ on the eFEDS-selected dwarf galaxy AGN fraction. This AGN fraction is broadly consistent with findings from studies at optical ($\sim$0.5%; Reines et al., 2013) and mid-IR ($\sim$0.4%; Lupi et al., 2020) wavelengths.

There are a number of caveats to consider when interpreting these results. First, we are only exploring relatively nearby ($z \leq 0.15$) and bright dwarf galaxies that are contained in the NSA. There are also limits on the luminosities of AGNs that can be detected with a flux-limited X-ray survey as discussed below. Heavily obscured AGNs could also remain undetected.

Detection limits

Here we explore detection limits for finding AGNs in dwarf galaxies with eROSITA/eFEDS. We first estimate the minimum detectable $0.5-8$ keV luminosity of an X-ray source in our parent sample of dwarf galaxies. We start with the minimum detectable flux of $\sim 7 \times 10^{-15}$ erg cm^{-2} s^{-1} in the $0.5-2$ keV band (Brunner et al., 2021). We convert this to a $0.5-8$ keV flux using PIMMS, in the same manner as in Section 4. We use the median distance of the dwarf galaxies in the NSA ($\sim$138 Mpc) to convert to a luminosity, resulting in an estimated minimum luminosity of $L_{0.5-8\ \mathrm{keV}} \sim 10^{40.5}$ erg s^{-1}. Note however that the six galaxies in our sample all have distances lower than the median distance of dwarfs in the NSA. If we instead calculate the minimum detectable luminosity using the smallest distance in our sample ($\sim$21 Mpc; Table 4.1), we find $L_{0.5-8\ \mathrm{keV}} \sim 10^{38.9}$ erg s^{-1}, which is consistent

with our results given in Table 4.2.

The Eddington ratio of an active BH is given by

$$f_{\rm Edd} = (\kappa L_{\rm X})/(L_{\rm Edd}) \tag{4.2}$$

where κ is the $2-10$ keV bolometric correction, $L_{\rm X}$ is the X-ray luminosity of the BH, and $L_{\rm Edd}$ is the Eddington luminosity of the BH, which is found via

$$L_{\rm Edd} \approx 1.26 \times 10^{38}\ M_{\rm BH}/M_{\odot}\ {\rm erg\ s^{-1}}. \tag{4.3}$$

We convert the minimum detectable flux using PIMMS in the same manner as before, this time from the $0.5-2$ keV band to the $2-10$ keV band, with a resulting luminosity of $L_{2-10\ {\rm keV}} \sim 10^{40.2}$ erg s^{-1}. Assuming a typical BH mass of $\sim 10^5\ M_{\odot}$ for a dwarf galaxy (Reines et al., 2013) and $\kappa = 20$ (Vasudevan & Fabian, 2009), the resulting Eddington ratio is $\sim$0.04. If we instead use the minimum luminosity found using the smallest distance in our sample, we find $L_{2-10\ {\rm keV}} \sim 10^{38.7}$ erg s^{-1}, and an Eddington fraction of $\sim$0.001.

Future Prospects with eROSITA

Despite the small sample presented here based on the limited eFEDS catalog, the eROSITA All-Sky Survey (eRASS) is poised to be a boon for future searches and studies of AGNs in dwarf galaxies (Vulic et al., 2021). The eFEDs catalog covers an area on the sky of only $\sim$140 deg^2 (Brunner et al., 2021), roughly 1/300th of the sky. Extrapolating the number of sources in eFEDS to the entire sky, eRASS could result in as many as $\sim$8 million X-ray sources. However, this number is likely to be an upper limit since eFEDS is about 50% deeper than is expected for eRASS (Brunner et al., 2021) and we will only have access to (the German) half of the sky. Assuming a correction factor of $\sim$1/2, this still leaves us with as many as $\sim$4 million potential new X-ray sources (over ten times larger than the Chandra

Source Catalog Version 2.0). Additionally, these sources will be an unbiased sample as the observation is all-sky with no pre-selection of targets.

Matching the eFEDS catalog to dwarf galaxies in the NSA, and accounting for chance alignments with background AGNs, yields 0-9 AGN candidates. Extrapolating these results to the completed eRASS and accounting for the correction factor of 1/2 (see above) suggests the number of future dwarf galaxy AGN candidates at low redshift could be as many as $\sim$1350, providing an ample and exciting new sample to explore.

AER acknowledges support for this work provided by NASA through EPSCoR grant number 80NSSC20M0231. ÁB and RK were supported by NASA contract NAS8-03060. This work is based on data from eROSITA, the soft X-ray instrument aboard SRG, a joint Russian-German science mission supported by the Russian Space Agency (Roskosmos), in the interests of the Russian Academy of Sciences represented by its Space Research Institute (IKI), and the Deutsches Zentrum für Luft- und Raumfahrt (DLR). The SRG spacecraft was built by Lavochkin Association (NPOL) and its subcontractors, and is operated by NPOL with support from the Max Planck Institute for Extraterrestrial Physics (MPE). The development and construction of the eROSITA X-ray instrument was led by MPE, with contributions from the Dr. Karl Remeis Observatory Bamberg & ECAP (FAU Erlangen-Nuernberg), the University of Hamburg Observatory, the Leibniz Institute for Astrophysics Potsdam (AIP), and the Institute for Astronomy and Astrophysics of the University of Tübingen, with the support of DLR and the Max Planck Society. The Argelander Institute for Astronomy of the University of Bonn and the Ludwig Maximilians Universität Munich also participated in the science preparation for eROSITA.

CONCLUSION

In summary, we have explored different methods of detecting AGN in dwarf galaxies and applied these methods to various samples. In Chapter 2 we used combined radio and X-ray observations to tease out signs of massive BHs in a sample of five dwarf galaxies, finding one possible candidate with a tentative BH mass of $\sim 10^5\ M_\odot$. This process exemplified one difficulty in searching for signatures of BHs that do not fall into the supermassive category, the problem of confounding factors. When it comes to accreting SMBHs, often their associated detected fluxes are so high as to preclude any possibility of being sourced by another celestial object. An example of this is quasars; they are so luminous in the radio band that an accreting SMBH is the only realistic possibility.

However, massive BHs fall into the smaller mass category, and their luminosities are often accordingly smaller. As seen, this, combined with lower accretion rates, can result in problems when dealing with such low-luminosity AGN. The above method falls flat in this case, as the observed luminosity is low enough that other sourcing mechanisms are a possibility (e.g. supernova remnants, or X-ray binaries), and so the presence of an accreting BH is no longer assured. A way to mitigate this involves combining observations at different wavelengths to see if we can find spatially coincident sources across the spectrum. In Chapter 2 we used radio and X-ray observations, following on the success of this method in detecting a massive BH in Henize 2-10 by Reines et al. (2011). While none of our detected radio or X-ray luminosities were high enough to definitively mark the presence of a massive BH, we found one candidate with spatially coincident sources in both bands such that they could feasibly be sourced by a single object - and if that were true, the object could well be an AGN sourced by a massive BH. However, the coincident sources lie atop a star-forming cluster, which could plausibly host multiple objects each sourcing enough luminosity to account for the observed emission in the X-ray and radio bands separately, such as an X-ray binary and a supernova

remnant. This again returns to the problem of separating relatively low-luminosity AGN powered by massive BHs from other celestial phenomena.

In Chapter 3 we examine the accuracy of another common AGN-detection method, that of mid-IR color-color selection. While this method works reliably for more massive galaxies, it was not clear whether this would hold true for dwarf galaxies as well. We started with a sample of eleven dwarf galaxies that had been selected as having candidate AGN via the color-color selection method, using mid-IR data from *WISE*. Using optical line diagnostics, we determine that roughly half of the dwarf galaxies in our sample show evidence for hosting AGNs (classifying five as AGN, five as star-forming, and one as composite); this method is the same as was successfully used in Reines et al. (2013) for a similar purpose. We also analyzed X-ray observations of our sample, finding that the galaxies classified as AGN and composite had much higher X-ray luminosities than the ones classified as star-forming - while such findings did not rule out the presence of obscured AGN in the star-forming galaxies, they did not add confidence to the possibility. We also used multiwavelength AGN scaling relations between X-ray luminosity and mid-IR luminosity, as well as line luminosities (Hα and [O III]) to search for evidence of AGN presence in the star-forming galaxies, finding little. As we only found evidence for AGNs in roughly half of the originally mid-IR selected sample of galaxies, we concluded that this selection method results in unreliable predictions for dwarf galaxies.

This outlines another issue in the search for massive BHs in dwarf galaxies; that some of the accepted, reliable methods for finding AGN in more massive galaxies do not work very well for dwarf galaxies. In Chapter 3 we saw this apply to the mid-IR color-color method, but also to the multiwavelength AGN scaling relations. While the relatively low luminosity of many AGN powered by massive BHs presents its own confounding factors as in Chapter 2, the similarly small dwarf galaxies they reside in also contribute to the issues surrounding the identification of these massive BHs.

Chapter 4 looks to the future, using the newly-released eFEDS catalog of X-ray observations from the eROSITA telescope to search for signatures of accreting massive BHs in dwarf galaxies. Of the $\sim$28,000 X-ray sources, and the $\sim$500 dwarf galaxies in the eFEDS footprint, we found six potential AGN candidates, and noted that there could be as many as nine in total at the 95% confidence level. The eFEDS catalog uses observations from the performance verification phase of eROSITA, and covers $\sim$1/300th of the sky; we extrapolated our results to the future eROSITA all-survey and concluded that it could result in over a thousand new AGN candidates in dwarf galaxies. Given the small sample sizes that AGN candidate dwarf galaxies usually come in, as seen in Chapters 2 and 3, a potential sample this big would be very useful to explore and use.

As mentioned in the Introduction (Chapter 1), this field is still relatively new, and as has been seen, the process of identifying candidate AGNs in dwarf galaxies is not always as simple as for their more massive counterparts. One has to take into account not only the relative size of the BHs powering these AGN, but also the dwarf galaxies they live in, and how they differ from more massive galaxies as well. As the field progresses, additional possibilities will open up, such as the eROSITA all-sky survey that was mentioned above, facilitating the use of X-ray analysis to determine potential AGN candidates on a massive scale. The advent of *JWST* will also pave the way for more in-depth IR studies; some of the problems with the mid-IR color-color selection from Chapter 3 could be addressed with the much greater increase in resolution over *WISE* observations, and could bring the direct observation of smaller AGN in early-universe galaxies into the realm of possibility. Additionally, *LISA* is scheduled to launch in the 2030s, and will be able to use gravitational waves to probe BH mergers out to high redshift, which would provide another avenue of observation. Regarding more local galaxies, the upcoming class of thirty meter telescopes could provide high enough resolutions to assist in dynamical detections of BHs in dwarf galaxies, which would lead to better constraints on the occupation fraction. Building on the

foundation of the body of work dedicated to analyzing dwarf galaxies and associated AGN, the steady technological advances and the growing number of dwarf galaxy AGN candidates will further promote new discoveries in the field.

REFERENCES CITED

Aihara, H., Armstrong, R., Bickerton, S., et al. 2018, PASJ, 70, S8, doi: 10.1093/pasj/psx081

Anglés-Alcázar, D., Faucher-Giguère, C.-A., Quataert, E., et al. 2017, MNRAS, 472, L109, doi: 10.1093/mnrasl/slx161

Antonini, F., Gieles, M., & Gualandris, A. 2019, MNRAS, 486, 5008, doi: 10.1093/mnras/stz1149

Aversa, A. G., Johnson, K. E., Brogan, C. L., Goss, W. M., & Pisano, D. J. 2011, The Astronomical Journal, 141, 125. http://stacks.iop.org/1538-3881/141/i=4/a=125

Bañados, E., Venemans, B. P., Mazzucchelli, C., et al. 2018, Nature, 553, 473, doi: 10.1038/nature25180

Bachetti, M., Harrison, F. A., Walton, D. J., et al. 2014, Nature, 514, 202, doi: 10.1038/nature13791

Baldassare, V. F., Geha, M., & Greene, J. 2018, ApJ, 868, 152, doi: 10.3847/1538-4357/aae6cf

Baldassare, V. F., Geha, M., & Greene, J. 2020, The Astrophysical Journal, 896, 10, doi: 10.3847/1538-4357/ab8936

Baldassare, V. F., Reines, A. E., Gallo, E., & Greene, J. E. 2015, The Astrophysical Journal Letters, 809, L14. http://stacks.iop.org/2041-8205/809/i=1/a=L14

—. 2017, The Astrophysical Journal, 836, 20, doi: 10.3847/1538-4357/836/1/20

Baldassare, V. F., Reines, A. E., Gallo, E., et al. 2016, The Astrophysical Journal, 829, 57. http://stacks.iop.org/0004-637X/829/i=1/a=57

Becker, R. H., White, R. L., & Helfand, D. J. 1995, ApJ, 450, 559, doi: 10.1086/176166

Bellovary, J. M., Cleary, C. E., Munshi, F., et al. 2019, MNRAS, 482, 2913, doi: 10.1093/mnras/sty2842

Birchall, K. L., Watson, M. G., & Aird, J. 2020, Monthly Notices of the Royal Astronomical Society, 492, 2268, doi: 10.1093/mnras/staa040

Blanton, M. R., & Roweis, S. 2007, AJ, 133, 734, doi: 10.1086/510127

Boller, T., Freyberg, M. J., Trümper, J., et al. 2016, A&A, 588, A103, doi: 10.1051/0004-6361/201525648

Brightman, M., Harrison, F. A., Fürst, F., et al. 2018, Nature Astronomy, 2, 312, doi: 10.1038/s41550-018-0391-6

Brorby, M., Kaaret, P., & Prestwich, A. 2014, Monthly Notices of the Royal Astronomical Society, 441, 2346, doi: 10.1093/mnras/stu736

Brunner, H., Liu, T., Lamer, G., et al. 2021, arXiv e-prints, arXiv:2106.14517. https://arxiv.org/abs/2106.14517

Cann, J. M., Satyapal, S., Abel, N. P., et al. 2018, ApJ, 861, 142, doi: 10.3847/1538-4357/aac64a

Cann, J. M., Satyapal, S., Bohn, T., et al. 2020, The Astrophysical Journal, 895, 147, doi: 10.3847/1538-4357/ab8b64

Chen, C.-T. J., Brandt, W. N., Reines, A. E., et al. 2017, The Astrophysical Journal, 837, 48, doi: 10.3847/1538-4357/aa5d5b

Chomiuk, L., & Wilcots, E. M. 2009, The Astrophysical Journal, 703, 370. http://stacks.iop.org/0004-637X/703/i=1/a=370

Condon, J. J. 1992, Annual Review of Astronomy and Astrophysics, 30, 575, doi: 10.1146/annurev.aa.30.090192.003043

Corbel, S., Dubus, G., Tomsick, J. A., et al. 2012, Monthly Notices of the Royal Astronomical Society, 421, 2947, doi: 10.1111/j.1365-2966.2012.20517.x

Cox, A. L., Sparke, L. S., Watson, A. M., & van Moorsel, G. 2001, The Astronomical Journal, 121, 692. http://stacks.iop.org/1538-3881/121/i=2/a=692

Cseh, D., Corbel, S., Kaaret, P., et al. 2012, The Astrophysical Journal, 749, 17, doi: 10.1088/0004-637x/749/1/17

Denney, K. D., Rosa, G. D., Croxall, K., et al. 2014, The Astrophysical Journal, 796, 134, doi: 10.1088/0004-637x/796/2/134

Dey, A., Schlegel, D. J., Lang, D., et al. 2019, AJ, 157, 168, doi: 10.3847/1538-3881/ab089d

Dickey, C. M., Geha, M., Wetzel, A., & El-Badry, K. 2019, ApJ, 884, 180, doi: 10.3847/1538-4357/ab3220

Dickey, J. M., & Lockman, F. J. 1990, ARA&A, 28, 215, doi: 10.1146/annurev.aa.28.090190.001243

Dong, R., Greene, J. E., & Ho, L. C. 2012, The Astrophysical Journal, 761, 73, doi: 10.1088/0004-637x/761/1/73

Flesch, E. W. 2015, Publications of the Astronomical Society of Australia, 32, e010, doi: 10.1017/pasa.2015.10

Fruscione, A., McDowell, J. C., Allen, G. E., et al. 2006, in Society of Photo-Optical Instrumentation Engineers (SPIE) Conference Series, Vol. 6270, Society of Photo-Optical Instrumentation Engineers (SPIE) Conference Series, ed. D. R. Silva & R. E. Doxsey, 62701V, doi: 10.1117/12.671760

Gallo, E., Degenaar, N., & van den Eijnden, J. 2018, MNRAS, 478, L132, doi: 10.1093/mnrasl/sly083

Gallo, E., Treu, T., Jacob, J., et al. 2008, The Astrophysical Journal, 680, 154. http://stacks.iop.org/0004-637X/680/i=1/a=154

Gallo, E., Treu, T., Marshall, P. J., et al. 2010, ApJ, 714, 25, doi: 10.1088/0004-637X/714/1/25

Gandhi, P., Horst, H., Smette, A., et al. 2009, A&A, 502, 457, doi: 10.1051/0004-6361/200811368

Gehrels, N. 1986, ApJ, 303, 336, doi: 10.1086/164079

Georgakakis, A., Tsamis, Y. G., James, B. L., & Aloisi, A. 2011, Monthly Notices of the Royal Astronomical Society, 413, 1729, doi: 10.1111/j.1365-2966.2011.18248.x

Gil de Paz, A., Madore, B. F., & Pevunova, O. 2003, The Astrophysical Journal Supplement Series, 147, 29. http://stacks.iop.org/0067-0049/147/i=1/a=29

Gilfanov, M. 2004, Monthly Notices of the Royal Astronomical Society, 349, 146, doi: 10.1111/j.1365-2966.2004.07473.x

Gilfanov, M., Grimm, H.-J., & Sunyaev, R. 2004, Monthly Notices of the Royal Astronomical Society, 347, L57, doi: 10.1111/j.1365-2966.2004.07450.x

Greene, J. E. 2012, Nature Communications, 3, 1304 EP . http://dx.doi.org/10.1038/ncomms2314

Greene, J. E., & Ho, L. C. 2007, The Astrophysical Journal, 670, 92. http://stacks.iop.org/0004-637X/670/i=1/a=92

Greene, J. E., Strader, J., & Ho, L. C. 2020, Annual Review of Astronomy and Astrophysics, 58, 257, doi: 10.1146/annurev-astro-032620-021835

Griffith, R. L., Tsai, C.-W., Stern, D., et al. 2011, The Astrophysical Journal, 736, L22, doi: 10.1088/2041-8205/736/1/l22

Grimm, H.-J., Gilfanov, M., & Sunyaev, R. 2003, Monthly Notices of the Royal Astronomical Society, 339, 793, doi: 10.1046/j.1365-8711.2003.06224.x

Grimm, H.-J., Gilfanov, M., & Sunyaev, R. 2002, A&A, 391, 923, doi: 10.1051/0004-6361:20020826

Habouzit, M., Volonteri, M., & Dubois, Y. 2017, MNRAS, 468, 3935, doi: 10.1093/mnras/stx666

Hainline, K. N., Reines, A. E., Greene, J. E., & Stern, D. 2016, The Astrophysical Journal, 832, 119. http://stacks.iop.org/0004-637X/832/i=2/a=119

Hao, C.-N., Kennicutt, R. C., Johnson, B. D., et al. 2011, The Astrophysical Journal, 741, 124. http://stacks.iop.org/0004-637X/741/i=2/a=124

Hebbar, P. R., Heinke, C. O., Sivakoff, G. R., & Shaw, A. W. 2019, Monthly Notices of the Royal Astronomical Society, 485, 5604, doi: 10.1093/mnras/stz553

Hickox, R. C., & Alexander, D. M. 2018, Annual Review of Astronomy and Astrophysics, 56, 625, doi: 10.1146/annurev-astro-081817-051803

Hickox, R. C., Jones, C., Forman, W. R., et al. 2009, The Astrophysical Journal, 696, 891. http://stacks.iop.org/0004-637X/696/i=1/a=891

Hirashita, H., & Hunt, L. K. 2004, A&A, 421, 555, doi: 10.1051/0004-6361:20035835

Ho, L. C. 2008, ARA&A, 46, 475, doi: 10.1146/annurev.astro.45.051806.110546

—. 2009, ApJ, 699, 626, doi: 10.1088/0004-637X/699/1/626

Ho, L. C., Filippenko, A. V., & Sargent, W. L. 1995, ApJS, 98, 477, doi: 10.1086/192170

Hong, J., van den Berg, M., Schlegel, E. M., et al. 2005, ApJ, 635, 907, doi: 10.1086/496966

Humphrey, P. J., & Buote, D. A. 2008, The Astrophysical Journal, 689, 983. http://stacks.iop.org/0004-637X/689/i=2/a=983

Inayoshi, K., Visbal, E., & Haiman, Z. 2020, ARA&A, 58, 27, doi: 10.1146/annurev-astro-120419-014455

Izotov, Y. I., Guseva, N. G., Fricke, K. J., & Henkel, C. 2011, A&A, 536, L7, doi: 10.1051/0004-6361/201118402

Izotov, Y. I., Guseva, N. G., Fricke, K. J., Krügel, E., & Henkel, C. 2014, A&A, 570, A97, doi: 10.1051/0004-6361/201423539

Jarrett, T. H., Cohen, M., Masci, F., et al. 2011, The Astrophysical Journal, 735, 112, doi: 10.1088/0004-637x/735/2/112

Jarrett, T. H., Masci, F., Tsai, C. W., et al. 2013, The Astronomical Journal, 145, 6. http://stacks.iop.org/1538-3881/145/i=1/a=6

Johnson, K. E., Indebetouw, R., Watson, C., & Kobulnicky, H. A. 2004, The Astronomical Journal, 128, 610. http://stacks.iop.org/1538-3881/128/i=2/a=610

Kaaret, P., Feng, H., & Roberts, T. P. 2017, ARA&A, 55, 303, doi: 10.1146/annurev-astro-091916-055259

Kaviraj, S., Martin, G., & Silk, J. 2019, Monthly Notices of the Royal Astronomical Society: Letters, 489, L12, doi: 10.1093/mnrasl/slz102

Kennicutt, Robert C., J., Armus, L., Bendo, G., et al. 2003, PASP, 115, 928, doi: 10.1086/376941

Kennicutt, Robert C., J., Hao, C.-N., Calzetti, D., et al. 2009, ApJ, 703, 1672, doi: 10.1088/0004-637X/703/2/1672

Kennicutt, R. C., & Evans, N. J. 2012, Annual Review of Astronomy and Astrophysics, 50, 531, doi: 10.1146/annurev-astro-081811-125610

Kennicutt, Jr., R. C. 1998, ARA&A, 36, 189, doi: 10.1146/annurev.astro.36.1.189

Kepley, A. A., Reines, A. E., Johnson, K. E., & Walker, L. M. 2014, The Astronomical Journal, 147, 43. http://stacks.iop.org/1538-3881/147/i=2/a=43

Kewley, L. J., Groves, B., Kauffmann, G., & Heckman, T. 2006, Monthly Notices of the Royal Astronomical Society, 372, 961, doi: 10.1111/j.1365-2966.2006.10859.x

Kimbrell, S. J., Reines, A. E., Schutte, Z., Greene, J. E., & Geha, M. 2021, ApJ, 911, 134, doi: 10.3847/1538-4357/abec40

Kimbro, E., Reines, A. E., Molina, M., Deller, A. T., & Stern, D. 2021, ApJ, 912, 89, doi: 10.3847/1538-4357/abec6a

Kormendy, J., & Ho, L. C. 2013, Annual Review of Astronomy and Astrophysics, 51, 511, doi: 10.1146/annurev-astro-082708-101811

Kormendy, J., & Richstone, D. 1995, Annual Review of Astronomy and Astrophysics, 33, 581, doi: 10.1146/annurev.aa.33.090195.003053

Kovács, O. E., Bogdán, Á., & Canning, R. E. A. 2020, ApJ, 898, 164, doi: 10.3847/1538-4357/aba04f

Kraft, R. P., Burrows, D. N., & Nousek, J. A. 1991, ApJ, 374, 344, doi: 10.1086/170124

LaMassa, S. M., Cales, S., Moran, E. C., et al. 2015, The Astrophysical Journal, 800, 144, doi: 10.1088/0004-637x/800/2/144

Lang, C. C., Kaaret, P., Corbel, S., & Mercer, A. 2007, The Astrophysical Journal, 666, 79, doi: 10.1086/519553

Latimer, L. J., Reines, A. E., Bogdan, A., & Kraft, R. 2021a, ApJ, 922, L40, doi: 10.3847/2041-8213/ac3af6

Latimer, L. J., Reines, A. E., Hainline, K. N., Greene, J. E., & Stern, D. 2021b, ApJ, 914, 133, doi: 10.3847/1538-4357/abfe0c

Latimer, L. J., Reines, A. E., Plotkin, R. M., Russell, T. D., & Condon, J. J. 2019, ApJ, 884, 78, doi: 10.3847/1538-4357/ab3289

Lehmer, B. D., Alexander, D. M., Bauer, F. E., et al. 2010, The Astrophysical Journal, 724, 559. http://stacks.iop.org/0004-637X/724/i=1/a=559

Lehmer, B. D., Berkeley, M., Zezas, A., et al. 2014, The Astrophysical Journal, 789, 52. http://stacks.iop.org/0004-637X/789/i=1/a=52

Lehmer, B. D., Eufrasio, R. T., Basu-Zych, A., et al. 2021, ApJ, 907, 17, doi: 10.3847/1538-4357/abcec1

Lemons, S. M., Reines, A. E., Plotkin, R. M., Gallo, E., & Greene, J. E. 2015, The Astrophysical Journal, 805, 12. http://stacks.iop.org/0004-637X/805/i=1/a=12

Lupi, A., Sbarrato, T., & Carniani, S. 2020, Monthly Notices of the Royal Astronomical Society, 492, 2528, doi: 10.1093/mnras/stz3636

MacLeod, C. L., Ross, N. P., Lawrence, A., et al. 2016, Monthly Notices of the Royal Astronomical Society, 457, 389, doi: 10.1093/mnras/stv2997

Mapelli, M., Ripamonti, E., Zampieri, L., Colpi, M., & Bressan, A. 2010, MNRAS, 408, 234, doi: 10.1111/j.1365-2966.2010.17048.x

Marleau, F. R., Clancy, D., Habas, R., & Bianconi, M. 2017, A&A, 602, A28, doi: 10.1051/0004-6361/201629832

McMullin, J. P., Waters, B., Schiebel, D., Young, W., & Golap, K. 2007, in Astronomical Society of the Pacific Conference Series, Vol. 376, Astronomical Data Analysis Software and Systems XVI, ed. R. A. Shaw, F. Hill, & D. J. Bell, 127

Merloni, A., Heinz, S., & di Matteo, T. 2003, MNRAS, 345, 1057, doi: 10.1046/j.1365-2966.2003.07017.x

Mezcua, M. 2017, International Journal of Modern Physics D, 26, 1730021, doi: 10.1142/S021827181730021X

Mezcua, M., Civano, F., Marchesi, S., et al. 2018, Monthly Notices of the Royal Astronomical Society, 478, 2576, doi: 10.1093/mnras/sty1163

Mezcua, M., & Sánchez, H. D. 2020, The Astrophysical Journal, 898, L30, doi: 10.3847/2041-8213/aba199

Mezcua, M., Suh, H., & Civano, F. 2019, Monthly Notices of the Royal Astronomical Society, 488, 685, doi: 10.1093/mnras/stz1760

Miller, B., Gallo, E., Treu, T., & Woo, J.-H. 2012, ApJ, 747, 57, doi: 10.1088/0004-637X/747/1/57

Miller, B. P., Gallo, E., Greene, J. E., et al. 2015, ApJ, 799, 98, doi: 10.1088/0004-637X/799/1/98

Miller-Jones, J. C. A., Wrobel, J. M., Sivakoff, G. R., et al. 2012, The Astrophysical Journal Letters, 755, L1. http://stacks.iop.org/2041-8205/755/i=1/a=L1

Mineo, S., Gilfanov, M., & Sunyaev, R. 2012, Monthly Notices of the Royal Astronomical Society, 419, 2095, doi: 10.1111/j.1365-2966.2011.19862.x

Mineo, S., Gilfanov, M., & Sunyaev, R. 2012, MNRAS, 426, 1870, doi: 10.1111/j.1365-2966.2012.21831.x

Molina, M., Reines, A. E., Latimer, L. J., Baldassare, V., & Salehirad, S. 2021, ApJ, 922, 155, doi: 10.3847/1538-4357/ac1ffa

Moran, E. C., Shahinyan, K., Sugarman, H. R., Vélez, D. O., & Eracleous, M. 2014, The Astronomical Journal, 148, 136. http://stacks.iop.org/1538-3881/148/i=6/a=136

Moretti, A., Campana, S., Lazzati, D., & Tagliaferri, G. 2003, ApJ, 588, 696, doi: 10.1086/374335

Motch, C., Broderick, J. W., Pakull, M. W., Corbel, S., & Soria, R. 2010, Monthly Notices of the Royal Astronomical Society, 409, 541, doi: 10.1111/j.1365-2966.2010.17360.x

Moustakas, J., & Kennicutt, Robert C., J. 2006, ApJS, 164, 81, doi: 10.1086/500971

Murphy, E. J., Condon, J. J., Schinnerer, E., et al. 2011, The Astrophysical Journal, 737, 67. http://stacks.iop.org/0004-637X/737/i=2/a=67

Natarajan, P. 2014, General Relativity and Gravitation, 46, 1702, doi: 10.1007/s10714-014-1702-6

Nguyen, D. D., Seth, A. C., Neumayer, N., et al. 2019, ApJ, 872, 104, doi: 10.3847/1538-4357/aafe7a

O'Connor, J. A., Rosenberg, J. L., Satyapal, S., & Secrest, N. J. 2016, Monthly Notices of the Royal Astronomical Society, 463, 811, doi: 10.1093/mnras/stw1976

Pakull, M. W., & Mirioni, L. 2002, arXiv Astrophysics e-prints

Pakull, M. W., & Mirioni, L. 2003, in Revista Mexicana de Astronomia y Astrofisica Conference Series, Vol. 15, Revista Mexicana de Astronomia y Astrofisica Conference Series, ed. J. Arthur & W. J. Henney, 197–199

Panessa, F., Bassani, L., Cappi, M., et al. 2006, A&A, 455, 173, doi: 10.1051/0004-6361:20064894

Pardo, K., Goulding, A. D., Greene, J. E., et al. 2016, The Astrophysical Journal, 831, 203. http://stacks.iop.org/0004-637X/831/i=2/a=203

Park, T., Kashyap, V. L., Siemiginowska, A., et al. 2006, ApJ, 652, 610, doi: 10.1086/507406

Pettini, M., & Pagel, B. E. J. 2004, MNRAS, 348, L59, doi: 10.1111/j.1365-2966.2004.07591.x

Plotkin, R. M., & Reines, A. E. 2018, in Astronomical Society of the Pacific Conference Series, Vol. 517, Science with a Next Generation Very Large Array, ed. E. Murphy, 719

Portegies Zwart, S. F., Baumgardt, H., Hut, P., Makino, J., & McMillan, S. L. W. 2004, Nature, 428, 724, doi: 10.1038/nature02448

Predehl, P., Andritschke, R., Arefiev, V., et al. 2021, A&A, 647, A1, doi: 10.1051/0004-6361/202039313

Prestwich, A. H., Tsantaki, M., Zezas, A., et al. 2013, The Astrophysical Journal, 769, 92. http://stacks.iop.org/0004-637X/769/i=2/a=92

Ranalli, P., Georgantopoulos, I., Corral, A., et al. 2015, A&A, 577, A121, doi: 10.1051/0004-6361/201425246

Reines, A. E. 2022, Nature Astronomy, 6, 26, doi: 10.1038/s41550-021-01556-0

Reines, A. E., & Comastri, A. 2016, Publications of the Astronomical Society of Australia, 33, e054, doi: 10.1017/pasa.2016.46

Reines, A. E., Condon, J. J., Darling, J., & Greene, J. E. 2020, The Astrophysical Journal, 888, 36, doi: 10.3847/1538-4357/ab4999

Reines, A. E., & Deller, A. T. 2012, The Astrophysical Journal Letters, 750, L24. http://stacks.iop.org/2041-8205/750/i=1/a=L24

Reines, A. E., Greene, J. E., & Geha, M. 2013, The Astrophysical Journal, 775, 116. http://stacks.iop.org/0004-637X/775/i=2/a=116

Reines, A. E., Johnson, K. E., & Goss, W. M. 2008, The Astronomical Journal, 135, 2222. http://stacks.iop.org/1538-3881/135/i=6/a=2222

Reines, A. E., Plotkin, R. M., Russell, T. D., et al. 2014, The Astrophysical Journal Letters, 787, L30. http://stacks.iop.org/2041-8205/787/i=2/a=L30

Reines, A. E., Reynolds, M. T., Miller, J. M., et al. 2016, The Astrophysical Journal Letters, 830, L35. http://stacks.iop.org/2041-8205/830/i=2/a=L35

Reines, A. E., Sivakoff, G. R., Johnson, K. E., & Brogan, C. L. 2011, Nature, 470, 66 EP . http://dx.doi.org/10.1038/nature09724

Reines, A. E., & Volonteri, M. 2015, The Astrophysical Journal, 813, 82. http://stacks.iop.org/0004-637X/813/i=2/a=82

Rémy-Ruyer, A., Madden, S. C., Galliano, F., et al. 2015, A&A, 582, A121, doi: 10.1051/0004-6361/201526067

Ricarte, A., & Natarajan, P. 2018, MNRAS, 481, 3278, doi: 10.1093/mnras/sty2448

Sartori, L. F., Schawinski, K., Treister, E., et al. 2015, Monthly Notices of the Royal Astronomical Society, 454, 3722, doi: 10.1093/mnras/stv2238

Satyapal, S., Abel, N. P., & Secrest, N. J. 2018, The Astrophysical Journal, 858, 38, doi: 10.3847/1538-4357/aab7f8

Satyapal, S., Kamal, L., Cann, J. M., Secrest, N. J., & Abel, N. P. 2021, ApJ, 906, 35, doi: 10.3847/1538-4357/abbfaf

Satyapal, S., Secrest, N. J., McAlpine, W., et al. 2014, The Astrophysical Journal, 784, 113, doi: 10.1088/0004-637x/784/2/113

Schramm, M., Silverman, J. D., Greene, J. E., et al. 2013, The Astrophysical Journal, 773, 150. http://stacks.iop.org/0004-637X/773/i=2/a=150

Schulze, A., & Wisotzki, L. 2010, A&A, 516, A87, doi: 10.1051/0004-6361/201014193

Schutte, Z., Reines, A. E., & Greene, J. E. 2019, The Astrophysical Journal, 887, 245, doi: 10.3847/1538-4357/ab35dd

Secrest, N. J., Satyapal, S., Gliozzi, M., et al. 2015, ApJ, 798, 38, doi: 10.1088/0004-637X/798/1/38

She, R., Ho, L. C., & Feng, H. 2017, ApJ, 842, 131, doi: 10.3847/1538-4357/aa7634

Shu, Y., Koposov, S. E., Evans, N. W., et al. 2019, MNRAS, 489, 4741, doi: 10.1093/mnras/stz2487

Silk, J. 2017, ApJ, 839, L13, doi: 10.3847/2041-8213/aa67da

Simmonds, C., Bauer, F. E., Thuan, T. X., et al. 2016, A&A, 596, A64, doi: 10.1051/0004-6361/201629310

Stern, D., Assef, R. J., Benford, D. J., et al. 2012, The Astrophysical Journal, 753, 30, doi: 10.1088/0004-637x/753/1/30

Sutton, A. D., Roberts, T. P., Walton, D. J., Gladstone, J. C., & Scott, A. E. 2012, MNRAS, 423, 1154, doi: 10.1111/j.1365-2966.2012.20944.x

Swartz, D. A., Ghosh, K. K., Tennant, A. F., & Wu, K. 2004, ApJS, 154, 519, doi: 10.1086/422842

Swartz, D. A., Soria, R., & Tennant, A. F. 2008, The Astrophysical Journal, 684, 282, doi: 10.1086/587776

Tagawa, H., Haiman, Z., & Kocsis, B. 2020, ApJ, 892, 36, doi: 10.3847/1538-4357/ab7922

Terashima, Y., & Wilson, A. S. 2003, The Astrophysical Journal, 583, 145. http://stacks.iop.org/0004-637X/583/i=1/a=145

Vacca, W. D., Garmany, C. D., & Shull, J. M. 1996, ApJ, 460, 914, doi: 10.1086/177020

van der Marel, R. P., Alves, D. R., Hardy, E., & Suntzeff, N. B. 2002, The Astronomical Journal, 124, 2639. http://stacks.iop.org/1538-3881/124/i=5/a=2639

van Wassenhove, S., Volonteri, M., Walker, M. G., & Gair, J. R. 2010, MNRAS, 408, 1139, doi: 10.1111/j.1365-2966.2010.17189.x

Vasudevan, R. V., & Fabian, A. C. 2009, Monthly Notices of the Royal Astronomical Society, 392, 1124, doi: 10.1111/j.1365-2966.2008.14108.x

Vito, F., Brandt, W. N., Yang, G., et al. 2018, MNRAS, 473, 2378, doi: 10.1093/mnras/stx2486

Volonteri, M. 2010, The Astronomy and Astrophysics Review, 18, 279, doi: 10.1007/s00159-010-0029-x

Volonteri, M., Lodato, G., & Natarajan, P. 2008, MNRAS, 383, 1079, doi: 10.1111/j.1365-2966.2007.12589.x

Volonteri, M., & Natarajan, P. 2009, MNRAS, 400, 1911, doi: 10.1111/j.1365-2966.2009.15577.x

Volonteri, M., & Reines, A. E. 2016, ApJ, 820, L6, doi: 10.3847/2041-8205/820/1/L6

Vulic, N., Hornschemeier, A. E., Haberl, F., et al. 2021, arXiv e-prints, arXiv:2106.14526. https://arxiv.org/abs/2106.14526

Walton, D. J., Fürst, F., Heida, M., et al. 2018, ApJ, 856, 128, doi: 10.3847/1538-4357/aab610

Whitney, B. A., Sewilo, M., Indebetouw, R., et al. 2008, The Astronomical Journal, 136, 18. http://stacks.iop.org/1538-3881/136/i=1/a=18

Wright, E. L., Eisenhardt, P. R. M., Mainzer, A. K., et al. 2010, AJ, 140, 1868, doi: 10.1088/0004-6256/140/6/1868

Yu, W., & Yan, Z. 2009, The Astrophysical Journal, 701, 1940, doi: 10.1088/0004-637x/701/2/1940